
IDENTIFICATION AND ANALYSIS OF SUBSEA GAS EMISSIONS AND QUANTITATIVE BATHYMETRY OF
OCEANIC CORE COMPLEXES

A Dissertation Presented to
the Faculty of the Department of Earth and Atmospheric Sciences
University of Houston

In Partial Fulfillment of the Requirements for the Degree
Doctor of Philosophy

By
Alex Barnard
August 2014

IDENTIFICATION AND ANALYSIS OF SUBSEA GAS EMISSIONS AND QUANTITATIVE BATHYMETRY OF
OCEANIC CORE COMPLEXES

Alex Barnard

APPROVED:

Dr. Jonathan E. Snow, Advisor

Associate Professor

Dr. Alan Brandon

Associate Professor

Dr. William W. Sager

Professor

Dr. John C. Stormer, Jr.

Professor Emeritus, Rice University

Dr. Bramley J. Murton

National Oceanography Centre, UK

Dr. Dan E. Wells

Dean, College of Natural Sciences & Mathematics

ACKNOWLEDGEMENTS

Special thanks goes to Dr. Jon Snow for his guidance and sincere appreciation to Drs. Hua-Wei Zhou and John Casey both for permitting me to pursue this research and for their numerous valuable contributions. I would also like to thank my committee members, Drs. Wendy Nelson, Adry Bissada, and the staff at UH, especially Jay, Jason, Zara, Daniele, and Hannah.

For the Barbados part of this study, thanks to the crew and scientists of the R/V Atlantis during AT21-02 and Cindy Van Dover. Bill Chadwick, Susan Merle, Daniel Price, and Evan Robertson from NOAA. Rob, Lindsay, Erin, Anya, and the staff at QPS. Thanks to Michael Max and an anonymous reviewer for constructive and helpful comments that greatly improved the quality of this work. The Japanese data were supplied by JAMSTEC, and Takayuki Tomiyama helped with collation of the available data.

My deepest gratitude goes to my wife for her love and patience, constant encouragement and support. My families in the UK and China: Mum, Dad, T & Chris, Mingshan, Lixia, and relatives in Montpellier, California, Miami, Brazil and Australia. Clive for his random fillips, Jay for accommodating me, Chris, George, Jon, Joe and Rudy for the cheerful times and cups of tea. Rego, Grego, Ian, Shango, Stuart, Mick, Ben Tom, Shawn, for good times. Last but not least classmates I lost along the way: Tom (Flopsy) Roberts, never forgotten...

...and a Chihuahua called Wavelet!

Hiraeth

IDENTIFICATION AND ANALYSIS OF SUBSEA GAS EMISSIONS AND QUANTITATIVE BATHYMETRY OF
OCEANIC CORE COMPLEXES

An Abstract of a Dissertation Presented to
the Faculty of the Department of Earth and Atmospheric Sciences
University of Houston

In Partial Fulfillment of the Requirements for the Degree
Doctor of Philosophy

By

Alex Barnard

August 2014

Abstract

Subsea gas and fluid emissions point to a variety of geological processes below the seafloor. Geophysical studies of the seafloor have been focused by the climate system modelling and oil and gas communities in particular toward the identification and analysis of such emissions. Multibeam sonar allows for the rapid evaluation of hydrographic anomalies as their geological context. Advanced processing methods fuse bathymetric, acoustic backscatter, and water column data into a 4D scene useful for the interpretation of subsea targets. Studies of the detailed characteristics of subsea gas emissions help in determining the magnitude of emissions, their ability to reach surface waters, and provide further understanding of the lithosphere – hydrosphere boundary. Using the Kongsberg EM122 multibeam echo soundings from cruise AT21-02 to the Barbados Accretionary Complex, several tall 500 – 1000 m vertical water column anomalies have been identified in the water column data above cratered hummocky regions with high backscatter emitted from the seafloor at a water depth of ~1500 m. The occurrence of morphologically defined craters, circled by high amplitude seafloor backscatter values and directly beneath flares imaged in the water column, is consistent with a model of dissociation within the gas hydrate stability zone causing the release of gas bubbles into the water column.

The second part of this dissertation presents the quantitative morphology of regions of seafloor that host large-scale low-angle normal detachment faults termed oceanic core complexes. High-resolution multibeam data were used to study the morphology of two

regions of oceanic core complex formation: Godzilla Megamullion and the Chaotic Terrain, both in the extinct Parece Vela Basin, but separated by ~10 million years of spreading history. These data provide a basis for mapping and analyzing the bathymetry of the oceanic core complexes at a previously unavailable spatial resolution. Data from over 40 surveys provide a high sounding density that has been used to create surfaces gridded at ~250 m. Both the Chaotic Terrain and Godzilla Megamullion datasets are used to further understand the evolution of oceanic core complexes and the Parece Vela Basin on a regional and local scale.

Dissertation Contents

Abstract	v
Dissertation Introduction	1
<i>Subsea Gas Emissions from the Barbados Accretionary Complex</i>	5
Abstract	5
1. Introduction	6
2. Study Area	10
2.1 Multibeam Echo Soundings Acquisition and Processing Methods – Atlantis AT21-02	12
3. Results	15
3.1 Water Column Data	16
3.2 Integrated Water Column, Bathymetry, and Backscatter Data	19
4. Discussion	21
4.1 Seafloor Morphology Associated with Emissions Sites	21
4.2 Bubble Characteristics	22
4.3 Rising Bubbles	23
4.4 Current Velocity Analysis	24
4.5 CTD Water Column Data	26
4.6 Source of Methane	29
4.7 Climate Implications	30
5. Conclusions	30
6. Acknowledgements	32
7. References	33
<i>Quantitative Bathymetry of Godzilla Megamullion, Parece Vela Basin, Philippine Sea</i>	43
Abstract	43
1. Introduction	44
2. Background	45
3. Location and Geology	47
4. Methods	48
5. Results	50
5.1 Morphology of the Godzilla Megamullion	50
5.2 Lithology of the Godzilla Surface from Dredge and Dive Samples	50
5.3 Distal Section	53
5.3.1 Breakaway	53
5.3.2 West Leg Ridge	55
5.3.3 South Tail Rise	57
5.3.4 East Leg Ridge	58
5.4 Medial Section	60
5.4.1 North Tail Rise	60
5.4.2 West Hipbone Rise	62
5.4.3 East Hipbone Rise	64
5.5 Proximal Section	66
5.5.1 West Arm Rise, Backbone Rise, and East Arm Rise	66
5.5.2 East and West Shoulder Ridges	67
5.5.3 Termination	69
5.5.4 Neck Peak and Head Peak	69

6. Discussion	71
6.1 Transform Angle	73
6.2 Melt Extraction	75
6.3 Oceanic Core Complex Initiation	79
6.4 Corrugations and Ridges	83
7. Conclusions	87
8. References	89
<i>Quantitative Morphology of the Chaotic Terrain Region from Multiple Bathymetric Surveys, Parece Vela Basin, Philippine Sea</i>	93
Abstract	93
1. Introduction	94
2. Geologic Setting	96
3. Background	96
4. Location and Geology	97
5. Methods	99
6. Bathymetry of the Chaotic Terrain	100
7. Discussion	104
7.1 Comparison of the Chaotic Terrain to Mid-Atlantic Oceanic Core Complexes	113
8. Conclusions	116
9. References	117
Dissertation Conclusions	121
Appendix	123
<i>Late Holocene Climate Change Recorded in Proxy Records from Bransfield Basin Sediment Core, Antarctic Peninsula</i>	123
Abstract	124
1. Introduction	125
1.1 Environmental Setting	127
2. Study Area	129
3. Methods	130
3.1 Radiocarbon Dates	132
3.2 Sedimentology	133
3.3 Geochemistry	134
4. Results	135
4.1 Geophysical Analysis and Core Integration	135
4.2 Radiocarbon Age Model	135
4.3 Super-units and Units	137
4.4 Units	139
5. Discussion	139
5.1 Correlation of Units to Late Holocene Climate Periods	146
6. Summary and Conclusions	149
7. Acknowledgements	151
8. References	152

Dissertation Introduction

Mid-ocean ridges extend 70,000 km over the Earth's surface, but compared to their size, relatively few regions have been mapped in detail. It was not until the late 1950's that the first physiographic maps based on depth soundings were produced, e.g. Heezen et al. (1959). The maps were based on relatively few observations that were focused on the crests of mid-ocean ridges. This rather limited dataset sparked the development of a generalized model of oceanic crust and thickness, termed 'Penrose stratigraphy', at the 1st Geological Society of America Conference on Ophiolites. Until the late 1980's few mechanisms other than magmatism were considered to accommodate the divergent motion of oceanic plates. Although amagmatic spreading is a concept that had been suggested by Harry Hess in 1962, it was not until after the development of modern high-resolution multibeam sonar systems through the 1980 – 1990's that oceanic core complexes were identified on the inside corners of ridge-transform intersections (Cann et al., 1997). Only then was it realized that these peridotite massifs represent a fundamentally new mode of seafloor spreading, and provide a window into the lower crust and upper mantle. Between 30 – 50 % of the Atlantic Ocean seafloor is now known to spread by amagmatic extension accommodated by very-large-offset low-angle normal faults, or oceanic core complexes. These faults, termed detachments, exhume lower crust and mantle on the seafloor and form a transient plate boundary. Combined with their unique structural style, the concomitant tectonic, magmatic, and hydrothermal processes found in these regions of the seafloor all contribute to the formation of the intrinsic properties of the oceanic crust. Although the extension on detachment faults can last for

millions of years, the hydrothermal districts associated with oceanic core complexes are more ephemeral. Because oceanic core complexes are known to exist in varying stages of their life cycles (breakaway, runaway slip, and termination), they provide a unique opportunity to understand the fluxes of fluids and gases that pass from the geosphere hydrosphere over geologic time scales.

Multibeam echo sounders are used to map and chart the seafloor. Initially these systems were simply used to gather depth information, but it is now possible to also characterize the type of seafloor and to identify features in the water column. This dissertation relies on the QPS-SAAB hydrographic and marine processing modules. The modules provide a graphical user interface that allows raw multibeam sonar data to be processed and analyzed. All of the processing modules feed information directly into the Fledermaus module where the data can be viewed and analyzed in 4D (x, y, z, plus time). Fledermaus was first commercialized at the University of New Brunswick. Subsequently, two of the principals, Colin Ware and Larry Mayer, moved to the University of New Hampshire where development continued. Since its commercialization, the software has been licensed through the following companies: IVS-3D, Quality Positioning Systems (QPS), and presently (2014) QPS-SAAB. The water column data-processing module FMmidwater is based on GeoZui4D, and was built by Moe Doucet (QPS) in conjunction with the staff at the Center for Coastal Mapping at the University of New Hampshire. Commercial off-the-shelf software such as the QPS-SAAB modules allow marine geologists the opportunity to process, analyze, and

integrate multibeam data with other geospatial information with the aim of addressing a broad spectrum of critical marine problems.

Understanding the fluxes of fluids and gases from the seafloor is important because in 2007, as part of their assessment report, the IPCC stated that present day atmospheric levels of methane are higher than at any time in at least the last ~650 Ka, but the contributions from subsea emissions (natural) are poorly documented and quantified. Anthropogenic emissions are also poorly quantified. Qualitatively, 20 – 30 percent of offshore wells leak at some point during their operation due to well integrity failures. In 2007, 25.5 % of offshore oil and gas wells were leaking (Well Integrity and Asset Digitalization, 2014), and these emissions are also largely unquantified. Due to high profile disasters, regulations and penalties are being set in place to ensure the safety of the environment and workforce that will likely require well integrity monitoring. The methodology, strategies, and tools outlined in this dissertation are a potential roadmap for a widely applicable and practical way to identify, analyze, and monitor shallow subsea emissions, and as a basis for their incorporation into a global inventory. Allowing the investigation of integrated datasets over multiple scales also has the potential to help identify, analyze, and focus studies of subsea emissions.

Initially, the identification of hydrothermal sites at mid-ocean ridges, particularly oceanic core complexes, was the focus of this study. To do this, several multibeam datasets acquired over oceanic core complexes were investigated to see if it is possible to identify hydrothermal plumes in the water column in deep water (~3000 m) using state-of-the-art hull-mounted multibeam systems. The results over oceanic core complexes

were inconclusive, so targets were identified on the Barbados Accretionary Complex, where the water depth is shallower (~1500 m) and emissions from the seafloor related to the dissociation of gas hydrates and releases of thermogenic and biogenic gases are commonplace.

The second and third chapters of this dissertation use multibeam deliverables such as bathymetric surfaces and slope maps created from data acquired during Japanese research cruises to the Parece Vela Basin, Philippine Sea, to analyze seafloor features. This region of the seafloor is host to the largest oceanic core complex identified to date, Godzilla Megamullion, and a large region of oceanic core complexes known as the Chaotic Terrain. Integration of multiple cruise datasets has allowed the creation of gridded surfaces at high resolutions. These high-resolution surfaces provide a spring board for more detailed interpretations than has previously been possible.

References

Heezen, B.C., Tharp, M., Ewing, M., 1959. The floors of the oceans: 1. The North Atlantic. Geological Society of America Special Papers 65, 1-126.

Hess, H.H., 1962. History of ocean basins, in: Engel, A. E. J., James, H.L., Leonard, B.F. (Eds.), Petrologic studies: a volume in honor of A. F. Buddington, Geological Society of America, Boulder, CO, pp. 599–620.

Cann, J., Blackman, D., Smith, D., McAllister, E., Janssen, B., Mello, S., Avgerinos, E., Pascoe, A., Escartín, J., 1997. Corrugated slip surfaces formed at ridge-transform intersections on the Mid-Atlantic Ridge. *Nature* 385, 329-332.

Well Integrity and Asset Digitalization, 2014. Decomworld.com. Retrieved March 21, 2014, from <http://www.decomworld.com/well-asset/content-infographic.php>.

Subsea Gas Emissions from the Barbados Accretionary Complex

Abstract

Multibeam sonar is commonly used to characterize subsea gas and fluid emission sites, as it allows for the rapid evaluation of hydrographic anomalies. The development of advanced processing methods that fuse bathymetric, acoustic backscatter, and water column data into a 4D (x, y, z, and time) scene fit for the interpretation of subsea targets adds value to existing datasets. Using the multibeam deliverables to study the detailed characteristics of subsea gas emissions helps in determining the magnitude of emissions and their ability to reach surface waters, and provides further understanding of the lithosphere – hydrosphere boundary. Kongsberg EM122 MB echo soundings were used from cruise AT21-02 to the Barbados Accretionary Complex, to locate a region with several 500 – 1000 m gas plumes in the water column directly above cratered hummocky regions with high backscatter emitted from the seafloor at a water depth of ~1500 m. From bottom simulating reflectors in seismic data gas hydrates are known to exist in this region. The plumes are interpreted as the products of dissociation of gas hydrates within the stability zone. The modeled gas hydrate stability zone reaches ~600 m above the seafloor, similar to the maximum depth of disappearance of the bubble plume providing evidence for hydrate armoring of the gas bubbles. Shearing of the plume indicates that the current direction of the lower water mass was from the northwest to southeast at 128°, a direction similar to the transport direction of North Atlantic Deep Water in this region. This study highlights the utility of multibeam data in providing a geologic context for hydrographic anomalies.

1. Introduction

Modern multibeam sonar systems allows for the rapid evaluation of subsea features and provides the ability to give water column features a geological context. Recently developed advanced processing and analysis techniques have the potential to help us to locate, analyze and interpret integrated hydrographic and seafloor features. Active acoustic detection of bubbles within a water column was first achieved in the 1960s (McCartney and Bary, 1965; Ohle, 1960), and later technological advances have enabled the integration of seafloor features. Vertical water column anomalies, termed “flares” are identified in echograms from sonar systems (Artemov et al., 2007; Bünz et al., 2012; Granin et al., 2012; Greinert et al., 2006; Heeschen et al., 2003; Hovland, 2007; Hovland et al., 2012; Kannberg et al., 2013; Linke et al., 2010; Merle, 2012; Naudts et al., 2009; Naudts et al., 2010; Naudts et al., 2012; Paull et al., 2011; e.g., Paull et al., 1995; Rajan et al., 2012; Römer et al., 2012; Salyuk et al., 2002; Suess et al., 2001; Tomczak et al., 2012; Veloso et al., 2012; Weber et al., 2012).

Because of the large amount of data they collect, multibeam systems are well suited as rapid near real-time detection sensors when trying to evaluate the extent and numbers of leak points present on the seafloor, as well as for distinguishing disaster-related releases of hydrocarbons and gases from other natural seafloor seeps. Repeated survey sweeps also enable a time dimension to delineate changes in the discharges, in addition to well site integrity and monitoring after any capping attempts. Water current displacement of gas flares can also be easily mapped using multibeam data (Schneider et

al., 2010) and can aid in focusing studies to the correct near surface positions above displaced or sheared flares. Water column mapping can help to establish the water layers that are being affected, hazards to the environment for both the water column and atmosphere and whether gas is being trapped in a deeper water layer. Multibeam data enable the rapid identification and analysis of potential subsea targets prior to the deployment of ultra-high resolution studies by manned submersible, remotely operated vehicle (ROV), or autonomous underwater vehicle (AUV). Thus providing the ability to quickly detect subsea gas leakages, focus conductivity-temperature-depth (CTD), water sampling, and provide flow-rate and flux estimates (Nikolovska et al., 2008; Weber et al., 2012; Weber et al., 2014).

Subsea natural gas and fluid releases, traditionally called cold seeps, may feature low or high temperature fluids and gases. Usually the rate and temporal variation in their discharge varies considerably, thus it is more appropriate to call them emission sites. Emission sites on the seafloor are a morphologically distinct part of the carrier system that delivers abiogenic, biogenic and thermogenic gases, and fluids from the lithosphere into the hydrosphere. The releases of gases and fluids can vary in size and through time. Emission site morphology is controlled by the methane releasing mechanism, depth of the gas hydrate stability zone, and the flow rates (Naudts et al., 2010; Roberts et al., 2006). Bubble release activity varies considerably (Greinert et al., 2006; Kannberg et al., 2013; Leifer and MacDonald, 2003; Naudts et al., 2010; Nikolovska et al., 2008; Sauter et al., 2006; Torres et al., 2002), with the dominant control being pressure changes in the source (Leifer et al., 2004) which have been related to the rupture of gas hydrate seals

(Daigle et al., 2011; Tryon et al., 2002; Tryon et al., 1999). Large fluxes of thermodynamically sourced hydrocarbons can reach surface waters and atmosphere (Solomon et al., 2009), but acoustic observations of smaller gas-based sites suggest the hydrocarbons cannot reach the surface (McGinnis et al., 2006; Weber et al., 2014). Release activity is also influenced in shallow (< 500 m) water by changes in pressure due to currents and tides (Boles et al., 2001; Greinert et al., 2006; Linke et al., 2010; Newman et al., 2008; Torres et al., 2002).

The details of the surface expression of emissions sites are shaped by the sources, migration pathways, temporal and spatial variability, and subsurface structures, e.g. faults, diapirs (Riedel et al., 2002; Talukder, 2012; Talukder et al., 2007). On the seafloor gas, and fluid discharge sites are characterized by a variety of morphological expressions, including pockmarks (Chand et al., 2009; King and MacLean, 1970; Pilcher and Argent, 2007), mud volcanoes (Bonini, 2012; Jerosch et al., 2007; Kopf, 2002; Milkov, 2000; Sager et al., 2003; Savini et al., 2009; Van Rensbergen et al., 2002; Zitter et al., 2005), hydrate pingoes/mounds, (Haeckel et al., 2004; Paull et al., 2007; Riedel et al., 2002; Serié et al., 2012; Simonetti et al., 2013; Van Dover et al., 2003), and authigenic carbonates (Aloisi et al., 2000; Bian et al., 2013; Bohrmann et al., 1998; Johnson et al., 2003). Furthermore, emission sites play an important role in biological and chemical processes on the seafloor (Agirrezabala et al., 2012; Cao et al., 2013; Hovland et al., 2012; Zenskaya et al., 2012).

In order to understand the impact of subsea emissions sites, it is important that the oceans are warming (Levitus et al., 2000); surface (<700 m) ocean temperatures have

increased by $0.11^{\circ}\text{C} \pm 0.02$ in the time period between 1971 – 2010 (IPCC, 2013) and both observations and models show that natural gas hydrate dissociation is occurring as a result (Reagan and Moridis, 2009; Thatcher et al., 2013; Westbrook et al., 2009). The gas hydrate stability zone forms a thermodynamic trap for migrating and *in-situ* (e.g., biogenic), hydrocarbons (Max and Johnson, 2014). Dissociation of natural gas hydrate produces gas at an expansion factor of 164 times by volume at standard temperature and pressures. However, the estimates of both global natural gas hydrate volume (Milkov, 2004) and the quantities of gas delivered to into the oceans and atmosphere (Fisher et al., 2011; Leifer et al., 2004; Phrampus and Hornbach, 2012) vary widely. This leads to uncertainty over the potential impact that natural gas hydrates have on the climate system, and whether the gases produced could be responsible for the rapid climate changes observed during Earth's history (Dawson et al., 2011; Jones et al., 2010; e.g., Max et al., 2006; McGuire and Maslin, 2012). The Intergovernmental Panel on Climate Change (IPCC, 2013) estimates that natural emissions of methane into the atmosphere from faults, fractured rocks and the seafloor is $40 - 60 \text{ Tg (CH}_4\text{) yr}^{-1}$, or 15 – 20 % of global emissions, but it remains difficult to quantify the geographic extent of the temporal variation without more detailed inventories (Denman et al., 2007; Kvenvolden and Rogers, 2005).

Acoustic estimates of subsea emissions have reached a milestone; it is now possible using a suite of geophysical tools to estimate gas released from the seafloor on regional scales (Weber et al., 2014). In future, the technology and accuracy of the estimates will continue to improve. Characterization of regions of seafloor where emissions occur,

better estimates of the gases released into the ocean and further documentation of the processes involved and quantities of gas that reach the atmosphere are needed to further understand the global impacts of regional subsea emissions. Because it is not possible to document every seafloor feature in detail, there is a need for detailed emission site inventories and ways in which to quantify emissions with integrated datasets and calibration of the existing data. Integrating all of the sonar deliverables (bathymetry, backscatter, and water column data) into one 4D (x,y,z, and time) scene provides a cost-effective broad survey model for the rapid evaluation of a location of the seafloor including water column characteristics and their geological context.

2. Study Area

The area of investigation is the Barbados Ridge, part of the Barbados Accretionary Complex on the Caribbean plate. The accretionary complex is composed of up to 20 km thickness of structurally shortened sediments, largely detached from the down-going slab. From faults mapped by Deville et al. (2003), the structural grain in the study area is dominantly north-south (Fig. 1.1). The sediments thicken to the south as a consequence of increasing sediment burden and accretionary material flux on the Atlantic down-going slab originating from the ancestral and present-day Orinoco delta and its distal deep sea fan complexes (Westbrook et al., 1984). Mud volcanoes and cold seeps are present in this region (Langseth et al., 1988; Olu et al., 1996), and extensive natural gas hydrate layers have been interpreted from seismic profiles showing the subsurface (Brown and

Westbrook, 1988; Martin et al., 1996; Deville et al., 2006; Deville et al., 2010; Marcelle-De Silva et al., 2012).

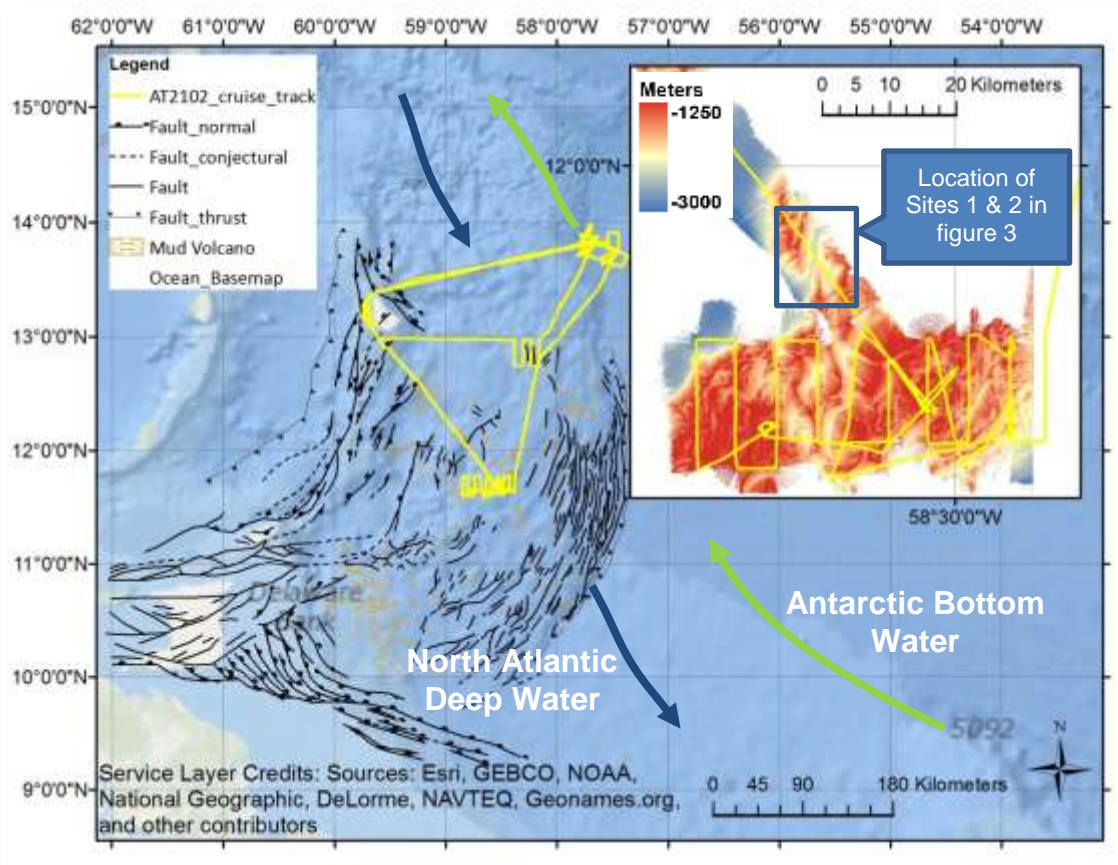


Figure 1.1. Route of the AT21-02 cruise from Barbados to several mud volcano sites within the Caribbean (yellow). Structure of the southern Barbados Accretionary Complex from Deville et al. (2003). The location and direction of deep water currents are provided for reference, and are adapted from (Pichot et al., 2012). Inset shows the study areas discussed in detail in this paper.

The Atlantic Ocean's currents play an important role in sedimentary processes and the distribution of sediments (Heezen et al., 1966; McCave and Tucholke, 1986). Turbidites and contourites controlled by these bottom currents result from thermohaline circulation that shapes sediment bodies on the continental rise (Embley and Langseth, 1977). On the Barbados Ridge two principle bottom currents exist: the North Atlantic Deep Water, which flows toward the southeast; and the Antarctic Bottom Water, which flows toward the northwest.

2.1 Multibeam Echo Soundings Acquisition and Processing

Methods – Atlantis AT21-02

The Atlantis AT21-02 cruise set out to understand the connectivity of Western-Atlantic seep communities, and as part of the multibeam data was acquired from the Barbados Ridge using a Kongsberg-Simrad EM122 system. This system has a dominant frequency of 12 kHz, with 288 beams per ping and 2 beams per ping when in multiping mode, that result in a greater sounding density and thus a higher data collection rate. Given a sound speed velocity of 1500 m/s and a dominant frequency of 12 kHz, the wavelength is ~12.5 cm. The beam dimensions are one degree by one degree, and the beam fan extends laterally approximately 75° from the vertical on both sides of the vessel. Patch test (offsets and roll pitch, yaw corrections), sound velocity profiles, and tidal information were applied to the swath sectors onboard. The multibeam data were imported into the Quality Positioning Systems (Doucet et al., 2009; Gee et al., 2012) suite of modules for further processing and analysis (Fig. 1.2).

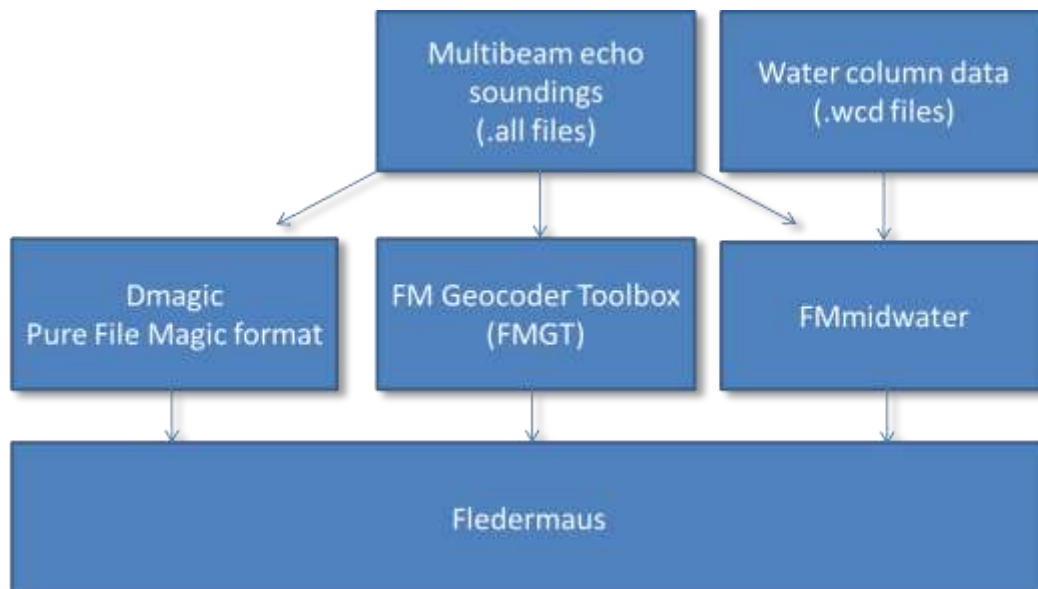


Figure 1.2. QPS multibeam processing workflow including the modules used. In this example Kongsberg format files are used (.all and .wcd) but the software accepts a wide variety of formats. The Dmagic module processes multibeam data into multi-resolution bathymetric surfaces, FM Geocoder Toolbox creates qualitative and quantitative acoustic backscatter mosaics, FMmidwater allows the visualization and analysis of water column data and the Fledermaus module integrates data from all the modules and allows visualization.

Raw multibeam data from the cruise AT21-02 is available from NOAA (<http://www.ngdc.noaa.gov/mgg/bathymetry/multibeam.html>); multibeam data were supplied in the ‘.all’ format and water column data in the ‘.wcd’ format. Both formats are native to the Kongsberg system and are supported by the Quality Positioning Systems processing modules. The modules allow the operator to process and fuse the bathymetry,

backscatter, and water column data and analyze it in 4D (Doucet et al., 2009). The time dimension effectively provides the user with visualization of the data as is was collected using the acquisition time stamps, and also allows comparison of multiple passes or surveys. The Dmagic module enables the creation of a bathymetric surface from multibeam echo soundings, whereby the data is loaded into a Pure File Magic (.pfm) structure. Data were gridded at 50 m, although multiple surfaces of varying resolutions were created over the survey area. Slope maps were created in the QPS Fledermaus module. The slope map uses a fitted plane algorithm that divides the gridded surface into blocks of 9 cells and then assigns each block with the steepest slope from the center. Acoustic backscatter was processed using the Fledermaus Geocoder Toolbox (FMGT) module, a backscatter processing toolbox that uses the integrated processing algorithms developed by Fonseca and Calder (2005).

Extraction of water column anomalies and their visualization in 4D allowed a more thorough understanding of the data (e.g., Gee et al., 2012). The processing steps require both the water column (.wcd) and navigation (.all) files in order to create a water column visualization (.gwc) file. Acoustic backscatter characteristics, such as the signal strength, spatial variability, attenuation, and frequency, with respect to beam origination, are then used to construct an interpretation of the physical properties of the feature. Temporal changes in the water column (i.e. turbulence), mixing, bubbles, temperature changes, and density differences all alter the way that sound travels through the water and the resulting sound reflectivity can be visualized.

3. Results

The presence of both flares in proximity with long-linear ridges indicates that these seafloor features are part of a deep plumbing system related to high pore fluid pressure, where the ridges are the surface expression of subsurface faulting (e.g., Talukder, 2012; Westbrook and Smith, 1983). Two water column anomalies sites occur along a short (7 – 10 km) north – south trending ridges and valleys with ~400 m of relief (Fig. 1.3). Some of the steepest slopes (~20°) on the escarpments have measured displacement/length ratios between 4 and 7, and a distinctive morphology commonly associated with faults and relays (Dawers and Anders, 1995; Walsh et al., 2002). Large escarpments have been associated with mud volcanoes by Langseth et al. (1988), who suggested that faults create migration pathways for fluids. The location of Site 1 is centered on a bathymetric depression that features hummocky bathymetry, and it is interpreted as a pockmark or ebullition crater. Where the flares erupt from the seafloor (Sites 1 & 2), the eruption site is rimmed by high backscatter values and rough slopes. Both flare sites occur along a ridge-line that is adjacent to a trough, and at both sites the flares are above regions of the seafloor characterized by craters that have chaotic changes in their slope.

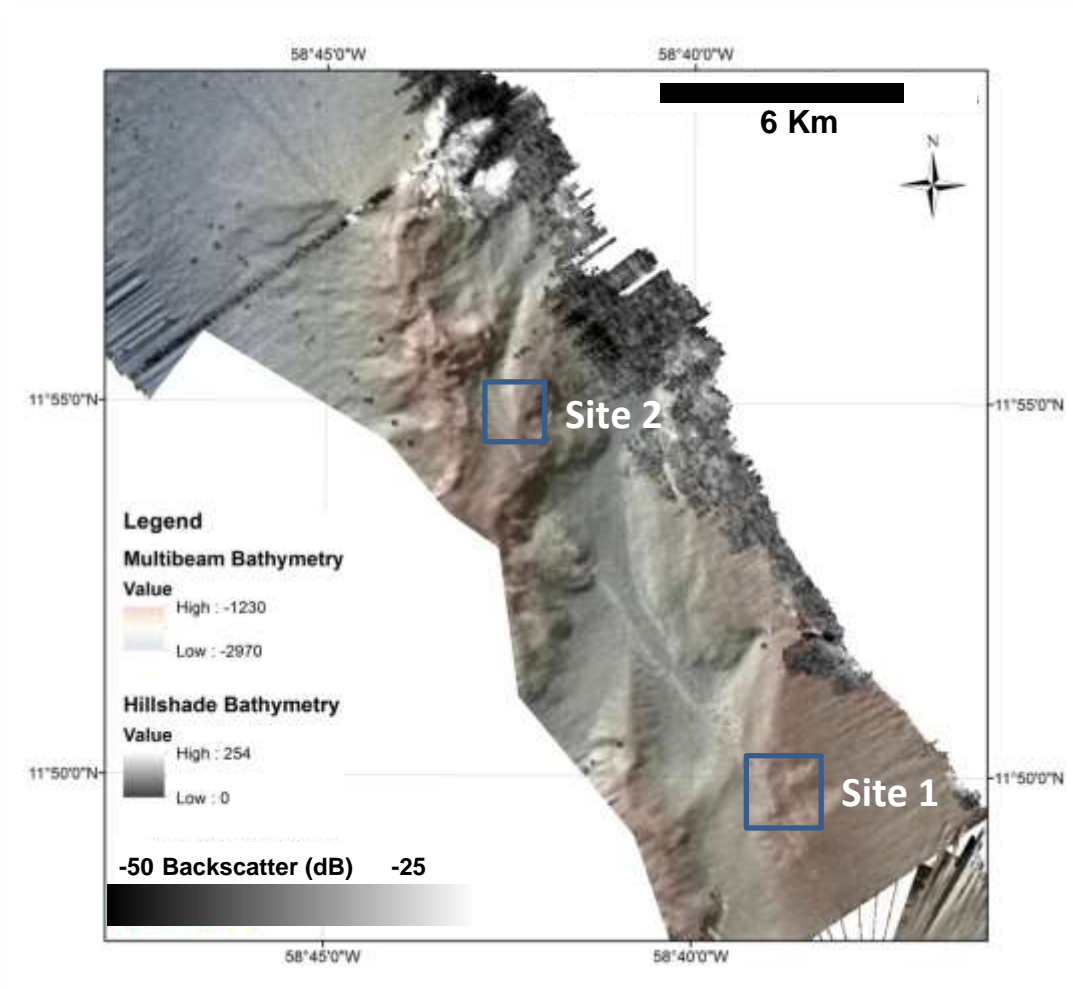


Figure 1.3. Sites identified in this study. The 3D effect in this image was achieved by using transparent hillshade bathymetry draped over backscatter imagery. A transparent multibeam bathymetry layer overlays both the integrated backscatter and hillshade to add color and scale to the relief.

3.1 Water Column Data

Vertical water column anomalies in the AT21-02 (Barbados) dataset occur in two areas clearly identified using a cross track view of the water column in figure 1.4. Some

anomalies visible in the water column are artifacts, identifiable by ‘smiles’, ‘frowns,’ and linear features in the beam fan that can be created by pulse length, side lobe pattern, refraction errors, reception and transmission beam width (Marques and Clarke, 2012). Side lobe and previous ping interference also cause false bottom echoes, which can be observed in the stacked fan view (Cobra, 1990; Tomczak et al., 2002); however, the vertical water column anomalies in the AT21-02 data are clearly resolved (Fig. 1.4).

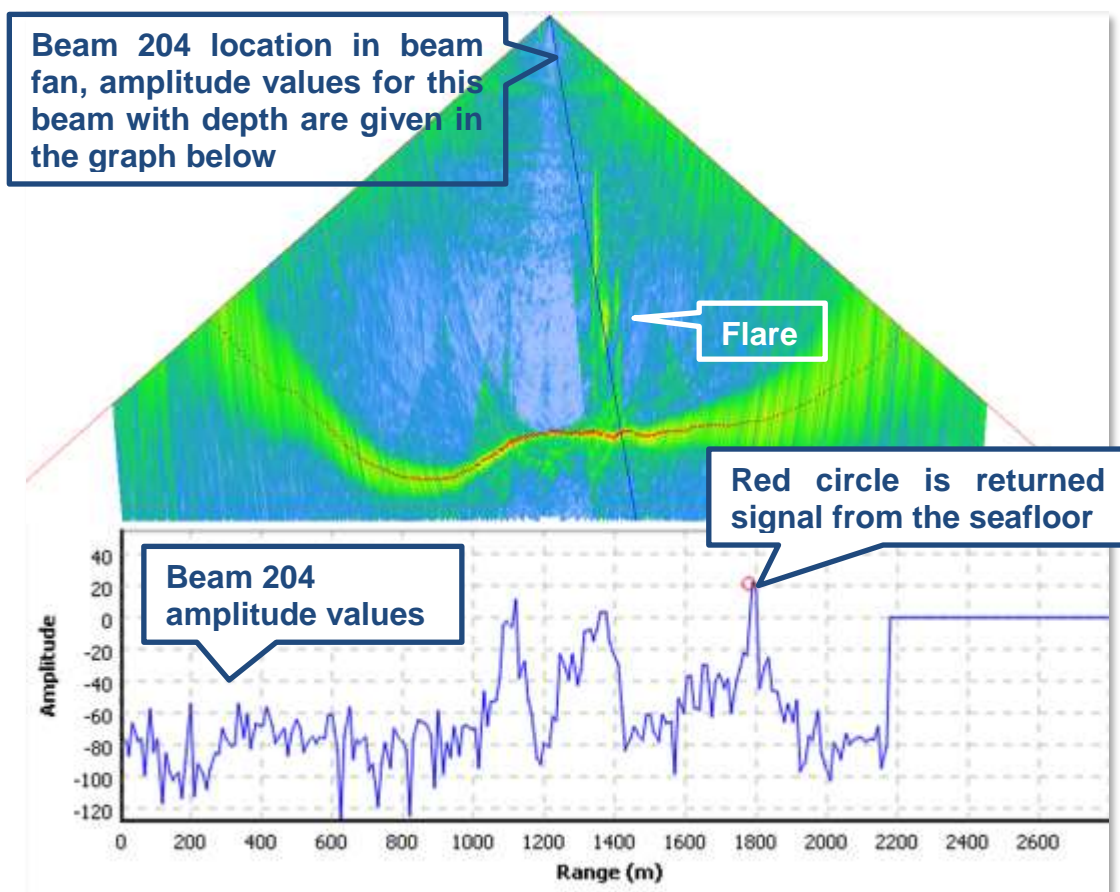


Figure 1.4. Beam fan with time series amplitude (dB) versus range (m) for beam number 204. Note that the flare is characterized by positive amplitudes, with the highest amplitude ~20dB.

Vertical water column anomalies in the AT21-02 (Barbados) dataset occur in two locations (Figs. 1.1 & 1.3, Sites 1 & 2, Table 1) at a water depth of between ~1500 and ~600 m (Figs. 1.4 & 1.5). At Site 1 two flares were identified and both are ~900 m and at site 2 the flares is ~ 800 m tall. Each has the highest amplitude backscatter occurring in the central and lower portions of the flare.

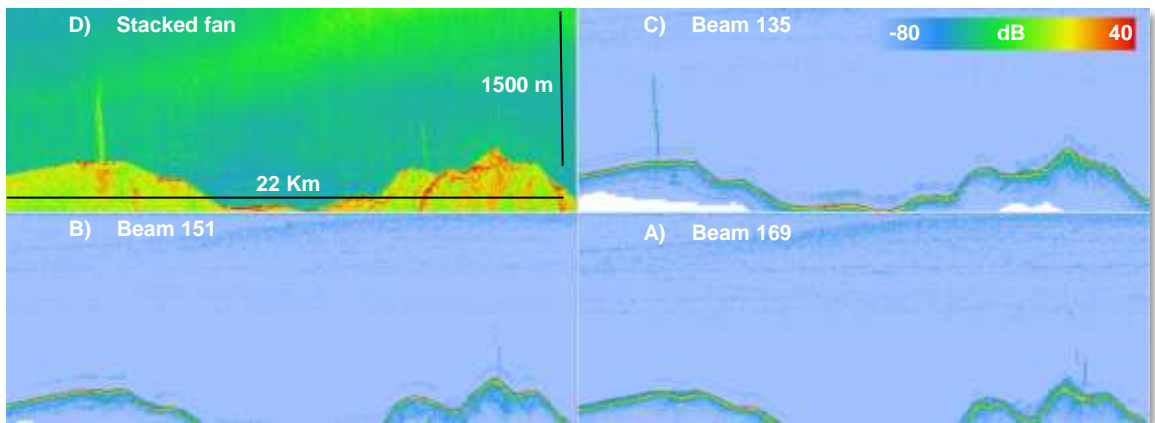


Figure 1.5. Along track water column data (view is perpendicular to the cruise track).
 A) Stacked fan, maximum filter of all the available water column data from all beams. This image highlights the regions where flares exist. B, C, and D are vertical profiles through the water column for beams 135, 151, and 169, respectively.

In a view perpendicular to the cruise track, the stacked section uses a maximum (dilation) filter to return the highest values for a neighborhood surrounding a pixel used to identify targets in the water column (e.g. wrecks, fish, and gas bubbles) (Doucet et al., 2009). This view includes some distortion because it is not corrected for the beam angle in order to incorporate all of the information for all the beams. The along track (stacked)

views presented in Figure 1.5 A – D show the location of each of the anomalies, and extraction of the anomalies from the background water column data shown in figure 1.5 identifies the curvilinear shape of the anomalies and the extent of their resolvable travel time through the water column. The amplitude values of the anomalies are provided in beam number 204, where the returned acoustic signals were ~40 – 60 dB higher than the background water column values (Figs. 1.4 & 1.5).

Site No.	Feature	Longitude	Latitude	Water Depth (m)
1	Pockmark	-58.6407	11.8274	~ 1450
2	Pockmark	-58.6985	11.9072	~ 1550

Table 1. Location of the identified seep sites (WGS84).

3.2 Integrated Water Column, Bathymetry, and Backscatter Data

The integrated multibeam deliverables provide a scene that allows recognition of hydrographic anomalies and also their relationship to the seafloor (Fig. 1.6). The small crater formed directly beneath the water column anomaly is formed by clustered, smaller semi-circular shaped features that suggest that the crater is the result of frequent ebullition activity. The occurrence of morphologically defined craters, circled by high amplitude seafloor backscatter values and directly beneath flares imaged in the water column, is consistent with a model of escaping gas from the seafloor.

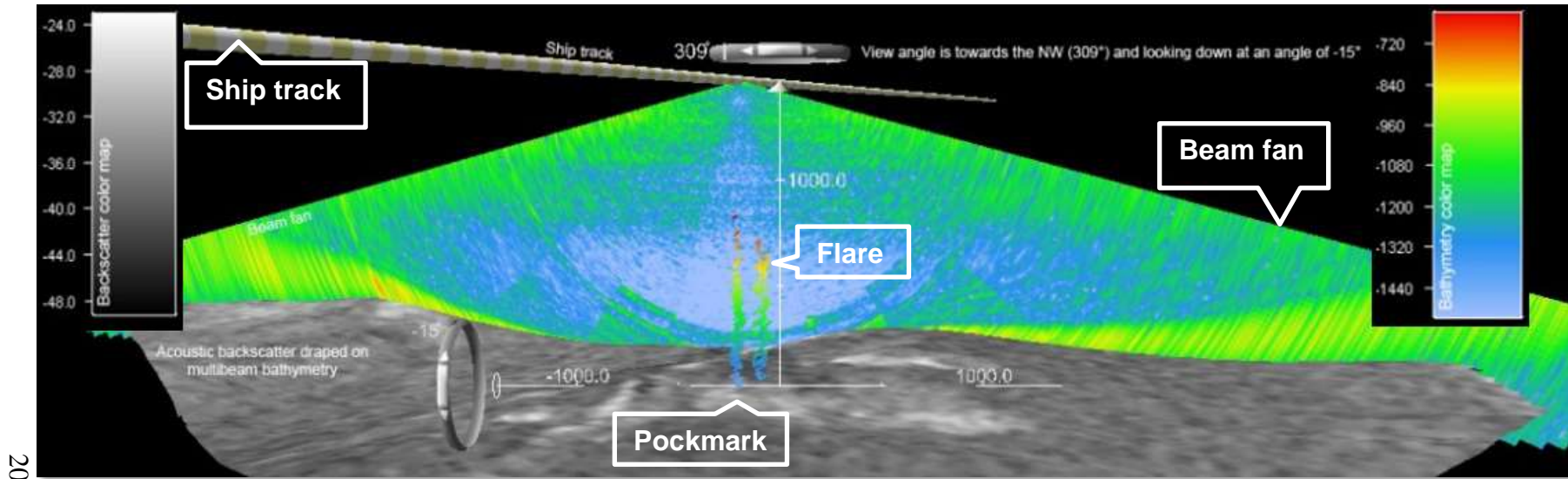


Figure 1.6. Integrated scene: backscatter draped on bathymetry, beam fan, and ship track. The scene includes the time dimension as the beam fan selected for visualization is one of many acquired along the cruise track. Acoustic backscatter and water column color maps are provided for reference. The flares are imaged to ~900 m above the seafloor elevation (~1500 m) resulting in the top of the flare being ~600 m deep. The flare is over a circular bathymetric depression characterized by high backscatter values. Other high backscatter areas are present and are interpreted as inactive emissions sites.

4. Discussion

4.1 Seafloor Morphology Associated with Emissions Sites

The emission sites identified (Sites 1 & 2, Table 1) are characterized by cratered regions of hummocky bathymetry. These circular regions of high backscatter are interpreted as mud volcanism, typically associated with gas and fluid emissions from the seafloor (e.g., Sager et al., 2003; Sager et al., 2004). Acoustic backscatter of the seafloor images changes in the volume scattering, roughness, and slope of the ensonified region. The annular high amplitude backscatter regions beneath the plume are interpreted as larger grain-size sediment (the smaller particles being carried further away) or fragments of ejected agglomerated sediment (rock from deeper or calcareous seafloor biota), gas saturated mud, or authigenic carbonate. The darker regions surrounding the Site 2 crater axis may also be the result of mud volcanism.

From the multiple concentric high backscatter crater regions, it is not clear whether there have been multiple eruptions over time or a single one with a varying eruption rate (e.g., Fig. 1.3). Because the emission sites have only local satellite craters, the deep plumbing system that feeds the gas plumes appears to be relatively stable at the present time. If emission sites could be identified across a broader region of the study area then this may indicate that multiple fluid escape pathways exist in the shallow subsurface. In contrast, the emissions appear to have either locally changed location or varied their ebullition rate or volume over small areas highlighted the regions of high backscatter beneath the plumes that may be related to hydrate plugs forming within the gas and fluid

pathways. Because of the similar sizes of each eruption site identified, the volumes of fluid and gas do not appear to have changed dramatically.

It is well understood that gas hydrates exist in this local area because seismic data from this region includes a bottom simulating reflector (Brown and Westbrook, 1988; Martin et al., 1996; Deville et al., 2006; Deville et al., 2010; Marcelle-De Silva et al., 2012). Gas hydrates can be identified in the subsurface by detection of the base of the gas hydrate stability zone that appears in seismic data as an ocean bottom simulating reflector with opposite polarity to the seafloor due to the contrast between p-wave velocities in sediments bearing gas hydrates and gases (Hyndman and Spence, 1992; Shipley et al., 1979). Gas hydrates were also recovered at a depth of 1 m in core KS20 from the Manon region, ~200 km north of the study area (Martin et al., 1996).

4.2 Bubble Characteristics

For an ideal round gas bubble, its diameter and depth are related to the received signal strength in dB, whereby deeper water and lower frequencies result in higher received signal strengths (e.g., Greinert et al., 2006, Fig. 5). It has also been shown that there is a linear, logarithmic, relationship between the volume of bubbles and the received signal strength (Ostrovsky et al., 2008) and that most of the energy returned from a bubble cloud comes from bubbles at the resonant frequency (Lee et al., 2002). Because the bubble volume is related to the target strength, the approach presented in Ostrovsky et al. (2008) to calculate bubble volume predicts a very wide range of volumes at the resonant frequency; in contrast, comparison of echogram flares and bubble plumes suggests that

the sizes are unrelated (Hovland et al., 2012). Hovland et al. (2012) suggested two possible explanations for this mismatch: 1) high concentrations of methane or hydrogen within the bubbles; or 2) the process of ebullition and bubbles in the water column creating noise (Czerski and Deane, 2010; Czerski et al., 2011; e.g., Davies et al., 2012). Although theoretical methods can be employed to understand the size and nature of the bubbles the multibeam data used in this study is not calibrated and so cannot be used to accurately quantify the volumes of gas released in the plumes identified.

4.3 Rising Bubbles

Data from artificially simulated releases of methane bubbles outside the gas hydrate stability zone demonstrates that the formation of hydrate rims inhibits mass transfer across the bubble wall (Rehder et al., 2002). McGinnis et al. (2006) provide a model for bubble dissolution that suggests a bubble with a starting diameter of ~8mm will survive for less than ten minutes above the gas hydrate stability zone before dissolving. In contrast, under the same conditions bubbles with a hydrate shell will survive for > 20 minutes (McGinnis et al., 2006, Figs. 8 & 9). Hydrate rims on bubbles are well understood (Max, 2003; Max et al., 2006, and references therein) and have been observed in both the laboratory and field (Maini and Bishnoi, 1981; Rehder et al., 2002). Hydrate rim formation typically occurs at ocean depths between 1600 and 500 m because methane hydrate is stable at low temperatures and pressures and also at high methane concentrations. The bubbles that are present in our data were released at ~1500 m. The models presented in McGinnis et al. (2006) indicate that bubbles with a hydrate rim released at this depth will dissolve at ~750 m and they are likely to be ~10 mm in

diameter. Furthermore, the models suggest that bubbles without armor would need to be ~40 mm in diameter when released in order to reach the same height, but such large bubbles are predicted to be either unlikely to exist or to break apart into smaller bubbles (McGinnis et al., 2006). Based on McGinnis et al. (2006) our estimate for the bubble size in the flares imaged in this study, using the plume flare and bubble dissolution models is ~10 mm, which results in a terminal velocity between 20 and 25 cm/s (McGinnis et al., 2006). Based on a ~10 mm bubble rising 900 m at a rate of 20 – 25 m/s, the upper and lower limits on the bubbles rise time through the entire ~1500 m water column are 60 – 75 minutes.

4.4 Current Velocity Analysis

As bubbles rise they behave as Lagrangian drifters, making them useful as ocean current indicators. Using the threshold technique of Doucet et al. (2009), it is possible to separate the anomalies from the water column data, export them as data points and fuse them into a 3D visualization that shows the shear imparted by the current velocity (Fig. 1.7). Consequently, the direction of the current can be determined by the maximum shear angle, which in this case indicates a current flow from the northwest towards the southeast at ~128°. The flares rise ~900 m and the horizontal difference between the top and the base is a maximum of ~350 m at the 128° azimuth, yielding an average ~21° of flare tilt. Using an average ascent rate of bubbles 1 - 10 mm of 20 cm/s this provides a current velocity of 8 – 10 cm/s, similar to the value of 10 cm/s measured in this region by Crease (1962).

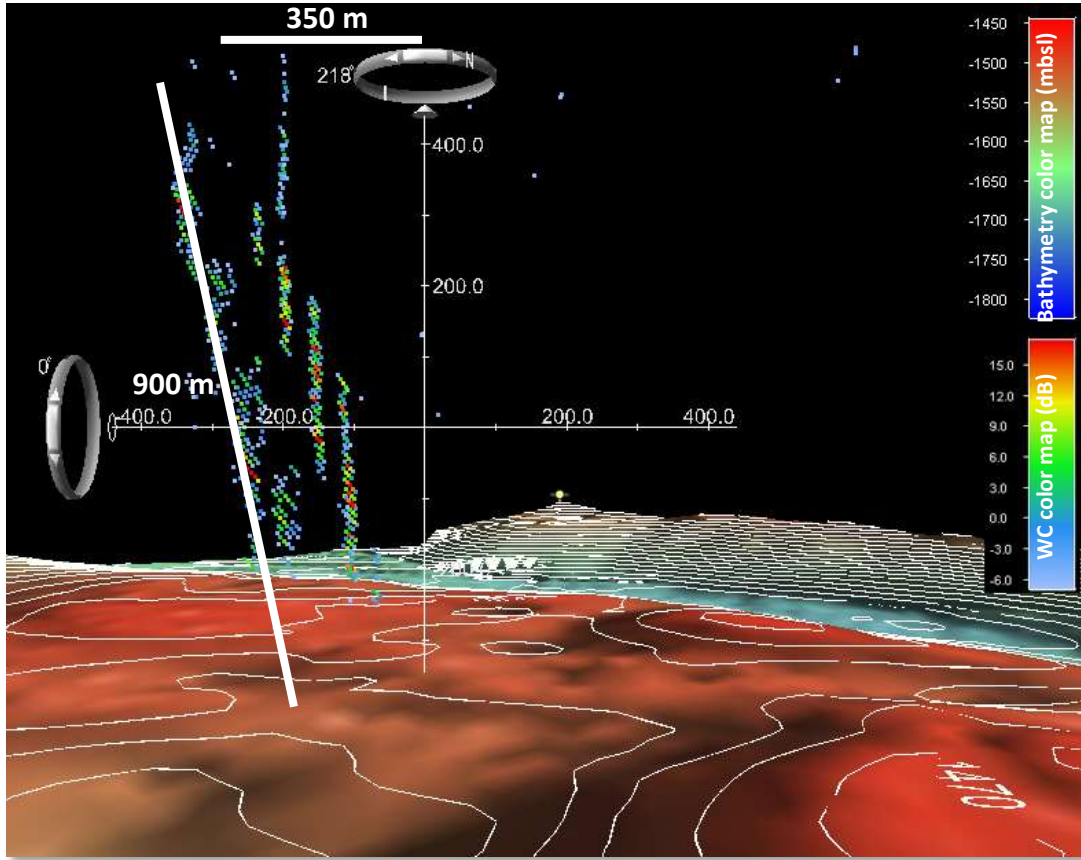


Figure 1.7. Integrated scene containing bathymetry and extracted water column data. Vertical exaggeration 1x, bathymetric contour interval is 10 m. Upper color map: bathymetry. Lower color map: amplitude in decibels for the extracted water column (WC) data. The current direction is towards 128° (from the NW), and this view is orthogonal at 218° that results in a view of the maximum shear from the water column with a shear angle of ~21° (white line). The flare is ~900 m tall, and is ~350 m offset from bottom to its top. The bathymetric contour interval is 10 m and the highest contour in the foreground is 1470 m.

The tilt of the plume reflects the current direction, but from the available data it is not possible to tell whether the current identified is a local or regional feature. Deep water currents can also be related to small-scale abyssal undular vortices (Rubino et al., 2012). Our results cannot rule out the presence of larger abyssal undular vortices that could complicate the interpretation of the current direction. The possibility exists that the observed current direction is not representative of the average mean transport, although the current direction is consistent with measured velocities (Crease, 1962) and is in agreement with the southeasterly current direction of North Atlantic Deep Water that flows over the Barbados Accretionary Complex (Pichot et al., 2012).

4.5 CTD Water Column Data

By using the models of McGinnis et al. (2006) the disappearance of the flares at a depth of ~600 m is interpreted as the depth of dissolution of hydrate armor on the rising bubbles. Bubble compositions consisting of ~87% and 100% methane, respectively, were modelled to further understand this process (Fig. 1.8). The two modeled bubble feed compositions (87 and 100% methane) were entered into the program CSMHYD (Sloan and Koh, 2008) in order to determine the depth range of the gas hydrate stability zone at different bubble gas concentrations. A composite water column (0 – 1500 m) was created using a linear interpolation of temperature measurements from CTD casts (AT21-02 survey and Reid and Mantyla, 1994). Using these inputs the gas hydrate stability zone is positioned at either 300 or 600 m for 87 and 100 % methane, respectively. This means that at depths greater than 300 m (87% methane), or 600 m (100% methane), hydrate can form where there is methane in excess of local solubility, such as around a gas bubble.

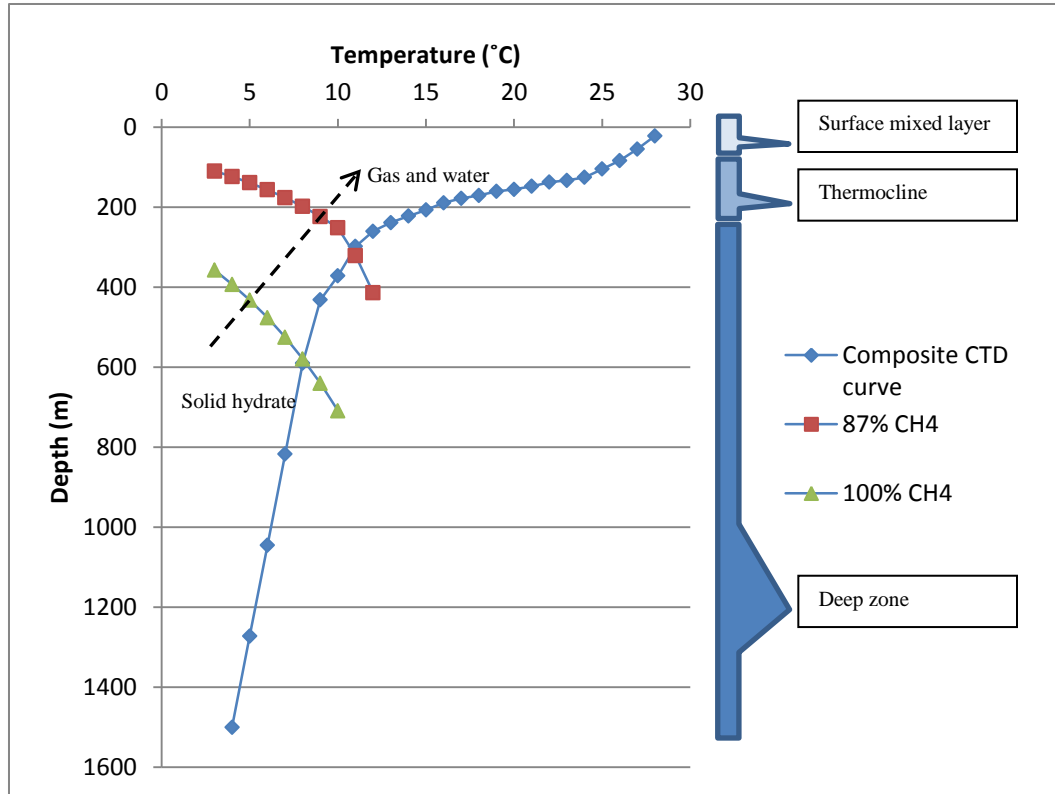


Figure 1.8. The composite CTD curve is based on a representative CTD cast from AT21-02 cruise from 0 – 400 m and an equal interval linear interpolation to seafloor data from the Reid and Mantyla (1994) dataset, courtesy of GeoMapApp (<http://www.geomapapp.org>). The 87 and 100 % methane gas hydrate stability zone models cross the CTD curve at 300 and 600 m, respectively. The bubble plume disappears at ~600 m in the acoustic data, in part due to the resolution of the data and should be taken as a maximum depth of dissolution. The acoustic results combined with model results may indicate that the bubble armor and bubbles dissolve at ~600 m, although shallower depths cannot be excluded due to the acoustic resolution of smaller bubble sizes.

The water column has been divided into three horizontal hydrographic water masses using amplitude values in the midwater data that correlated with data from CTD casts. These are: 1) the shallow surface layer above 100 m; 2) a middle layer ~100 – 250 m; and 3) a lower layer 250 – 2000 m (e.g., Kunze et al., 1987). Interestingly, from the CTD and water column data the surface mixed layer is positioned above ~100 and the thermocline penetrates to ~250 m. Integrating these results provides a theoretical basis for the disappearance of the flares at the observed ~600 m that is based on the location of the gas hydrate stability zone and indicates that the methane bubble compositions are close to ~100%. Disappearance of the bubble acoustic signature is unlikely to be caused by temperature changes in the upper water column as the depth of disappearance occurs beneath the thermocline.

Different gas compositions could also change the gas hydrate stability field, with increases in methane concentration increasing the depth of dissolution, a possible mechanism for the disappearance of plumes at sites 1 & 2 at different water depths. It should be noted that the absolute depth of bubble dissolution cannot explicitly be known solely from acoustic signal data, due to the fact that it is controlled by acoustic resolution and bubble size. Therefore, the loss of an acoustic signature at ~600 m may not necessarily be taken as the result of a particular depth of dissolution at a given composition of methane. Thus, even though indicative of a maximum depth of bubble dissolution, the acoustic resolution of the flare and the model results may not necessarily exclude bubble concentrations of less than 100% methane. However, it should be noted that these results are from flares that appear to be relatively long-lived, and changes in the

volume or rate of gas release would alter the results significantly, as shown by larger gas flares passing through the gas hydrate stability zone in Kannberg et al. (2013).

4.6 Source of Methane

The source of the methane is likely to be organic-rich mudrocks that are part of the accretionary complex, coupled with biogenic gas produced in the shallow subsurface. Methane can also be created by deep seated serpentinization processes occurring in mantle rocks along the subducted slab detachment of the subduction zone that could migrate via carrier systems into the gas hydrate stability zone (Raznitsin, 2012; Rajan et al., 2012). Gas analyses from the Barbados region indicate that the emitted gases are predominantly thermogenic gases mixed with biogenic gases (Deville et al., 2003; Pohlman et al., 2009). Thermogenic oil and gas is present in drill holes in Barbados, derived from marine Cretaceous source rocks (Hill and Schenk, 2005). The bottom simulating reflector seen in seismic lines across the Barbados Accretionary Prism (Brown and Westbrook, 1988; Deville et al., 2006; Deville et al., 2010; Marcelle-De Silva et al., 2012; Martin et al., 1996) is created by the presence of gas beneath the gas hydrate stability zone and indicates that emissions into the ocean are related to the integrity of the thermodynamic gas hydrate traps and are likely to be controlled by the pressure regime in the base gas hydrate stability zone and the presence of carrier systems such as faults. In this situation the emissions are prone to being long lived and episodic in nature, rather than catastrophic (Holbrook, 2001).

4.7 Climate Implications

External changes, such as temperature increases in ocean bottom currents are thought to influence hydrate dissociation (Revelle, 1983). This idea has been challenged because the ocean is not saturated in the molecular guest species of hydrate, so the effects of an increase in temperature of bottom layers or currents in the ocean could cause both dissolution and dissociation (e.g., Rehder et al., 2004). Conversely, changes in the temperature of sediments on the seafloor induced by the ocean above could alter the thickness of the gas hydrate stability zone by changing the depth of the bottom simulating reflector. In contrast, the gas hydrate stability zone is heterogeneous and has been shown to have internal complexity and lateral and vertical variability (Boswell and Collett, 2006; Max et al., 2006). Furthermore, the internal variability of the hydrate system and the quantity of hydrate within the gas hydrate stability zone is related to the internal plumbing system, about which little is currently known in this region.

5. Conclusions

Several vertical flares 500 – 1000 m high in the water column have been identified using water column multibeam data. Combined with observations of the acoustic backscatter and bathymetry of the seafloor, the water column anomalies are interpreted as plumes of gas bubbles rising from the seafloor. The calculated horizontal shear of the flares has been found to be consistent with a current direction and velocity similar to that of North Atlantic Deep Water in this region. The CSMHYD model of the gas hydrate stability zone and composite temperature curve for the water column show an upper limit

of the gas hydrate stability zone that lies deeper than the pycnocline, between 300 – 600 m, for bubbles for gas compositions of 87 – 100 % methane, respectively. Disappearance of the acoustic flares at ~600 m is therefore likely to be related to the dissolution of hydrate armor surrounding the bubbles in the water column. These acoustic observations suggest that when using multibeam data it is difficult to resolve whether methane released in deep water (~1500 m) reach surface waters as its acoustic signature may not persist to high levels in the water column. A better understanding of the volumes of gases in the water column can be gained using calibrated multibeam systems coupled with direct observations, however this study draws attention to what can presently be achieved and understood.

A better understanding of the deep water currents and plumbing system in this region will allow better quantification of the impact gases released from sediments overlying accretionary prisms will have on climate in the future. To do this further observations such as ROV studies of the bubble sizes, 3D seismic, a calibrated-multibeam survey, and geochemical studies of the fluid and gas released are necessary to fully characterize the subsurface plumbing system. Additionally, the installation of upward looking acoustic Doppler current profiler (ADCP) would allow for a better understanding of the deep water currents that operate in this region. Gas and fluid emissions from the seafloor are related to the structural style, the gas hydrate stability zone, and underlying petroleum systems. This study highlights the importance of integrating all of the available multibeam data to provide a geologic context for hydrographic anomalies.

6. Acknowledgements

Thanks to the crew and scientists of the R/V Atlantis during AT21-02, particularly Cindy Van Dover. Thanks to Bill Chadwick, Susan Merle, Daniel Price, and Evan Robertson from NOAA, Lindsay Gee, Anya Duxfield, Erin Heffron and the staff at QPS, and Bramley Murton (NOCS). I would also like to thank Michael Max, William Sager, Jon Snow, and an anonymous reviewer for their support and constructive comments that significantly improved this paper. This research was funded by the University of Houston, Department of Earth and Atmospheric Sciences Teaching Assistantship.

7. References

- Agirrezabala, L.M., Kiel, S., Blumenberg, M., Schäfer, N., Reitner, J., 2012. Outcrop analogues of pockmarks and associated methane-seep carbonates: a case study from the Lower Cretaceous (Albian) of the Basque-Cantabrian Basin, western Pyrenees. *Palaeogeography, Palaeoclimatology, Palaeoecology* 390, 94-115.
- Aloisi, G., Pierre, C., Rouchy, J.-M., Foucher, J.-P., Woodside, J., 2000. Methane-related authigenic carbonates of eastern Mediterranean Sea mud volcanoes and their possible relation to gas hydrate destabilisation. *Earth and Planetary Science Letters* 184, 321-338.
- Artemov, Y.G., Egorov, V., Polikarpov, G., Gulin, S., 2007. Methane emission to the hydro- and atmosphere by gas bubble streams in the Dnieper paleo-delta, the Black Sea. *National Academy of Sciences Ukraine*, 5, 110-116.
- Bian, Y., Feng, D., Roberts, H.H., Chen, D., 2013. Tracing the evolution of seep fluids from authigenic carbonates: Green Canyon, northern Gulf of Mexico. *Marine and Petroleum Geology* 44, 71-81.
- Bohrmann, G., Greinert, J., Suess, E., Torres, M., 1998. Authigenic carbonates from the Cascadia subduction zone and their relation to gas hydrate stability. *Geology* 26, 647-650.
- Boles, J., Clark, J., Leifer, I., Washburn, L., 2001. Temporal variation in natural methane seep rate due to tides, Coal Oil Point area, California. *Journal of Geophysical Research: Oceans* (1978–2012) 106, 27077-27086.
- Bonini, M., 2012. Mud volcanoes: Indicators of stress orientation and tectonic controls. *Earth-Science Reviews* 115(3), 121-152.
- Boswell, R., Collett, T.S., 2006. The gas hydrates resource pyramid, methane hydrate newsletter. U.S. Department of Energy, Office of Fossil Energy, National Energy Technology Laboratory, Fire in the Ice Newsletter, pp. 5-7.
- Brown, K., Westbrook, G.K., 1988. Mud diapirism and subcretion in the Barbados Ridge Accretionary Complex: The role of fluids in accretionary processes. *Tectonics* 7, 613-640.
- Bünz, S., Polyanov, S., Vadakkepuliambatta, S., Consolaro, C., Mienert, J., 2012. Active gas venting through hydrate-bearing sediments on the Vestnesa Ridge, offshore W-Svalbard. *Marine Geology* 332, 189-197.
- Cao, Y., Su, Z., Chen, D., 2013. Influence of water flow on gas hydrate accumulation at cold vents. *Science China Earth Sciences* 56(4), 568-578.

Chand, S., Rise, L., Ottesen, D., Dolan, M., Bellec, V., Bøe, R., 2009. Pockmark-like depressions near the Goliat hydrocarbon field, Barents Sea: Morphology and genesis. *Marine and Petroleum Geology* 26, 1035-1042.

Cobra, D.E.Q., 1990. Estimation and correction of geometric distortions in side-scan sonar images. Unpublished doctoral dissertation, Massachusetts Institute of Technology/Woods Hole Oceanographic Institution, USA.

Crease, J., 1962. Velocity measurements in the deep water of the western North Atlantic: Summary. *Journal of Geophysical Research* 67, 3173-3176.

Czerski, H., Deane, G.B., 2010. Contributions to the acoustic excitation of bubbles released from a nozzle. *The Journal of the Acoustical Society of America* 128, 2625.

Czerski, H., Twardowski, M., Zhang, X., Vagle, S., 2011. Resolving size distributions of bubbles with radii less than 30 μm with optical and acoustical methods. *Journal of Geophysical Research: Oceans* (1978–2012) 116.

Daigle, H., Bangs, N.L., Dugan, B., 2011. Transient hydraulic fracturing and gas release in methane hydrate settings: A case study from southern Hydrate Ridge. *Geochemistry, Geophysics, Geosystems* 12, Q12022.

Davies, R.J., Thatcher, K.E., Mathias, S.A., Yang, J., 2012. Deepwater canyons: An escape route for methane sealed by methane hydrate. *Earth and Planetary Science Letters* 323–324, 72-78.

Dawers, N.H., Anders, M.H., 1995. Displacement-length scaling and fault linkage. *Journal of Structural Geology* 17, 607-614.

Dawson, A., Bondevik, S., Teller, J., 2011. Relative timing of the Storegga submarine slide, methane release, and climate change during the 8.2 ka cold event. *The Holocene* 21, 1167-1171.

Denman, K.L., Brasseur, G., Chidthaisong, A., Ciais, P., Cox, P.M., Dickinson, R.E., Hauglustaine, D., Heinze, C., Holland, E., Jacob, D., 2007. Couplings between changes in the climate system and biogeochemistry. *Climate Change* 2007, 541-584.

Deville, É., Battani, A., Griboulard, R., Guerlais, S., Herbin, J., Houzay, J., Muller, C., Prinzhofer, A., 2003. The origin and processes of mud volcanism: New insights from Trinidad and the Barbados Prism. *Geological Society, London, Special Publications* 216, 475-490.

Deville, É., Guerlais, S.-H., Callec, Y., Griboulard, R., Huyghe, P., Lallemand, S., Mascle, A., Noble, M., Schmitz, J., 2006. Liquefied vs stratified sediment mobilization processes: Insight from the South of the Barbados accretionary prism. *Tectonophysics* 428, 33-47.

Deville, É., Guerlais, S.-H., Lallemand, S., Schneider, F., 2010. Fluid dynamics and subsurface sediment mobilization processes: an overview from Southeast Caribbean. *Basin Research* 22, 361-379.

Doucet, M., Ware, C., Arsenault, R., Weber, T., Malik, M.A., Mayer, L., Gee, L., 2009. Advanced mid-water tools for 4D marine data fusion and analysis, OCEANS 2009, MTS/IEEE Biloxi-Marine Technology for Our Future: Global and Local Challenges. IEEE, pp. 1-9.

Embley, R.W., Langseth, M.G., 1977. Sedimentation processes on the continental rise of northeastern South America. *Marine Geology* 25, 279-297.

Fisher, R.E., Sriskantharajah, S., Lowry, D., Lanoisellé, M., Fowler, C., James, R., Hermansen, O., Lund Myhre, C., Stohl, A., Greinert, J., 2011. Arctic methane sources: Isotopic evidence for atmospheric inputs. *Geophysical Research Letters* 38(21).

Fonseca, L., Calder, B., 2005. Geocoder: an efficient backscatter map constructor, Proceedings of the US Hydrographic Conference, San Diego.

Gee, L., Doucet, M., Parker, D., Weber, T., Beaudoin, J., 2012. Is multibeam water column data really worth the disk space, in Proceedings of Hydro12 – Taking Care of the Sea, San Diego, CA pp. 81–86.

Granin, N.G., Muyakshin, S.I., Makarov, M.M., Kucher, K.M., Il'ya, A.A., Granina, L.Z., Mizandroutsev, I.B., 2012. Estimation of methane fluxes from bottom sediments of Lake Baikal. *Geo-Marine Letters* 32, 427-436.

Greinert, J., Artemov, Y., Egorov, V., De Batist, M., McGinnis, D., 2006. 1300-m-high rising bubbles from mud volcanoes at 2080m in the Black Sea: Hydroacoustic characteristics and temporal variability. *Earth and Planetary Science Letters* 244, 1-15.

Haeckel, M., Suess, E., Wallmann, K., Rickert, D., 2004. Rising methane gas bubbles form massive hydrate layers at the seafloor. *Geochimica et Cosmochimica Acta* 68, 4335-4345.

Heeschen, K.U., Tréhu, A.M., Collier, R.W., Suess, E., Rehder, G., 2003. Distribution and height of methane bubble plumes on the Cascadia Margin characterized by acoustic imaging. *Geophysical Research Letters* 30, 1643–1646.

Heezen, B., Schneider, E., Pilkey, O., 1966. Sediment transport by the Antarctic bottom current on the Bermuda Rise. *Nature* 211, 611-612.

Hill, R.J., Schenk, C.J., 2005. Petroleum geochemistry of oil and gas from Barbados: Implications for distribution of Cretaceous source rocks and regional petroleum prospectivity. *Marine and Petroleum Geology* 22, 917-943.

Holbrook, W.S., 2001. Seismic studies of the Blake Ridge: Implications for hydrate distribution, methane expulsion, and free gas dynamics, *Natural Gas Hydrates: Occurrence, Distribution, and Detection*. AGU, Washington, DC, pp. 235-256.

Hovland, M., 2007. Discovery of prolific natural methane seeps at Gullfaks, northern North Sea. *Geo-Marine Letters* 27, 197-201.

Hovland, M., Jensen, S., Fichler, C., 2012. Methane and minor oil macro-seep systems — Their complexity and environmental significance. *Marine Geology* 332–334, 163-173.

Hyndman, R., Spence, G., 1992. A seismic study of methane hydrate marine bottom simulating reflectors. *Journal of Geophysical Research: Solid Earth* (1978–2012) 97, 6683-6698.

IPCC, 2013. Summary for Policymakers, *Climate Change 2013: The Physical Science Basis. Contribution of Working Group I to the Fifth Assessment Report of the Intergovernmental Panel on Climate Change*. Cambridge University Press, Cambridge United Kingdom and New York, NY, USA.

Jerosch, K., Schlüter, M., Foucher, J.-P., Allais, A.-G., Klages, M., Edy, C., 2007. Spatial distribution of mud flows, chemoautotrophic communities, and biogeochemical habitats at Håkon Mosby Mud Volcano. *Marine Geology* 243, 1-17.

Johnson, J.E., Goldfinger, C., Suess, E., 2003. Geophysical constraints on the surface distribution of authigenic carbonates across the Hydrate Ridge region, Cascadia margin. *Marine Geology* 202, 79-120.

Jones, T.D., Ridgwell, A., Lunt, D., Maslin, M., Schmidt, D., Valdes, P., 2010. A Palaeogene perspective on climate sensitivity and methane hydrate instability. *Philosophical Transactions of the Royal Society A: Mathematical, Physical and Engineering Sciences* 368, 2395-2415.

Kannberg, P.K., Tréhu, A.M., Pierce, S.D., Paull, C.K., Caress, D.W., 2013. Temporal variation of methane flares in the ocean above Hydrate Ridge, Oregon. *Earth and Planetary Science Letters* 368, 33-42.

King, L.H., MacLean, B., 1970. Pockmarks on the Scotian shelf. *Geological Society of America Bulletin* 81, 3141-3148.

Kopf, A.J., 2002. Significance of mud volcanism. *Reviews of Geophysics* 40, 2-1-2-52.

Kvenvolden, K.A., Rogers, B.W., 2005. Gaia's breath—global methane exhalations. *Marine and Petroleum Geology* 22, 579-590.

Kunze, E., Williams, A.J., Schmitt, R.W., 1987. Optical microstructure in the thermohaline staircase east of Barbados. *Deep Sea Research Part A. Oceanographic Research Papers* 34(10), 1697-1704.

Langseth, M.G., Westbrook, G.K., Hobart, M.A., 1988. Geophysical survey of a mud volcano seaward of the Barbados Ridge Accretionary Complex. *Journal of Geophysical Research: Solid Earth* 93, 1049-1061.

Lee, K.I., Choi, B.K., Yoon, S.W., 2002. Acoustic pressure reflection coefficients of a subsurface bubble layer in water. *Journal of the Korean Physical Society* 40, 256-263.

Leifer, I., MacDonald, I., 2003. Dynamics of the gas flux from shallow gas hydrate deposits: interaction between oily hydrate bubbles and the oceanic environment. *Earth and Planetary Science Letters* 210, 411-424.

Leifer, I., Boles, J., Luyendyk, B., Clark, J., 2004. Transient discharges from marine hydrocarbon seeps: spatial and temporal variability. *Environmental Geology* 46, 1038-1052.

Levitus, S., Antonov, J.I., Boyer, T.P., Stephens, C., 2000. Warming of the World Ocean. *Science* 287, 2225-2229.

Linke, P., Sommer, S., Rovelli, L., McGinnis, D., 2010. Physical limitations of dissolved methane fluxes: The role of bottom layer processes. *Marine Geology* 272, 209-222.

Maini, B.B., Bishnoi, P., 1981. Experimental investigation of hydrate formation behaviour of a natural gas bubble in a simulated deep sea environment. *Chemical Engineering Science* 36, 183-189.

Marcelle-De Silva, J., Thomas, A., De Landro Clarke, W.L., Allum, M., 2012. Evidence of Gas Hydrates in Block 26—Offshore Trinidad. *Energies* 5, 1309-1320.

Marques, C.R., Clarke, J.E.H., 2012. Automatic mid-water target tracking using multibeam water column, Canadian Hydrographic Conference, Niagara Falls.

Martin, J.B., Kastner, M., Henry, P., Le Pichon, X., Lallement, S., 1996. Chemical and isotopic evidence for sources of fluids in a mud volcano field seaward of the Barbados accretionary wedge. *Journal of Geophysical Research: Solid Earth* 101, 20325-20345.

Max, M.D., 2003. Natural gas hydrate in oceanic and permafrost environments. Kluwer Academic Pub.

Max, M.D., Johnson, A.H., Dillon, W.P., 2006. Economic geology of natural gas hydrate. Kluwer Academic Pub.

Max, M.D., Johnson, A.H., 2014. Hydrate petroleum system approach to natural gas hydrate exploration. *Petroleum Geoscience* 20, 187-199.

McCartney, B., Bary, B.M., 1965. Echo-sounding on probable gas bubbles from the bottom of Saanich Inlet, British Columbia, *Deep Sea Research and Oceanographic Abstracts*. Elsevier, pp. 285-294.

McCave, I.N., Tucholke, B.E., 1986. Deep current-controlled sedimentation in the western North Atlantic, in: Vogt, P.R., Tucholke, B.E. (Eds.), *The Geology of North America, Vol. M, The Western North Atlantic region, Decade of North America Geology*, Geological Society of America, Boulder, CO, pp. 451-468.

McGinnis, D.F., Greinert, J., Artemov, Y., Beaubien, S.E., Wüest, A., 2006. Fate of rising methane bubbles in stratified waters: How much methane reaches the atmosphere? *Journal of Geophysical Research: Oceans* (1978-2012), 111(C9).

McGuire, B., Maslin, M.A., 2012. Climate forcing of geological hazards. Wiley-Blackwell.

Merle, S.G., Chadwick, W.W., Embley, R.W., Doucet, M., 2012. Bubble plumes at NW Rota-1 submarine volcano, Mariana Arc: Visualization and analysis of multibeam water column data, AGU Fall Meeting, San Francisco.

Milkov, A., 2000. Worldwide distribution of submarine mud volcanoes and associated gas hydrates. *Marine Geology* 167, 29-42.

Milkov, A.V., 2004. Global estimates of hydrate-bound gas in marine sediments: how much is really out there? *Earth-Science Reviews* 66, 183-197.

Naudts, L., De Batist, M., Greinert, J., Artemov, Y., 2009. Geo-and hydro-acoustic manifestations of shallow gas and gas seeps in the Dnepr paleodelta, northwestern Black Sea. *The Leading Edge* 28, 1030-1040.

Naudts, L., Greinert, J., Poort, J., Belza, J., Vangampelaere, E., Boone, D., Linke, P., Henriët, J.-P., De Batist, M., 2010. Active venting sites on the gas-hydrate-bearing Hikurangi Margin, off New Zealand: Diffusive-versus bubble-released methane. *Marine Geology* 272, 233-250.

Naudts, L., Khlystov, O., Granin, N., Chensky, A., Poort, J., De Batist, M., 2012. Stratigraphic and structural control on the distribution of gas hydrates and active gas seeps on the Posolsky Bank, Lake Baikal. *Geo-Marine Letters* 32, 395-406.

Newman, K.R., Cormier, M.-H., Weissel, J.K., Driscoll, N.W., Kastner, M., Solomon, E.A., Robertson, G., Hill, J.C., Singh, H., Camilli, R., 2008. Active methane venting observed at giant pockmarks along the US mid-Atlantic shelf break. *Earth and Planetary Science Letters* 267, 341-352.

Nikolovska, A., Sahling, H., Bohrmann, G., 2008. Hydroacoustic methodology for detection, localization, and quantification of gas bubbles rising from the seafloor at gas seeps from the eastern Black Sea. *Geochemistry Geophysics Geosystems* 9, Q10010.

Ohle, W., 1960. Fernsehen, Photographie und Schallortung der Sedimentoberfläche in Seen. *Arch. Hydrobiol* 57, 135-160.

Olu, K., Sibuet, M., Harmegnies, F., Foucher, J.P., Fiala-Médioni, A., 1996. Spatial distribution of diverse cold seep communities living on various diapiric structures of the southern Barbados prism. *Progress in Oceanography* 38, 347-376.

Ostrovsky, I., McGinnis, D., Lapidus, L., Eckert, W., 2008. Quantifying gas ebullition with echosounder: the role of methane transport by bubbles in a medium-sized lake. *Limnol. Oceanogr.: Methods* 6, 105-118.

Paull, C.K., Ussler, W., Borowski, W.S., Spiess, F.N., 1995. Methane-rich plumes on the Carolina continental rise: associations with gas hydrates. *Geology* 23, 89-92.

Paull, C.K., Ussler, W., Dallimore, S.R., Blasco, S.M., Lorenson, T.D., Melling, H., Medioli, B.E., Nixon, F.M., McLaughlin, F.A., 2007. Origin of pingo-like features on the Beaufort Sea shelf and their possible relationship to decomposing methane gas hydrates. *Geophysical Research Letters* 34(1), L01603.

Paull, C.K., Caress, D.W., Ussler, W., Lundsten, E., Meiner-Johnson, M., 2011. High-resolution bathymetry of the axial channels within Monterey and Soquel submarine canyons, offshore central California. *Geosphere* 7, 1077-1101.

Phrampus, B.J., Hornbach, M.J., 2012. Recent changes to the Gulf Stream causing widespread gas hydrate destabilization. *Nature* 490, 527-530.

Pichot, T., Patriat, M., Westbrook, G., Nalpas, T., Gutscher, M.-A., Roest, W., Deville, E., Moulin, M., Aslanian, D., Rabineau, M., 2012. The Cenozoic tectonostratigraphic evolution of the Barracuda Ridge and Tiburon Rise, at the western end of the North America-South America plate boundary zone. *Marine Geology* 303, 154-171.

Pilcher, R., Argent, J., 2007. Mega-pockmarks and linear pockmark trains on the West African continental margin. *Marine Geology* 244, 15-32.

Pohlman, J.W., Bauer, J., Canuel, E., Grabowski, K., Knies, D., Mitchell, C., Whiticar, M., Coffin, R.B., 2009. Methane sources in gas hydrate-bearing cold seeps: Evidence from radiocarbon and stable isotopes. *Marine Chemistry* 115, 102-109.

Rajan, A., Mienert, J., Bünz, S., 2012. Acoustic evidence for a gas migration and release system in Arctic glaciated continental margins offshore NW-Svalbard. *Marine and Petroleum Geology* 32, 36-49.

Raznitsin, Y.N., 2012. Geodynamics of ophiolites and formation of hydrocarbon fields on the shelf of eastern Sakhalin. *Geotecton.* 46, 1-15.

Reagan, M.T., Moridis, G.J., 2009. Large-scale simulation of methane hydrate dissociation along the West Spitsbergen Margin. *Geophysical Research Letters* 36.

Rehder, G., Brewer, P.W., Peltzer, E.T., Friederich, G., 2002. Enhanced lifetime of methane bubble streams within the deep ocean. *Geophysical Research Letters* 29, 1731.

Rehder, G., Kirby, S.H., Durham, W.B., Stern, L.A., Peltzer, E.T., Pinkston, J., Brewer, P.G., 2004. Dissolution rates of pure methane hydrate and carbon-dioxide hydrate in undersaturated seawater at 1000-m depth. *Geochimica et Cosmochimica Acta* 68, 285-292.

Reid, J., Mantyla, A., 1994. World Ocean Dataset. Available from Scripps Institute of Oceanography: <ftp://minerva.ucsd.edu>.

Revelle, R.R., 1983. Methane hydrates in continental slope sediments and increasing atmospheric carbon dioxide. *Changing Climates*, 252-261.

Riedel, M., Spence, G.D., Chapman, N.R., Hyndman, R.D., 2002. Seismic investigations of a vent field associated with gas hydrates, offshore Vancouver Island. *Journal of Geophysical Research: Solid Earth* 107, 2200.

Roberts, H.H., Hardage, B.A., Shedd, W.W., Hunt Jr, J., 2006. Seafloor reflectivity—an important seismic property for interpreting fluid/gas expulsion geology and the presence of gas hydrate. *The Leading Edge* 25, 620-628.

Römer, M., Sahling, H., Pape, T., Bohrmann, G., Spieß, V., 2012. Quantification of gas bubble emissions from submarine hydrocarbon seeps at the Makran continental margin (offshore Pakistan). *Journal of Geophysical Research: Oceans* (1978–2012) 117(C10).

Rubino, A., Falcini, F., Zanchettin, D., Bouche, V., Salusti, E., Bensi, M., Riccobene, G., De Bonis, G., Masullo, R., Simeone, F., Piattelli, P., Sapienza, P., Russo, S., Platania, G., Sedita, M., Reina, P., Avolio, R., Randazzo, N., Hainbucher, D., Capone, A., 2012. Abyssal undular vortices in the Eastern Mediterranean basin. *Nature Communications* 3, 834.

Sager, W.W., MacDonald, I.R., Hou, R., 2003. Geophysical signatures of mud mounds at hydrocarbon seeps on the Louisiana continental slope, northern Gulf of Mexico. *Marine Geology* 198, 97-132.

Sager, W.W., MacDonald, I.R., Hou, R., 2004. Side-scan sonar imaging of hydrocarbon seeps on the Louisiana continental slope. *AAPG bulletin* 88, 725-746.

Salyuk, A., Obzhirov, A., Li, B., Biebow, N., Suess, E., 2002. Hydroacoustic flare imaging and estimation of the methane flux from an active natural methane vent area on the northern Sakhalin slope. *Terra Nostra* 3, 96–97.

Sauter, E.J., Muyakshin, S.I., Charlou, J.-L., Schlüter, M., Boetius, A., Jerosch, K., Damm, E., Foucher, J.-P., Klages, M., 2006. Methane discharge from a deep-sea submarine mud volcano into the upper water column by gas hydrate-coated methane bubbles. *Earth and Planetary Science Letters* 243, 354-365.

Savini, A., Malinverno, E., Etiope, G., Tessarolo, C., Corselli, C., 2009. Shallow seep-related seafloor features along the Malta plateau (Sicily channel–Mediterranean Sea): Morphologies and geo-environmental control of their distribution. *Marine and Petroleum Geology* 26, 1831-1848.

Schneider, J., Greinert, J., Chapman, N., Rabbel, W., Linke, P., 2010. Acoustic imaging of natural gas seepage in the North Sea: Sensing bubbles under control of variable currents. *Limnology and Oceanography: Methods* 8, 155-171.

Serié, C., Huuse, M., Schødt, N.H., 2012. Gas hydrate pingoes: Deep seafloor evidence of focused fluid flow on continental margins. *Geology* 40, 207-210.

Shipley, T.H., Houston, M.H., Buffler, R.T., Shaub, F.J., McMillen, K.J., Ladd, J.W., Worzel, J.L., 1979. Seismic evidence for widespread possible gas hydrate horizons on continental slopes and rises. *AAPG bulletin* 63, 2204-2213.

Simonetti, A., Knapp, J.H., Sleeper, K., Lutken, C.B., Macelloni, L., Knapp, C.C., 2013. Spatial distribution of gas hydrates from high-resolution seismic and core data, Woolsey Mound, Northern Gulf of Mexico. *Marine and Petroleum Geology* 44, 21-33.

Sloan, E.D., Koh, C.A., 2008. *Clathrate hydrates of natural gases*. CRC Press Llc.

Solomon, E.A., Kastner, M., MacDonald, I.R., Leifer, I., 2009. Considerable methane fluxes to the atmosphere from hydrocarbon seeps in the Gulf of Mexico. *Nature Geoscience* 2, 561-565.

Suess, E., Torres, M., Bohrmann, G., Collier, R., Rickert, D., Goldfinger, C., Linke, P., Heuser, A., Sahling, H., Heeschen, K., Jung, C., Nakamura, K., Greinert, J., Pfannkuche, O., Tréhu, A., Klinkhammer, G., Whiticar, M., Eisenhauer, A., Teichert, B., Elver, M., 2001. Sea floor methane hydrates at Hydrate Ridge, Cascadia margin, in: Paull, C.K., Dillon, W.P. (Eds) *Natural Gas Hydrates: Occurrence, Distribution, and Detection*. AGU, Washington, DC, pp. 87-98.

Talukder, A.R., Bialas, J., Klaeschen, D., Buerk, D., Brueckmann, W., Reston, T., Breitzke, M., 2007. High-resolution, deep tow, multichannel seismic and sidescan sonar survey of the submarine mounds and associated BSR off Nicaragua pacific margin. *Marine Geology* 241, 33-43.

Talukder, A.R., 2012. Review of submarine cold seep plumbing systems: leakage to seepage and venting. *Terra Nova* 24, 255-272.

Thatcher, K., Westbrook, G., Sarkar, S., Minshull, T., 2013. Methane release from warming-induced hydrate dissociation in the West Svalbard continental margin: Timing, rates, and geological controls. *Journal of Geophysical Research: Solid Earth* 118(1), 22-38.

Tomczak, M., Haffner, G.D., Fronaes, E., 2002. False-bottom acoustic echo in mid water? A note on how to evaluate and prevent the interference. *Oceanic Engineering, IEEE Journal of* 27(4), 870-872.

Tomczak, M., Bohrmann, G., Berges, B., White, P., Leighton, T., Wright, I., 2012. Detection, localization and quantification of the emissions of gas from the seabed in fieldwork and experimental studies using active sonar systems, *Proceedings of the 11th European Conference on Underwater Acoustics*, pp. 605-612.

Torres, M., McManus, J., Hammond, D., De Angelis, M., Heeschen, K., Colbert, S., Tryon, M., Brown, K., Suess, E., 2002. Fluid and chemical fluxes in and out of sediments hosting methane hydrate deposits on Hydrate Ridge, OR, I: Hydrological provinces. *Earth and Planetary Science Letters* 201, 525-540.

Tryon, M.D., Brown, K.M., Torres, M.E., Tréhu, A.M., McManus, J., Collier, R.W., 1999. Measurements of transience and downward fluid flow near episodic methane gas vents, Hydrate Ridge, Cascadia. *Geology* 27, 1075-1078.

Tryon, M.D., Brown, K.M., Torres, M.E., 2002. Fluid and chemical flux in and out of sediments hosting methane hydrate deposits on Hydrate Ridge, OR, II: Hydrological processes. *Earth and Planetary Science Letters* 201, 541-557.

Van Dover, C., Aharon, P., Bernhard, J., Caylor, E., Doerries, M., Flickinger, W., Gilhooly, W., Goffredi, S., Knick, K., Macko, S., 2003. Blake Ridge methane seeps: characterization of a soft-sediment, chemosynthetically based ecosystem. *Deep Sea Research Part I: Oceanographic Research Papers* 50, 281-300.

Van Rensbergen, P., De Batist, M., Klerkx, J., Hus, R., Poort, J., Vanneste, M., Granin, N., Khlystov, O., Krinitsky, P., 2002. Sublacustrine mud volcanoes and methane seeps caused by dissociation of gas hydrates in Lake Baikal. *Geology* 30, 631-634.

Veloso, M., Mienert, J., De Batist, M., Greinert, J., 2012. Analysis of the spatial and temporal variability of seep occurrences and activity offshore W-Spitzbergen (Svalbard), EGU General Assembly Conference Abstracts, p. 12341.

Walsh, J.J., Nicol, A., Childs, C., 2002. An alternative model for the growth of faults. *Journal of Structural Geology* 24, 1669-1675.

Weber, T.C., De Robertis, A., Greenaway, S.F., Smith, S., Mayer, L., Rice, G., 2012. Estimating oil concentration and flow rate with calibrated vessel-mounted acoustic echo sounders. *Proceedings of the National Academy of Sciences* 109, 20240-20245.

Weber, T.C., Mayer, L., Jerram, K., Beaudoin, J., Rzhhanov, Y., Lovalvo, D., 2014. Acoustic estimates of methane gas flux from the seabed in a 6000 km² region in the Northern Gulf of Mexico. *Geochemistry, Geophysics, Geosystems* 15, 1911-1925.

Westbrook, G., Smith, M., 1983. Long décollements and mud volcanoes: Evidence from the Barbados Ridge Complex for the role of high pore-fluid pressure in the development of an accretionary complex. *Geology* 11, 279-283.

Westbrook, G., Mascle, A., Biju-Duval, B., 1984. Geophysics and structure of the Lesser Antilles forearc. *Initial Reports Deep Sea Drilling Program, LXXVIII*, 23-38.

Westbrook, G.K., Thatcher, K.E., Rohling, E.J., Piotrowski, A.M., Pällike, H., Osborne, A.H., Nisbet, E.G., Minshull, T.A., Lanoisellé, M., James, R.H., 2009. Escape of methane gas from the seabed along the West Spitsbergen continental margin. *Geophysical Research Letters* 36, L15608.

Zemskaya, T.I., Sitnikova, T.Y., Kiyashko, S.I., Kalmychkov, G.V., Pogodaeva, T.V., Mekhanikova, I.V., Naumova, T.V., Shubenkova, O.V., Chernitsina, S.M., Kotsar, O.V., 2012. Faunal communities at sites of gas-and oil-bearing fluids in Lake Baikal. *Geo-Marine Letters* 32, 437-451.

Zitter, T.A.C., Huguen, C., Woodside, J.M., 2005. Geology of mud volcanoes in the eastern Mediterranean from combined sidescan sonar and submersible surveys. *Deep Sea Research Part I: Oceanographic Research Papers* 52, 457-475.

Quantitative Bathymetry of Godzilla Megamullion, Parece Vela Basin, Philippine Sea

Abstract

Oceanic core complexes represent one of the fundamental modes of accretion of new ocean crust at mid-ocean ridges. Their morphology are controlled by the processes that form the detachment surfaces and serves as a probe into the genetic processes of slow to intermediate spreading in magma-starved environments. Multibeam sonar data were used to investigate the morphology of the largest oceanic core complex identified to date, Godzilla Megamullion. Multiple bathymetric surveys provide a high multibeam echo sounding density that has been used to create surfaces gridded at ~250 m, a high level of precision, and spatial coverage for this region. In total, 40 cruises to the area were collated and processed. Godzilla Megamullion stretches ~150 km from the initiation of asymmetric spreading to termination. Corrugations present on the Godzilla Megamullion and abyssal hills throughout the region define changes in the spreading direction through time. The initiation of asymmetric spreading occurred along two oceanic core complexes that subsequently linked across the entire segment. There is an inverse relationship between the presence of regions of slope parallel and perpendicular to the spreading direction that are interpreted as corrugations and rider block fault scarps, respectively. Smaller en-echelon fractures and faults found in association with rises on the surface of Godzilla Megamullion are particularly common in the medial and proximal portions, and may be related to reaction-driven cracking caused by shallow hydrothermal circulation driven by melt stagnation in the lithosphere.

1. Introduction

Oceanic core complexes are regions of the seafloor that are affected by large-offset low-angle normal faults featuring concomitant tectonic, magmatic, and hydrothermal processes that form a transient plate boundary. Oceanic core complexes are found in association with magma-poor areas of rifts, were first termed ultramafic lifts (Cannat and Casey, 1995), megamullions Tucholke (1998), and later oceanic core complexes (Blackman et al., 1998). The recognition that these seafloor massifs provide a window into the lower crust and mantle, and has spurred fast moving research at slow spreading ridges in recent years. As part of the cruise JC007 (Searle et al., 2007), approximately 50 km² of TOBI sidescan sonar data were collected along the Mid-Atlantic Ridge. The spectacular geophysical images of the corrugated surfaces of oceanic core complexes, and a broad suite of geochemical and geophysical data, provided the foundations for our current understanding of the lifecycle of oceanic core complexes (MacLeod et al., 2009; Mallows and Searle, 2012; Wilson et al., 2013). The oceanic core complexes in the Parece Vela Basin are extremely unusual because they are much larger than other core complexes and formed in a back-arc environment. Godzilla Megamullion at ~150 km is the biggest oceanic core complex identified to date. Extension along the Godzilla Megamullion progressed from the southernmost inactive spreading segment in a southwesterly direction (Ohara et al., 2001). Furthermore, the curvature of the corrugations has also been related to changes in the position of the pole of rotation (Spencer and Ohara, 2014). The surface regions of the megamullion have been divided

into distal, medial, and proximal portions based on bathymetry and geochemical analyses (Harigane et al., 2011; Tani et al., 2011).

2. Background

The steeply dipping normal faults that initiate oceanic core complexes are typical of mid-ocean rift flank faults but form in thin crust within the rift valley. These faults roll over a hinge when the displacement is greater than the strength of the rock (Buck, 1988). The dome-shaped footwall fault surface exposes lower crustal, and with extreme extension, mantle rocks on the seafloor. Oceanic core complex surfaces are corrugated in a direction perpendicular to the ridge axis and rafted rider blocks often clutter the surface. Where serpentinized peridotite is exhumed at the seafloor by oceanic core complexes, mass wasting processes typically create slopes of less than 20° (Cannat et al., 2013). The presence of rafted blocks of basaltic crust on the oceanic core complex surface means that oceanic core complexes may be far more widespread than current observations suggest (Reston and Ranero, 2011). Hydrothermal fluids that flow along the fault plane (McCaig et al., 2007; McCaig et al., 2010) are necessary for the formation of weak minerals such as talc and serpentine that facilitate runaway slip along low-angle detachment faults (Escartín et al., 1997). The amount of extension accommodated by oceanic core complexes can be from 10's to 100's km and can accommodate up to 100% of the spreading rate (Grimes et al., 2008). Oceanic core complexes have been found in every ocean basin (Mallows, 2011).

Numerical models of asymmetric seafloor spreading suggested that melt supply played a major role in the evolution of oceanic core complexes (Tucholke and Lin, 1994; Tucholke et al., 2008). These ideas were supported by field-based observations (MacLeod et al., 2009; Mallows and Searle, 2012) using acoustic backscatter that showed when oceanic core complexes are active, their location is correlated with a lack of magma supply, and that the adjacent rift valley is totally amagmatic until the encroachment of the neovolcanic zone back into the ridge axis adjacent to an oceanic core complex terminates its development. This led to the understanding that melt supply controls the first-order structural evolution of oceanic core complexes (Mallows and Searle, 2012; Sauter et al., 2013; Smith, 2013), and that mantle chemistry is an important underlying factor in their development (Loocke et al., 2013; Wilson et al., 2013). Central to this life-cycle is the idea that tectonic extension, magmatism, and hydrothermal activity is strongly 4D, not only controlled spatially in three dimensions by the position of the actively developing core complex, but also shows temporal variation. In asymmetric segments, the separation style varies along axis from tectonic to magmatic over distances of ~10's km.

Godzilla Megamullion is a vast oceanic core complex that stretches 160 km in length (Ohara et al., 2001). As part of this study, cruises to the Parece Vela Basin have been used to help map the oceanic core complex accurately and analyze the morphology. By integrating all of the publicly available data from JAMSTEC, we were able to determine the three-dimensional morphology, quantify variations in bathymetry character, and evaluate how the identified features provide insights into the initiation, development, and termination of a giant oceanic core complexes.

3. Location and Geology

The Parece Vela Basin is a back-arc basin situated in the southeastern Philippine Sea (Fig. 2.1). Development of the basin occurred in three main stages: 1) trench formation, 2) arc volcanism, 3) rifting, and 4) back arc spreading (Karig, 1971). Based on rift geometry, marine magnetic data and volcanic ages, the basin has been divided into western and central domains (Ohara et al., 2011). The western part of the basin was actively spreading up to 21 Ma at a rate of ~ 80 mm/yr with an east-west extension direction. The western basin contains symmetrically spread basaltic crust and a region a distinct region of asymmetric spread crust that hosts numerous oceanic core complexes termed the Chaotic Terrain (Ohara et al., 2001). The central basin is defined magnetic anomaly 6A and lies to the east of 138°E . Due to its equatorial position interpretation of magnetic anomalies in the Parece Vela Basin is challenging. The extension direction changes to a northeast-southwest direction and stair-step ridges developed to accommodate the change in spreading direction. The extinct axis of the spreading ridge has been divided into 7 first-order segments offset by en-echelon fracture zones (Ohara et al., 2001; Ohara et al., 2011). The three most southerly segments (S3, S2, and S1) host oceanic core complexes (Ohara et al., 2001), and Godzilla Megamullion is located in southernmost segment (S1).

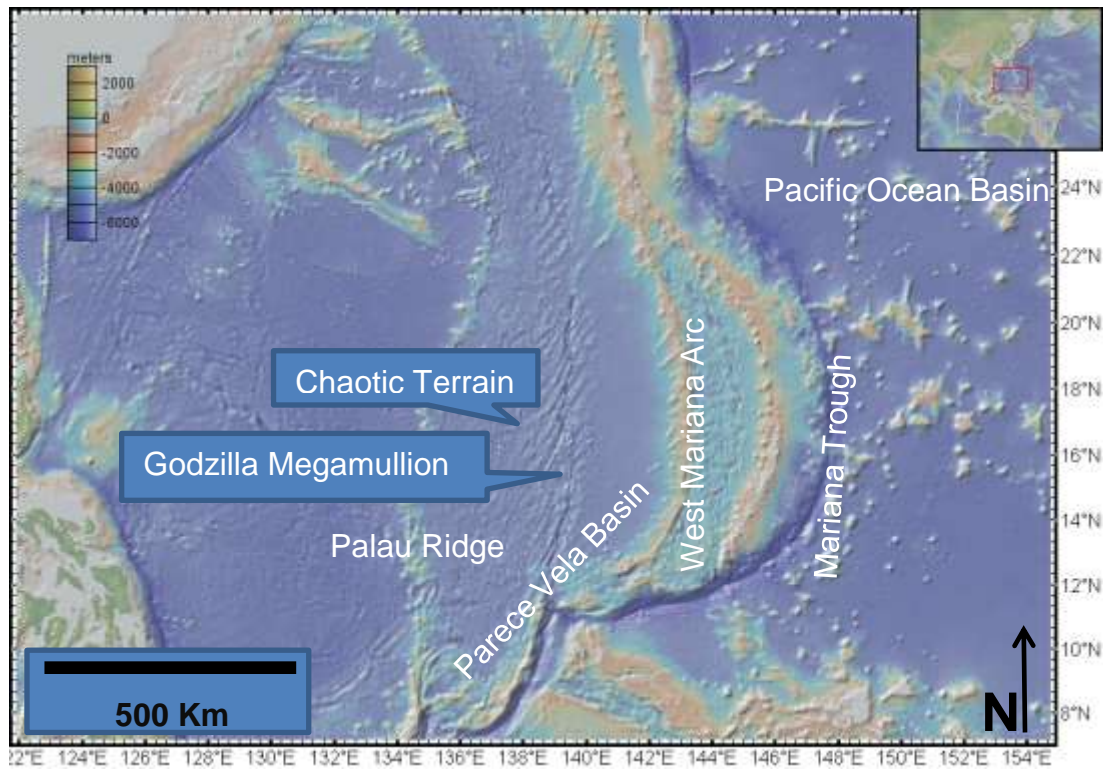


Figure 2.1. Location map for the Godzilla Megamullion in the Philippine Sea.

4. Methods

Data were downloaded from the Data Research System for Whole Cruise Information (DARWIN) database available through the Japan Agency for Marine-Earth Science and Technology (JAMSTEC). Data used in this study was acquired as part of the following research cruises: KR98-01, KR98-12, KR02-14, KR03-01, KR03-04 Leg 2, KR04-14 Leg 2, KR05-14, KR05-16, KR06-11, KR06-13, KR06-14, KR08-05 Leg 1, KR08-15, KY01-11 Leg 2, MR00-K04, MR00-K07 Leg 34, MR01-K05 Leg 12, MR01-K05 Leg 34, MR02-K04, MR02-K06, MR04-01, MR04-03 Leg 1, MR05-03 Leg 3, MR09-01 Leg 3, MR06-05 Leg 3, MR07-03, MR10-02, MR10-03 Leg 1, MR10-03 Leg 2, MR11-06,

MR11-08 Leg 2, MR98-K02, MR99-K03, YK00-01, YK02-07 Leg 2, YK03-09 Leg 2, YK05-09 Leg 1, YK10-14, YK09-08, YK09-05, YK06-11, YK11-08, YK12-11. This dataset provides almost complete coverage of the Godzilla Megamullion. Further cruises may be integrated into the database at a future date to complete the more regional coverage. The data were loaded into QPS-SAAB modules for processing and analysis. Where necessary file formats were converted and processing steps conducted in MBsystems (Caress and Chayes, 1995). Using the Dmagic module a giant Pure File Magic area-based editing database was created. From this database, surfaces were exported that maintained an editable relationship between the soundings and the surface bins. The created bathymetric surface was gridded at 250 m. Data were then loaded into the Fledermaus module for visualization and analysis in 3D. Bathymetric maps were integrated with slope maps to interpret geologic features. The slope map is created by computing the slope for each cell center based on the relationship to cell neighbors (north, east, south and west) and then calculating as an arctan function slope in degrees from horizontal. Using this method a 90° slope is vertical.

A widget is used to identify azimuthal direction of the view and as a scale for distances. The widget has a vertical component that provides the view angle in degrees from horizontal. The horizontal component provides the view direction as a bearing using the azimuth system. Vertical and horizontal scale bars provide 3D dimensions for the image, where the vertical scale and the horizontal are in either m or km depending on the size of the region being studied. Where not labelled by a widget, north is always

towards the top of the page. Where accompanying a color ramp, the 2D profiles include the same color ramp.

5. Results

5.1 Morphology of the Godzilla Megamullion

Depths in the Godzilla region range from ~6800 m in the west-bounding transform deep to a shoal of ~2400 on the shoulder of the oceanic core complex termination (Fig. 2.2). Along its length corrugations divide the surface, and their orientations have changed through time, parallel with the spreading direction. The corrugations have wavelengths of ~4 – 10 km. The oceanic core complex extends for 150 km and is 60 km wide and has been divided into 13 morphotectonic regions (Ohara and Snow, 2009; Harigane et al., 2011). In this paper we discuss the morphology of each of the identified regions in order from the breakaway through oldest to youngest, to the termination.

5.2 Lithology of the Godzilla Surface from Dredge and Dive Samples

Dredge and dive samples were collected from 39 locations on the Godzilla Megamullion surface and recovered peridotite, gabbro, and basalt (Fig. 2.3). These samples were collected during cruises YK03-09 Leg 2, KR03-01 and KH07 Leg 2. The average totals for all of the rocks collected were peridotite 236 kg (~38%), gabbro 173 kg (~28%), and basalt 213 kg (~34%). Most of the basalt and gabbro was collected from crust with abyssal hill-like structure, and the peridotite from regions of smooth or corrugated seafloor.

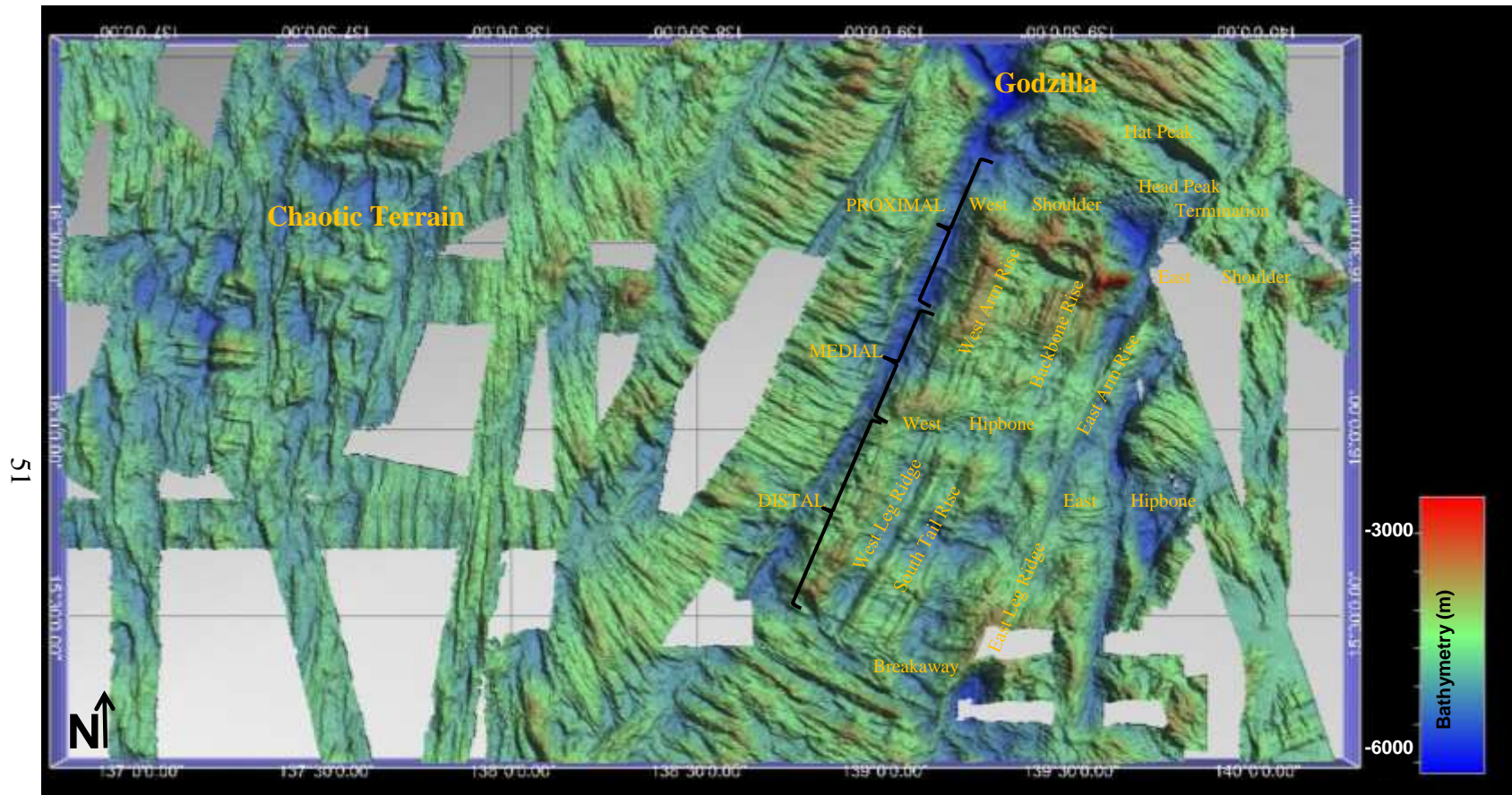


Figure 2.2. Bathymetry of the Godzilla region annotated with names of important features discussed in text.

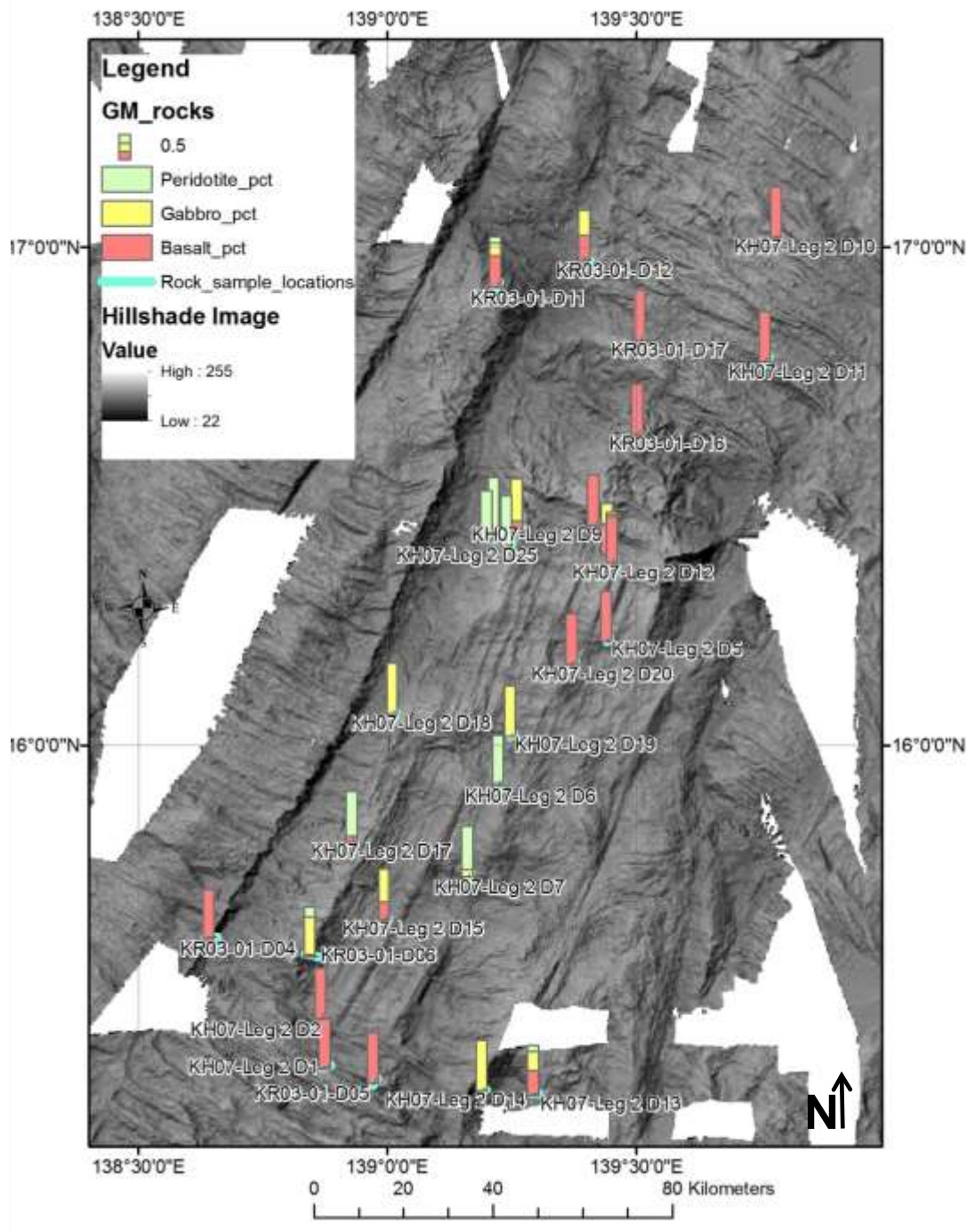


Figure 2.3. Dredge and dive sample locations and sample lithology from the Godzillia Megamullion surface (pct = percentage).

5.3 Distal Section

5.3.1 Breakaway

Godzilla Megamullion initiated along a ridge-flank normal fault that subsequently developed much greater displacement than length when compared to normal fault growth models, resulting in an oceanic core complex. The breakaway region is predominantly basaltic rocks that form two bathymetric highs with a central deep basin (Figs 2.4 & 2.5). There are no corrugations on the bathymetric highs and their surfaces are blocky, suggesting that they are overlain by volcanic rider blocks.

The corrugated surfaces develop at the breakaway and continue into the distal portions of the oceanic core complex. The breakaway as shown in figures 2.4 & 2.5 has significant relief along its length varying from ~5700 m in two discontinuous basins to ~4200 m on two breakaway highs. From their morphologic character the two highs in the central depression appear to be pre-megamullion oceanic core complexes that were terminated when Godzilla started to breakaway across the entire segment. The axial trace of the Godzilla breakaway surface is interpreted to lie along line A (Fig 2.4). On the opposing margin there are three fault scarps typical of symmetric spread crust that have elevation of ~1000 m and slopes $> 28^\circ$. Fault scarps in the 6 km adjacent (southwest) of the breakaway have slopes greater than 28° , making them steeper and higher than other faults in symmetric spread crust in this region. The long linear abyssal hill topography with steep slopes indicates that this region was created during magmatically robust spreading.

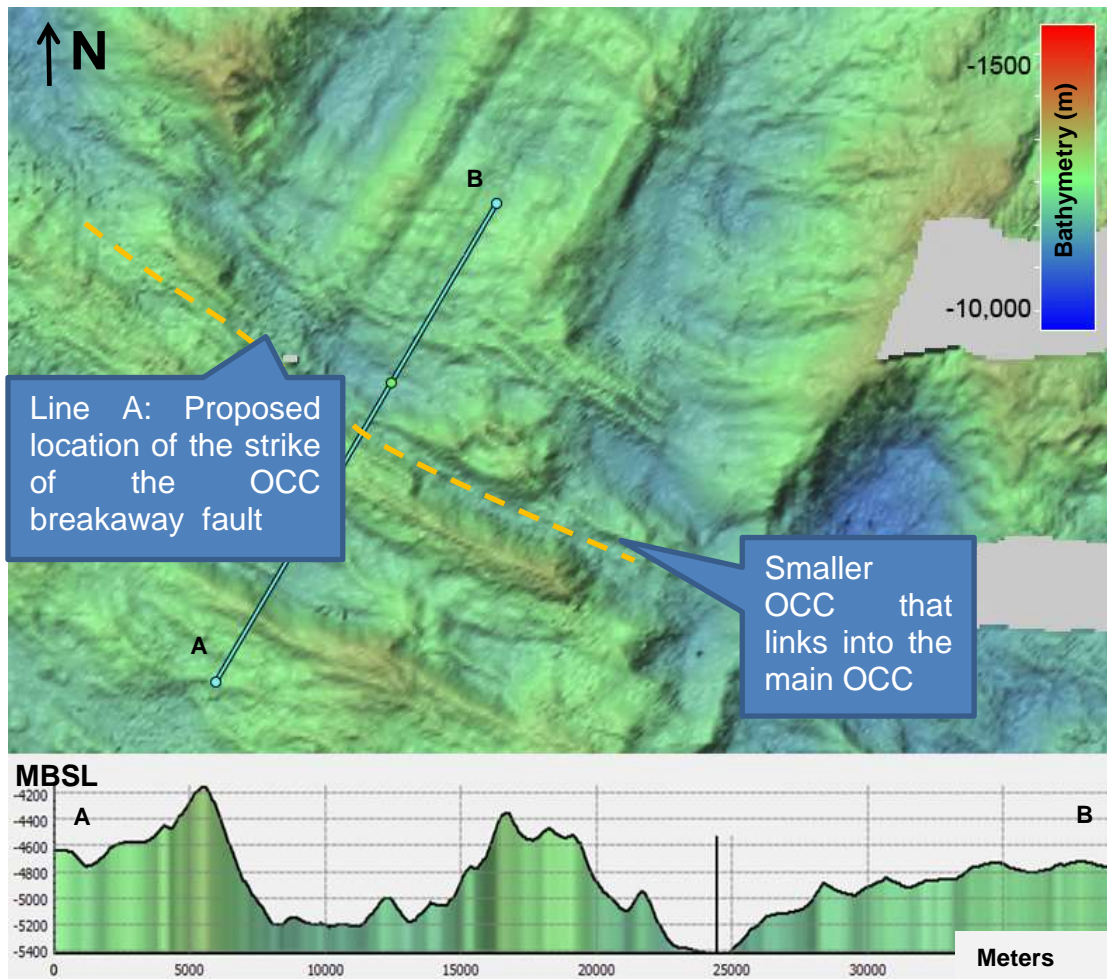


Figure 2.4. . Location of the breakaway, OCC = Oceanic Core Complex.

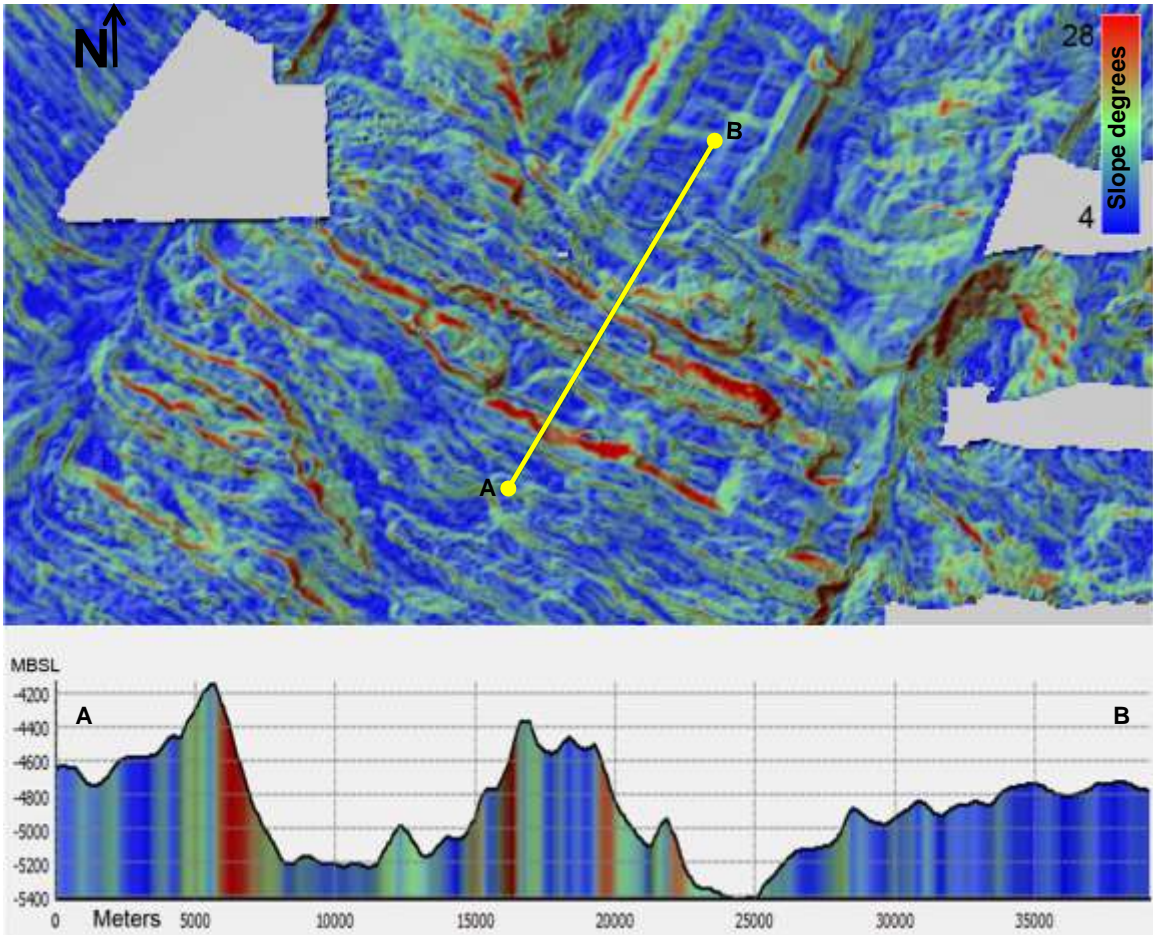


Figure 2.5. Slope map of the breakaway location.

5.3.2 West Leg Ridge

West Leg Ridge is 60 km long 20 km wide bathymetric high with several triangular shaped promontories along its length (Figs 2.6 & 2.7). The shoalest sounding used to create the bathymetric surface on this part of the ridge is adjacent to the breakaway low (3800 m), and the depth increases to ~4700 m close to Hip Bone Ridge high. Generally the ridge has shallower slopes (~7°) on the western margins where it is bounded by a transform fault, and a steeper slope (~16°) on the southeastern side. The slope map

defines well-developed corrugations along the southeast facing wall and along the ridge axis. The corrugations are oriented at $\sim 033^\circ$ up to the location of Hip Bone Ridge where the orientation changes.

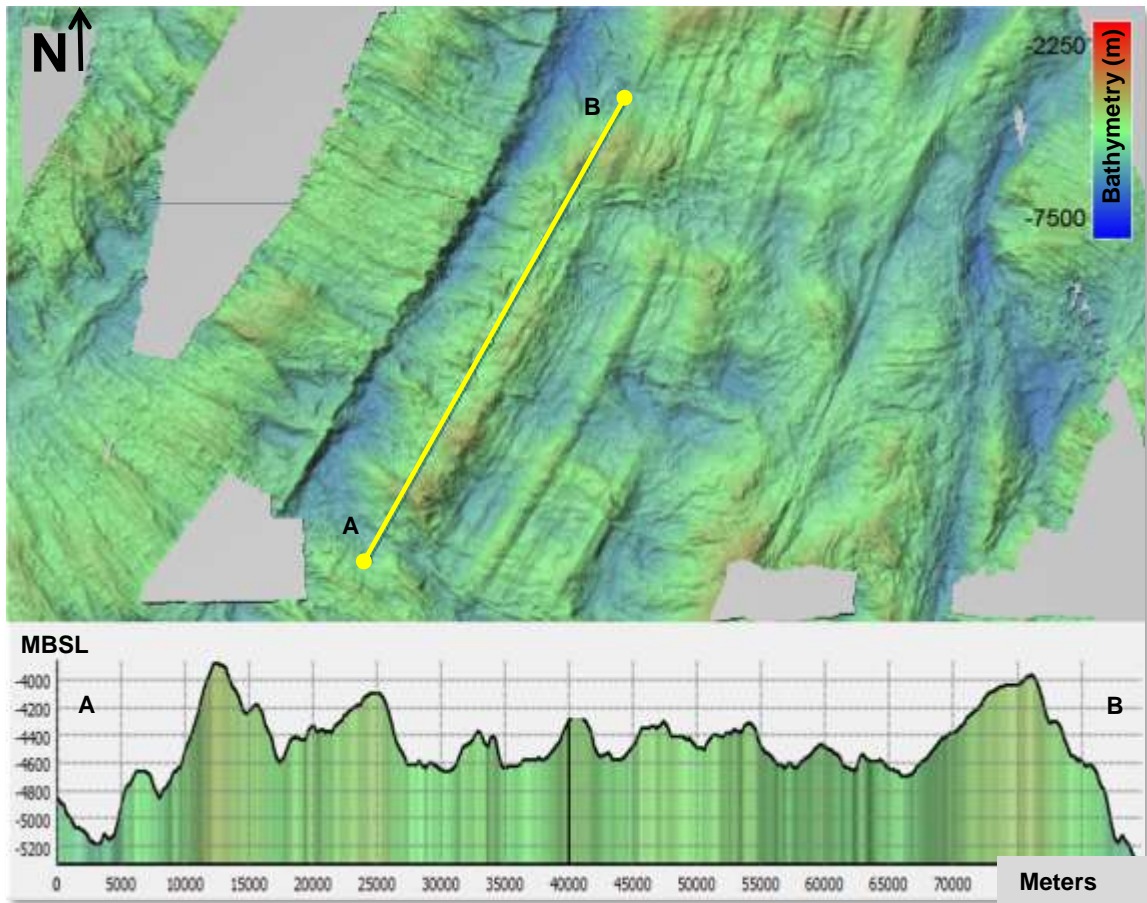


Figure 2.6. Bathymetry of West Leg Ridge.

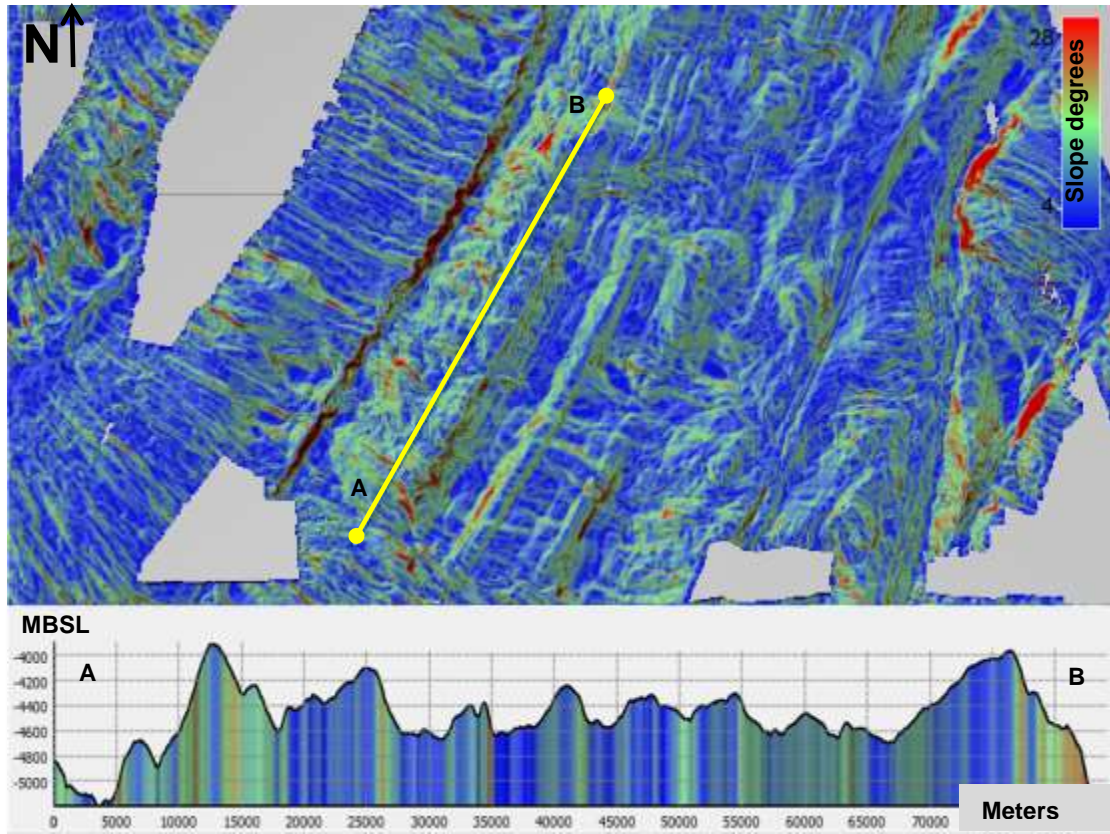


Figure 2.7. Slope map of West Leg Ridge.

5.3.3 South Tail Rise

South Tail Rise is a cylindrical, segment-shaped ridge that extends ~30 km from the breakaway and is connected to Backbone Rise (Fig. 2.8). South Tail Rise connects to North Tail Rise in a bathymetric depression (~5000 m) that is the contact between two different ridge orientations. The orientation of the ridge axis changes in the deepest part. From the breakaway along the first 30 km of South Tail Rise the ridge follows an orientation similar to West Leg Ridge (33°), whereas along North Tail Rise the orientation changes to ~27°.

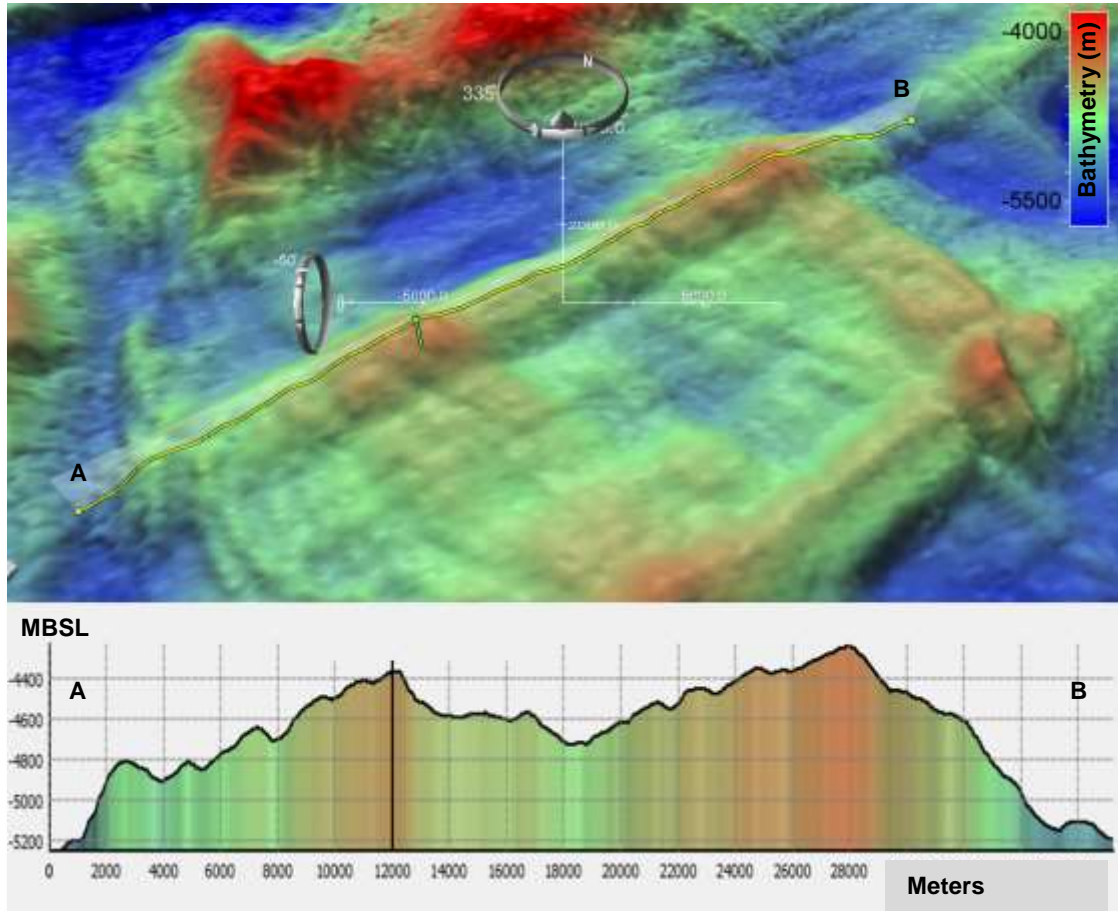


Figure 2.8. Bathymetry of South Tail Rise.

5.3.4 East Leg Ridge

Unfortunately there is a large section of East Leg Rise missing due to lower sounding data density in this region. East Leg Ridge is defined by bathymetric highs found close to the breakaway and similar to those found on West Leg Ridge (Fig. 2.9). In contrast to West Leg Ridge, the shallowest slope is on the northwestern edge, and the steepest slope along the transform boundary.

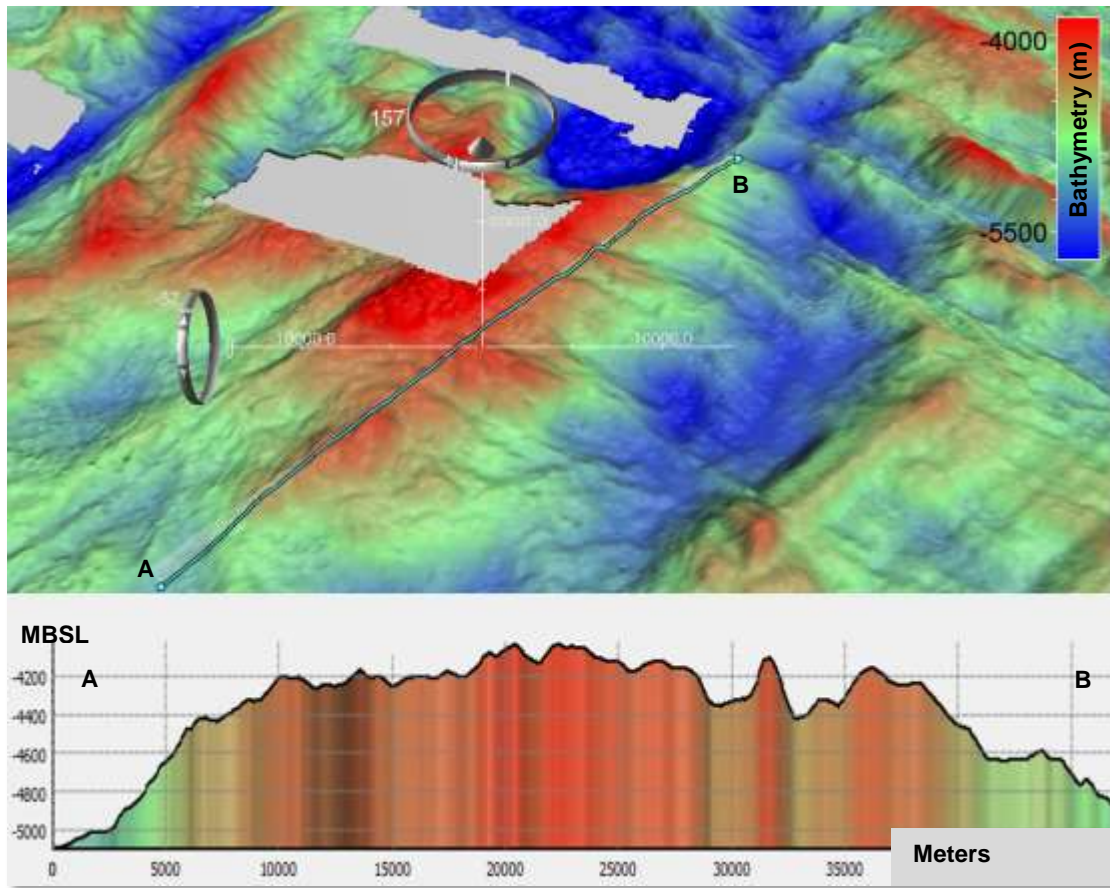


Figure 2.9. Bathymetry of East Leg Ridge.

The east-bounding transform has a narrow bathymetric expression, as characterized in the slope map, when compared to the west-bounding transform boundary. Due to the hummocky nature of the structural grain in this area and lack of corrugations determining the orientation of spreading in this region, it is assumed to have had a similar structural history to Tail Rise. Several circular regions of high slope with central craters with low slope have been identified in this area using the slope map (Fig. 2.10). These features are typically a few km wide by 500 – 100 m tall and may be related to seafloor volcanism adjacent to the transform.

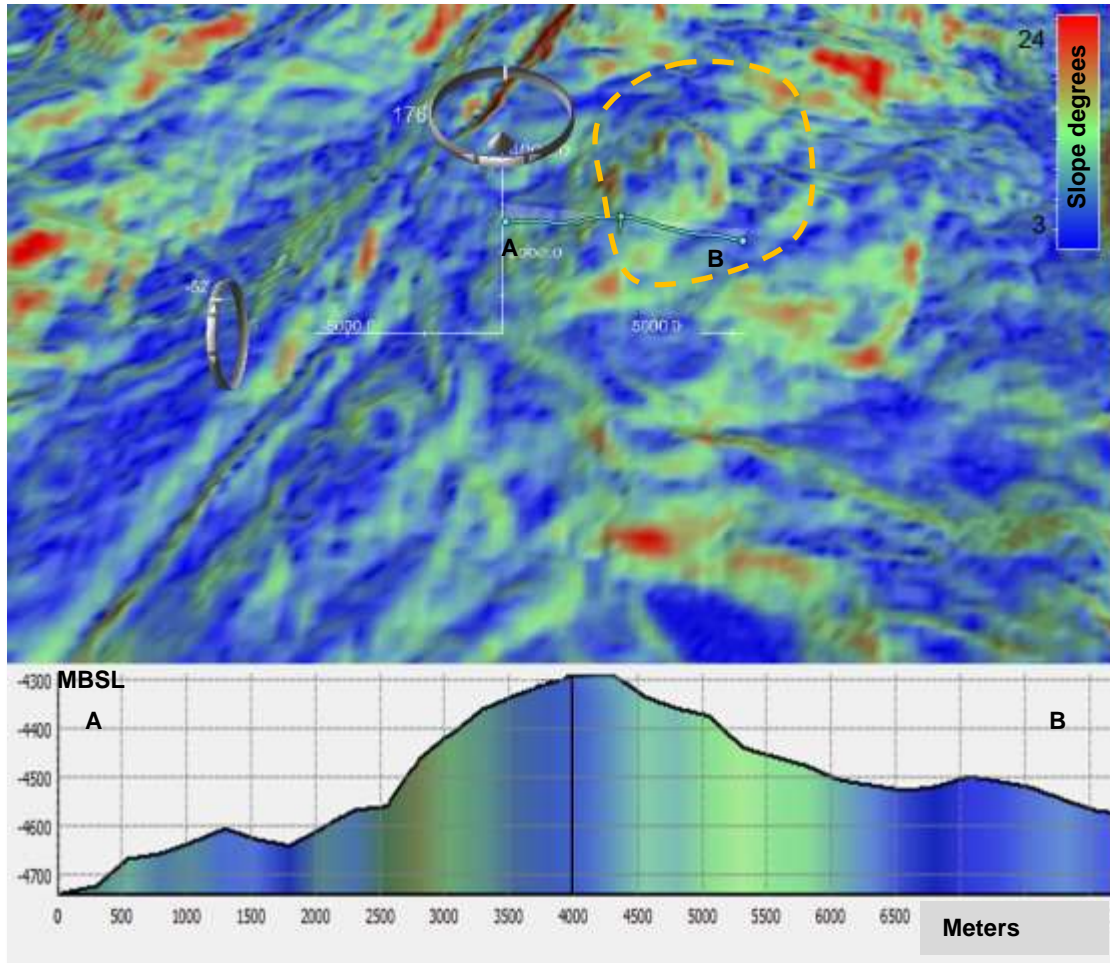


Figure 2.10. Slope map of possible volcanic features in the East Leg Ridge region.

5.4 Medial Section

5.4.1 North Tail Rise

North Tail rise is a continuation of South Tail Rise. Before transitioning into Backbone Rise there are two large circular features have been identified using the slope map that both have central craters. These features have steep outer slopes $>20^\circ$. In 3D view of the raw data two multibeam swath lines can be seen, represented by green and

orange dots (pings) (Fig. 2.11). Because the data in both lines shows the crater morphology it is unlikely that the crater is an artifact. The origins of this feature are unknown and may be related to lava, or mud, volcanism.

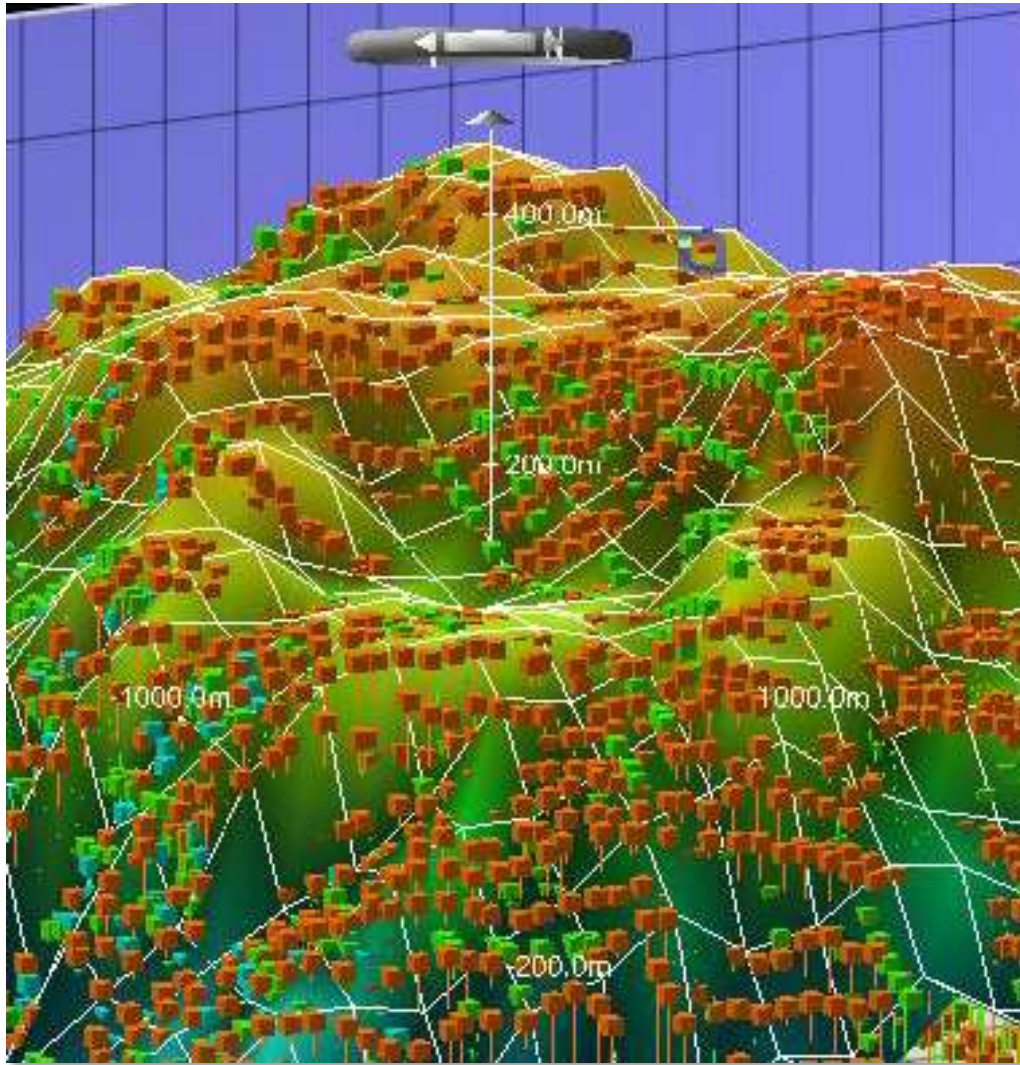


Figure 2.11. Soundings used to image the surface of volcanic features at the terminal end of South Tail Rise.

5.4.2 West Hipbone Rise

West Hipbone Rise is dome shaped, approximately 20 x 17 km in dimensions, and has slopes less than 20° (Figs. 2.12, 2.13 & 2.14). The southern edge of the West Hip Bone Rise massif is bounded by several steep slopes (~20°). The steep slopes have an elliptical morphology typically associated with fault displacement/length ratios and relay ramps (Dawers and Anders, 1995; Walsh et al., 2002) (Fig. 2.13).

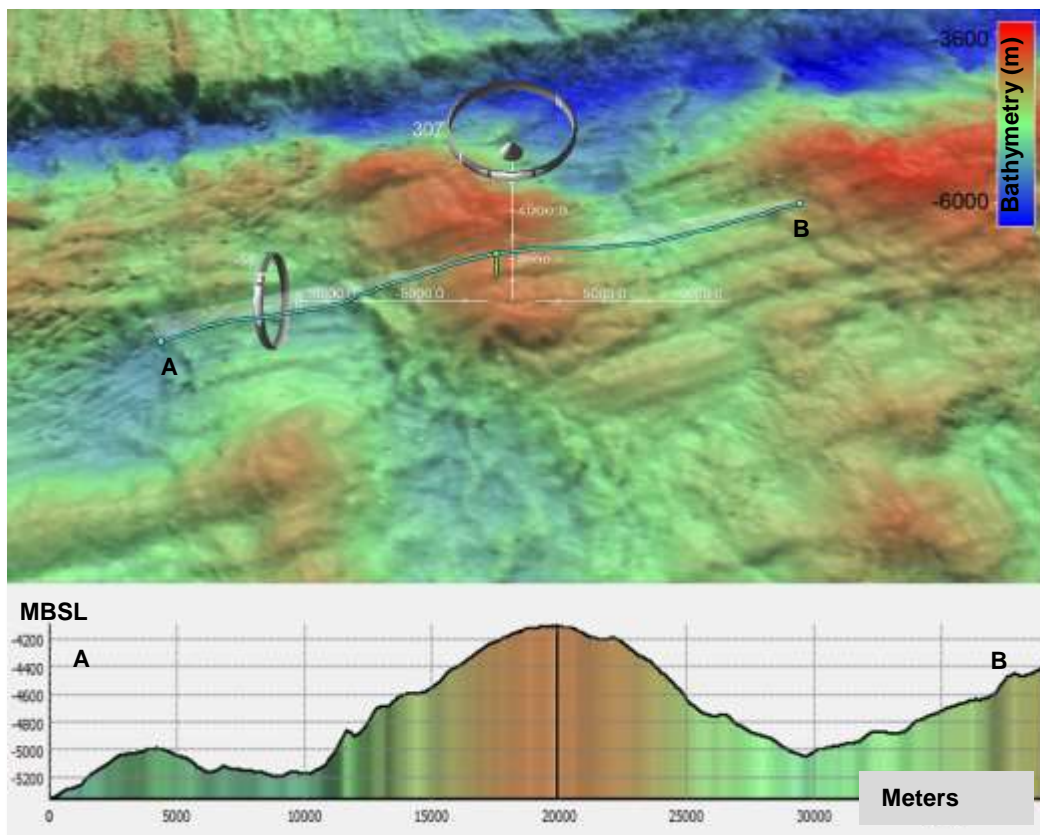


Figure 2.12. Bathymetry of West Hipbone Rise.

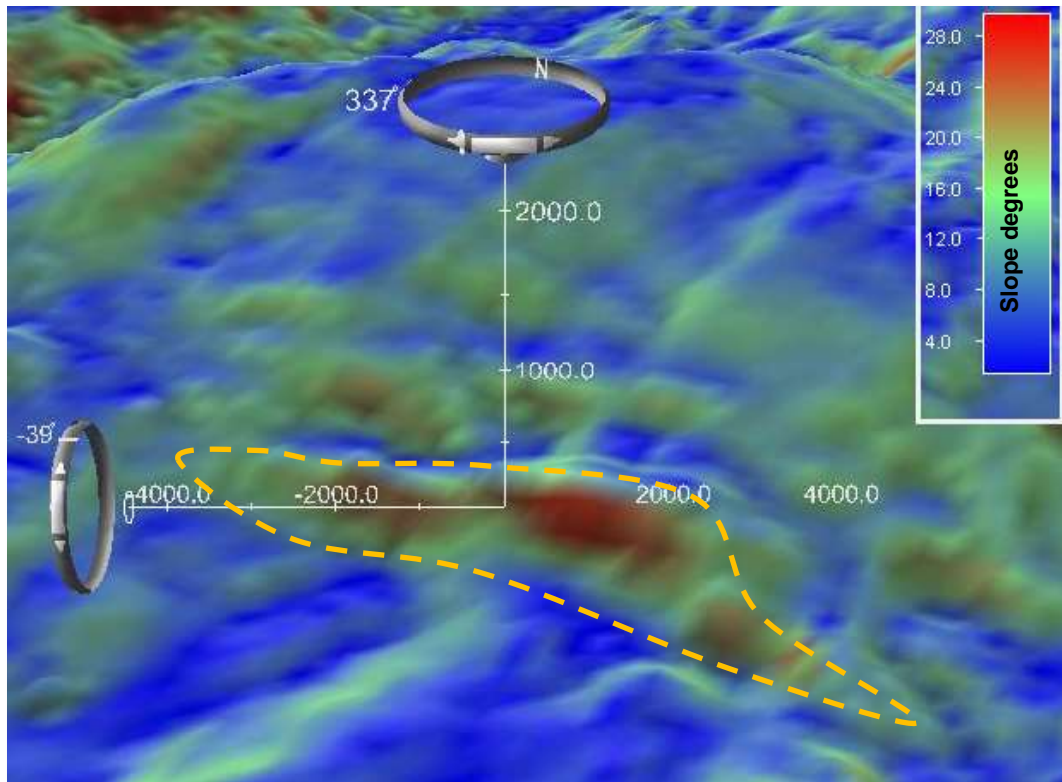


Figure 2.13. Fault scarp on West Hipbone Rise.

Measurements of fault surfaces in this region give a length/displacement ratio of ~ 9 , placing them within the ranges of established the fault growth models. On the northwestern corner of the massif steep slopes leading down into the transform valley appear to have been formed by mass-wasting processes (Fig. 2.14). The region of mass wasting is a scallop-shaped region that's surface is cut by numerous fault planes.

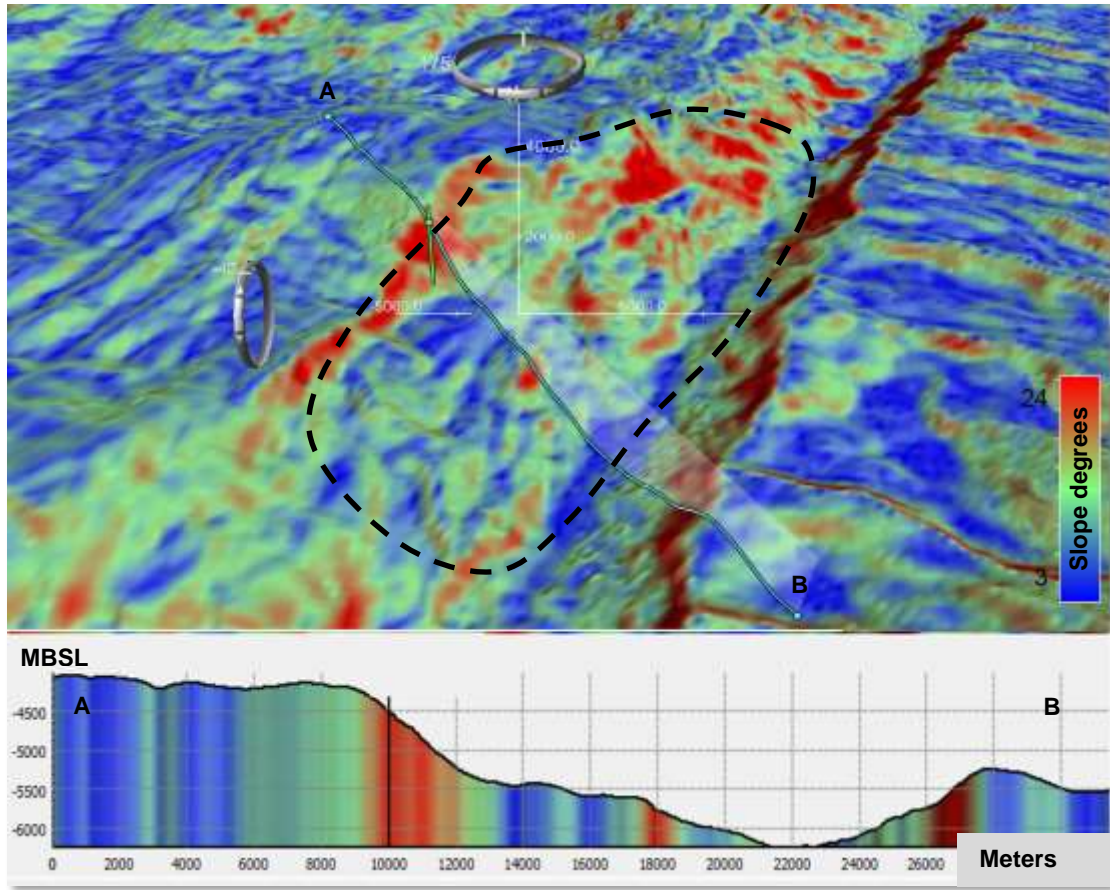


Figure 2.14. Dashed line highlights region of seafloor failure on West Hipbone Rise.

5.4.3 East Hipbone Rise

East Hip Bone Rise is a dome shaped bathymetric profile and the main rise is about 12 km square and has ~1000 m of relief (Fig. 2.15). The rise has a curvilinear surface expression that may be the result of seafloor mass-wasting processes. The region of mass wasting is characterized by a blocky, fragmented, and discontinuous region bounded and cut by numerous faults. The observation of long linear ridges downslope from the main promontory suggests a failure mechanism for their origin (Fig. 2.16).

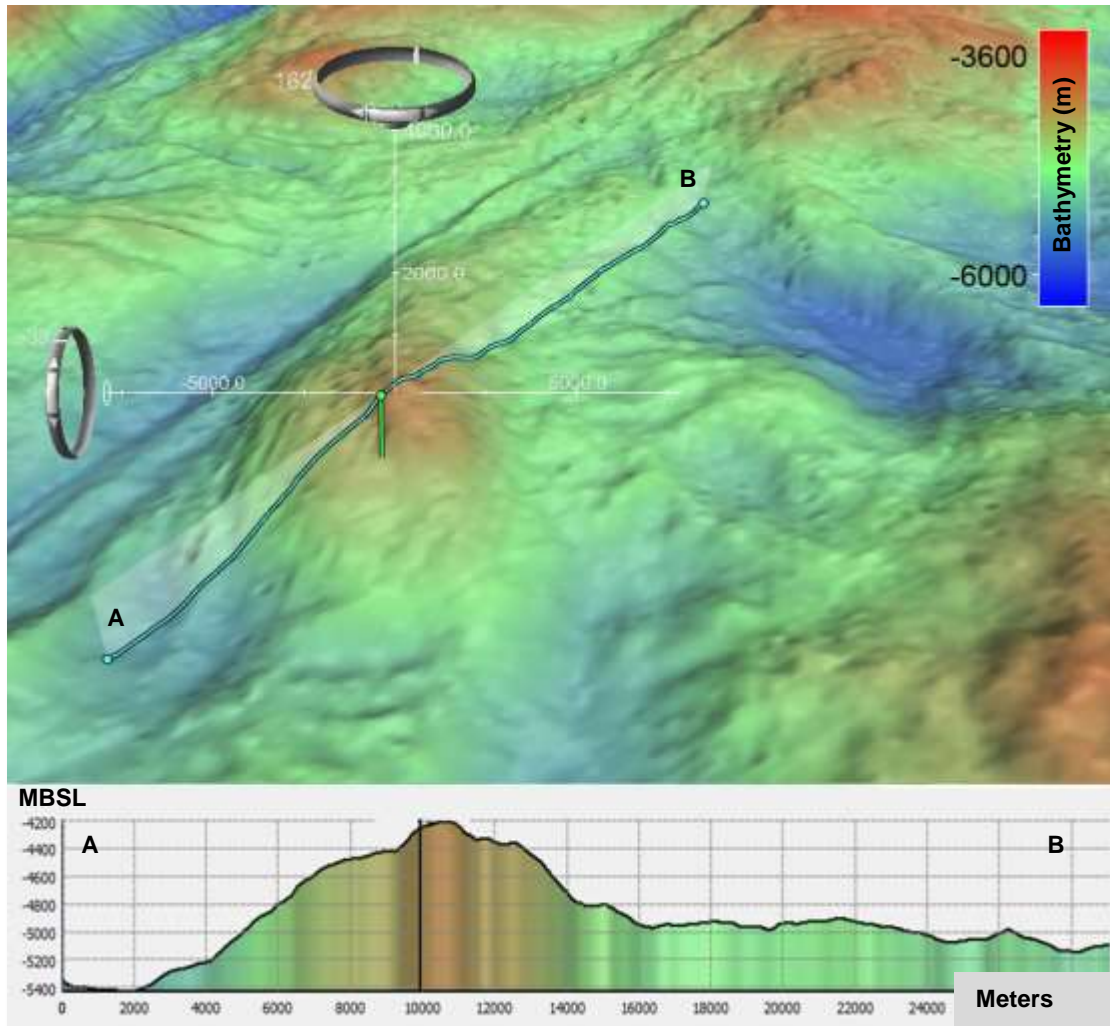


Figure 2.15. Bathymetry of East Hipbone Rise.

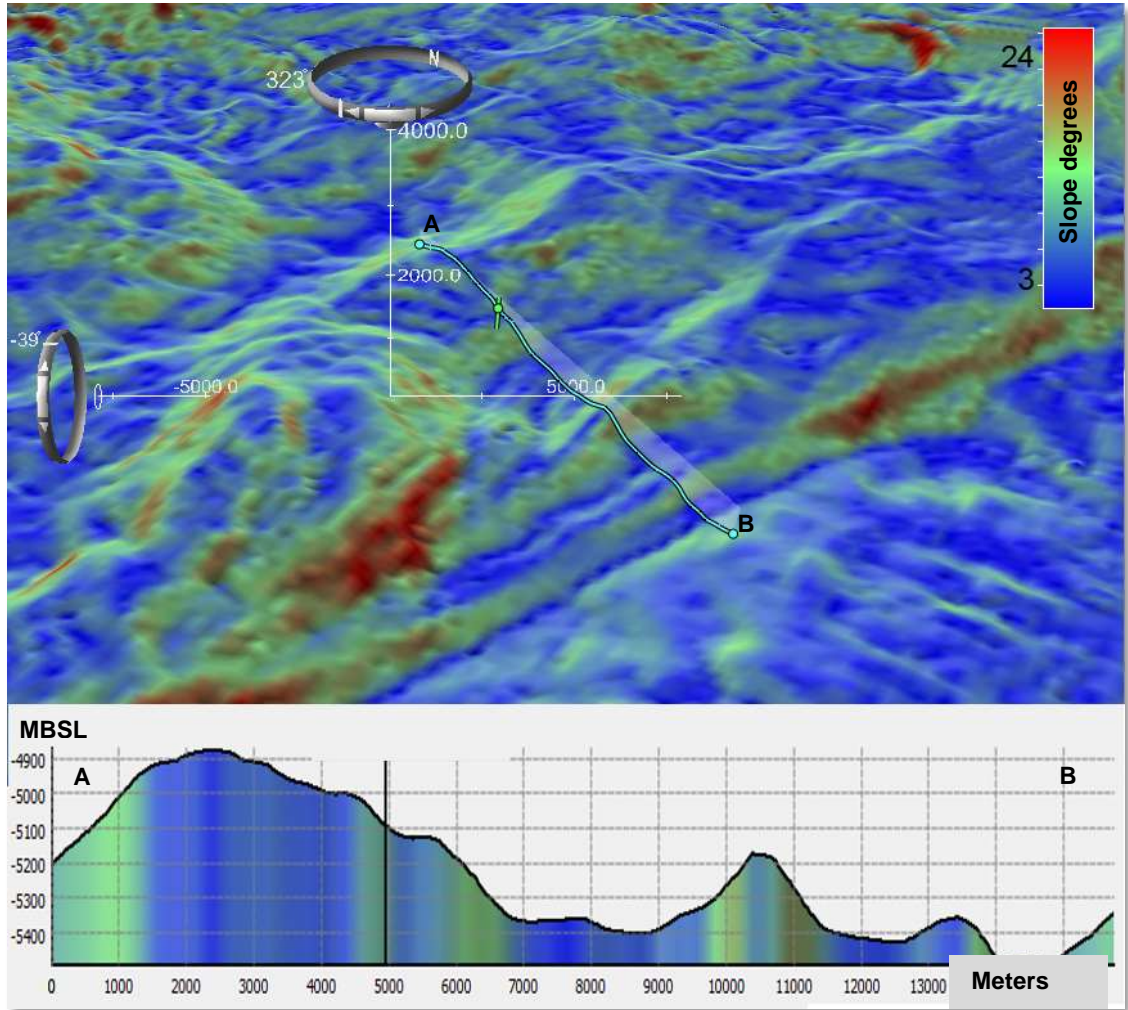


Figure 2.16. Slope failure on East Hipbone Rise.

5.5 Proximal Section

5.5.1 West Arm Rise, Backbone Rise, and East Arm Rise

The bathymetry shoals from the Hip Bone Rises to the Backbone and Arm Rises. Corrugations that were present in the distal and Hip Bone regions are better defined through the Backbone and Arm Rises. The corrugations are cut by en-echelon (280°)

faults. The fault scarps have slopes of between $12 - 25^\circ$ and the slopes on the back side of the scarps (back tilted surface) from $1 - 25^\circ$. Where the normal faults cross cut the topographic highs of the Arm and Backbone Rises, the corrugations are less pronounced. West Arm Rise is unique in that mylonites are only found in this region (Harigane et al., 2011), suggesting that in this portion of the oceanic core complex the detachment fault surface is preserved. In this segment the measured along corrugation is $\sim 25^\circ$, suggesting that the spreading direction was $\sim 25^\circ$ during its formation. The western transform boundary widens and deepens in this region. Widening and deepening of the transform boundary suggests that there was an extensional component to the spreading in this region.

5.5.2 East and West Shoulder Ridges

The East and West Shoulder Ridges are connected via SSW-dipping escarpments that cross the width of the corrugated surface (Fig. 2.17). The corrugations cease at the start of these linear features and remain absent up to the terminal rift valley. In the central part of Godzilla the linear ridges are perpendicular to the spreading direction. At the transform margins of both shoulder highs, the tips are rotated towards the now extinct spreading axis. The rotation of the ridge tips can also be observed on the conjugate flank, Hat Ridge. These two rotated linear ridges form a bowl-shaped feature around Godzilla's Head and Neck Rises. In contrast, the generalized bathymetry of Godzilla features western ridges at shallower depths with the East Shoulder High containing the shoalest sounding on the surface (~ 2500). The southeastern transform boundary widens and deepens adjacent to the East Shoulder Ridge.

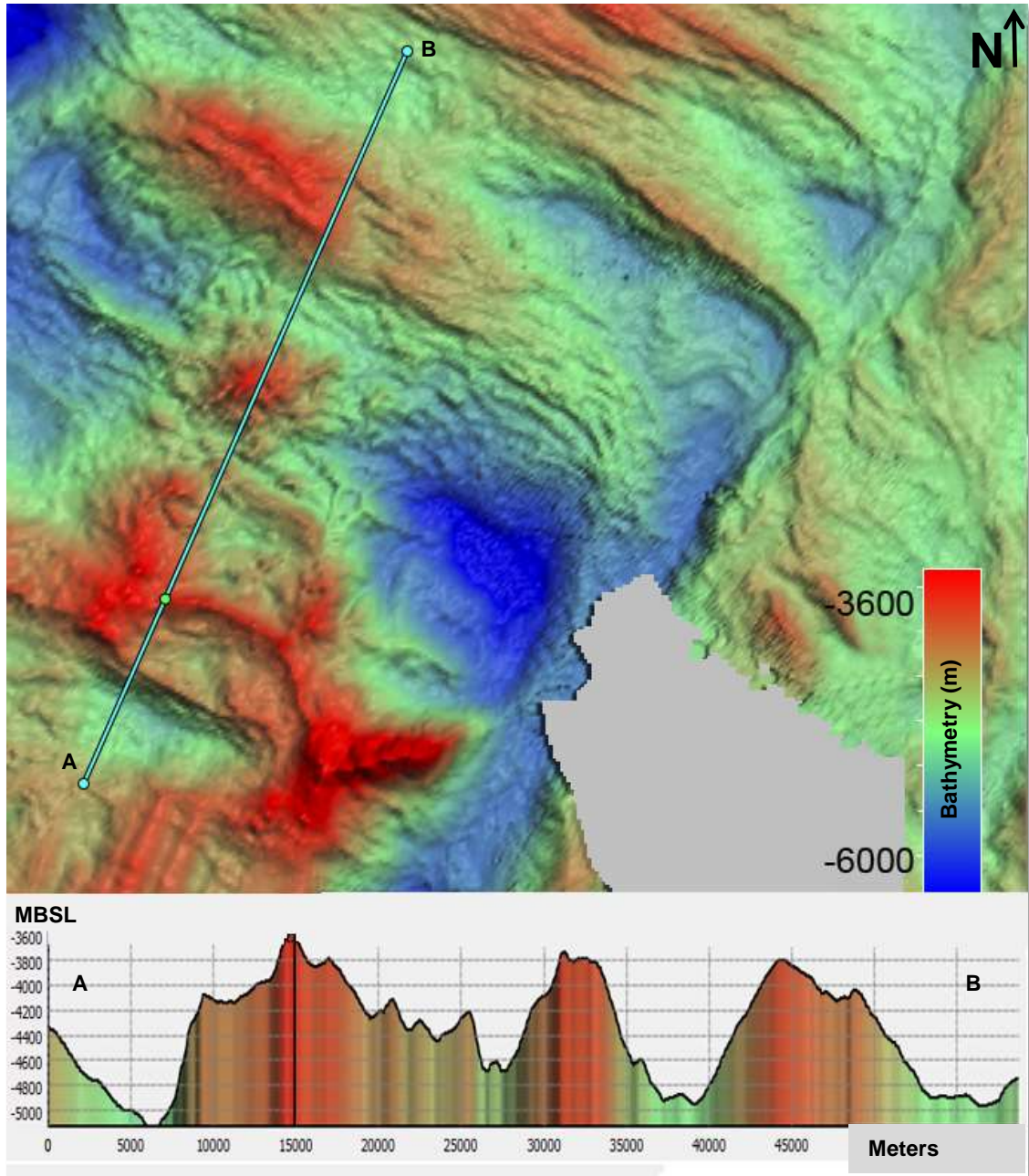


Figure 2.17. Bathymetry of East and West Shoulder Ridge and the termination.

5.5.3 Termination

The cessation of volcanism at Head Peak was the end of Godzilla Megamullion expansion and subsequent tectonic stretching caused the termination rift flanking fault tips to rotate inwards towards the termination.

5.5.4 Neck Peak and Head Peak

The Neck and Head Peaks are isolated peaks within a region of deep bathymetry where the transform margins become wider and deeper (Figs. 2.18 and 2.19). Basalts from Head Peak returned ages of 4.8 Ma (Ishizuka et al., 2004). The terrain in this region has bathymetry associated with eruptive hummocks, the building block of mid-ocean ridges (Yeo et al., 2012). Numerous circular cratered regions have been identified in the bathymetry and slope map. The region of hummocky slope fills the central parts of the deep basin but does not reach to the transform margins. Head Peak rises to ~3500 m water depth and has deep basins either side (~6400 m).

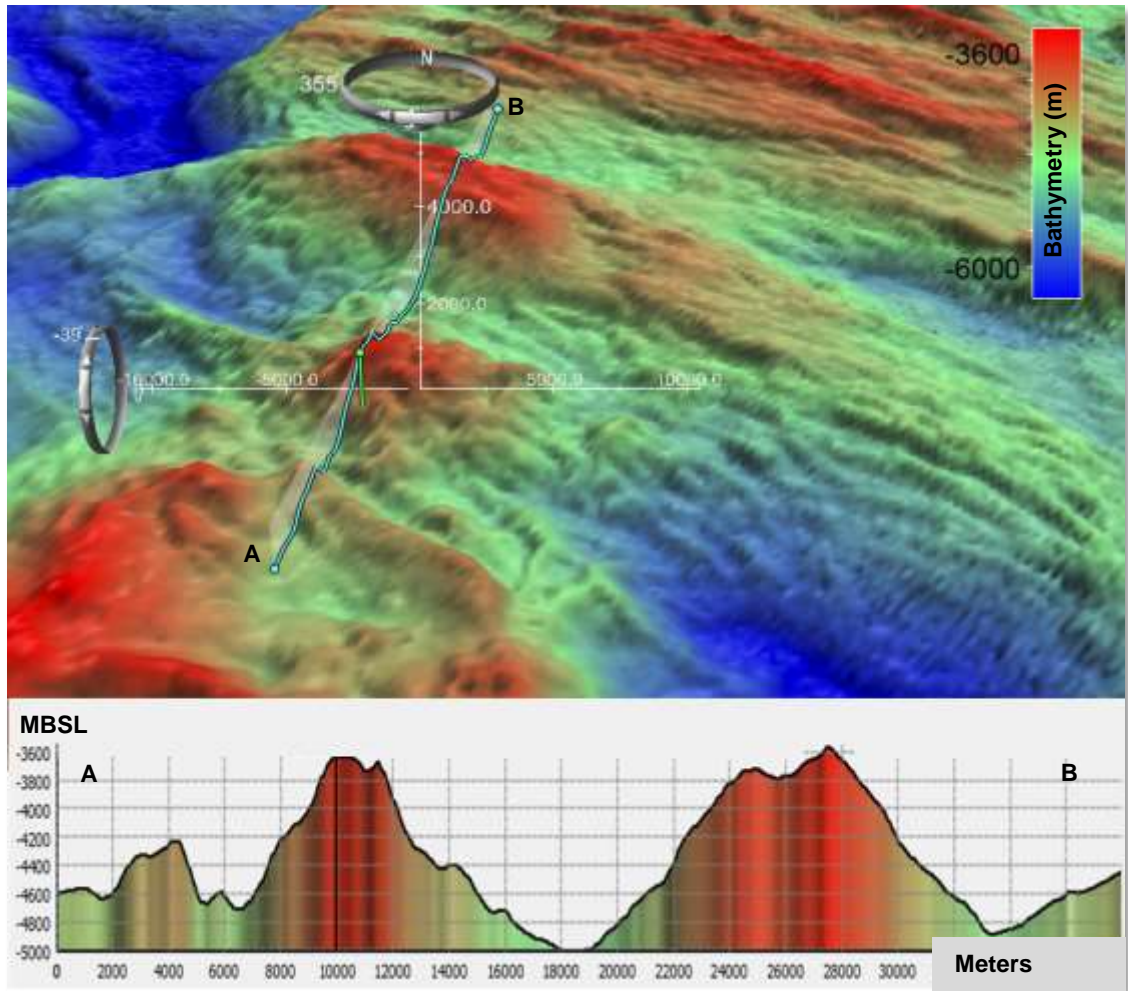


Figure 2.18. Bathymetry of Neck and Head Peaks.

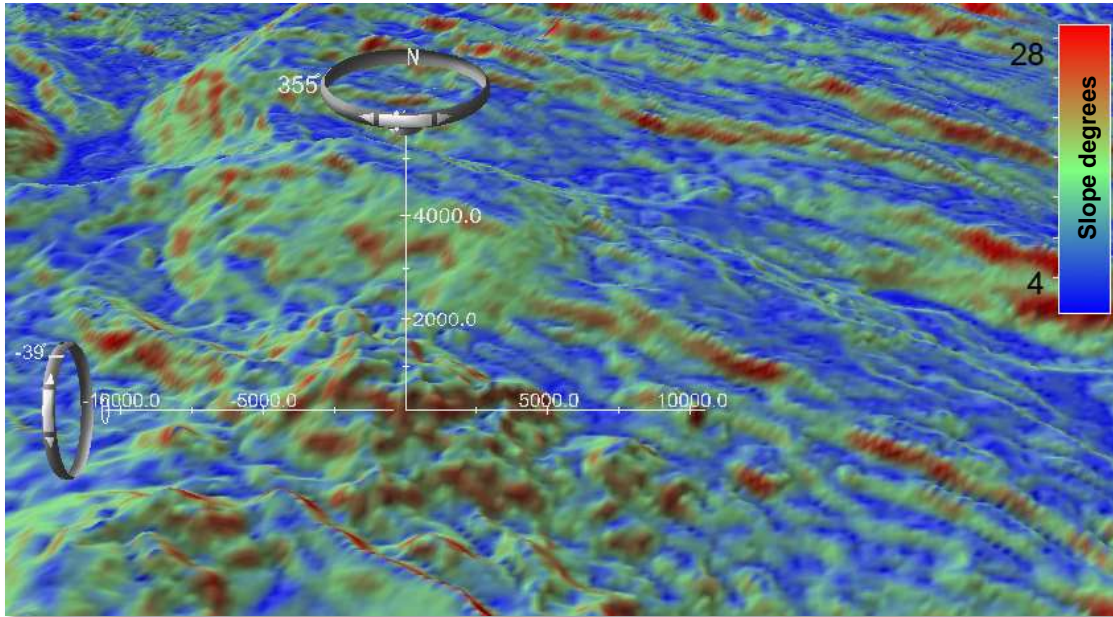


Figure 2.19. Slope map of Neck and Head Peaks.

6. Discussion

Mantle composition, ridge geometry, thermal structure, and spreading rate all influence ridge tectonics (Macdonald, 1982). At the present time, the dominant mode of spreading along mid-ocean ridges is slow, but of the existing crust, up to 50% was created at fast ridges (e.g., Teagle et al., 2012). Because asymmetric spreading is a relatively newly discovered mode of seafloor spreading, it is important to consider the influence of spreading rate on the formation of oceanic core complexes. The spreading rate at Godzilla Megamullion has been determined using magmatic zircon $^{206}\text{Pb}/^{238}\text{U}$ ages to have a half-spreading rate of ~ 25.4 mm/yr (Tani et al., 2011). Comparisons of the azimuth of rotation throughout time on the conjugate flank suggest that the spreading rate is similar on both margins providing a full spreading rate of ~ 50 mm/yr. If this

comparison is correct this suggests that the seafloor in this region formed at an intermediate rate, when compared to global seafloor spreading rates. The paucity of dates in the medial section means that a linear interpolation of the spreading rate during this time is relatively poorly constrained (Fig. 2.20).

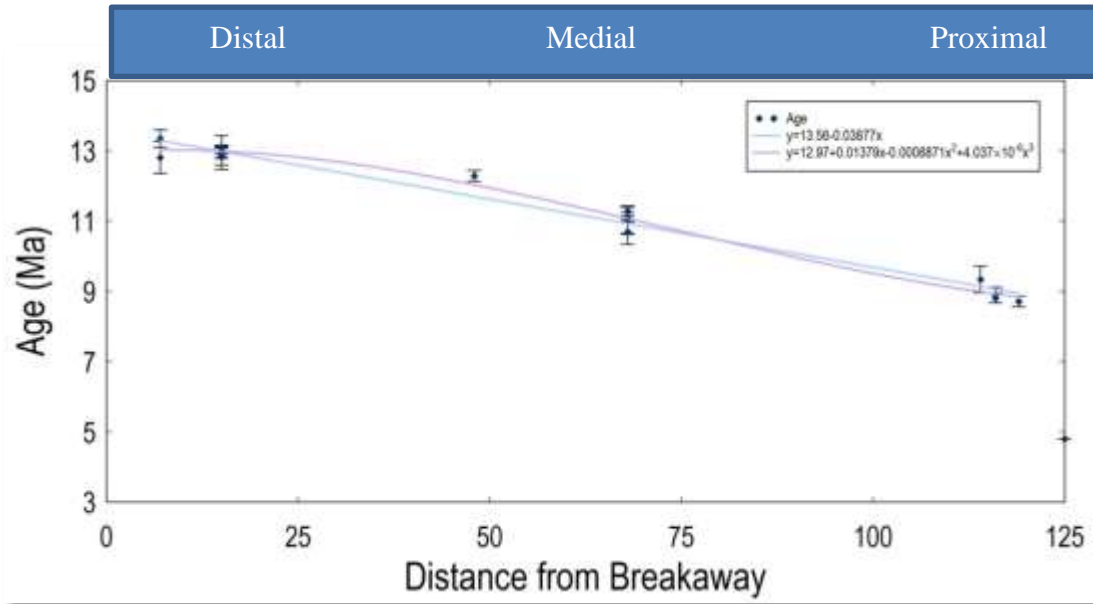


Figure 2.20. Zircon dates vs distance from paleoridge, from Tani et al., 2010.

The spread of the ages and their spatial distribution means that changes in their interpretation can vary the spreading rate significantly. The ages are from dredge hauls that result in multiple dates from single dredges. There is a possibility that older rocks are transported along the oceanic core complex surface during spreading but the youngest age from each location is arguably the most accurate. Integration of these dates with all the high-resolution multibeam data provides an opportunity to reexamine the ages. An alternative interpretation of the dates provides spreading rates of for the distal, medial and proximal regions of ~60, ~23, and ~7 mm/yr respectively, and an average spreading rate

of ~30 mm/yr. However, because the age of the termination is not known it is possible that changes of the spreading rate in the proximal regions are difficult to identify. This alternative interpretation based on the data provides a possible mechanism for the changes to the oceanic core complex in the distal, medial, and proximal sections of Godzilla Megamullion. Based on the available zircon dates, the spreading rate decreased through time may have increased during the termination (e.g., Tani et al., 2011).

Basalts from Head peak have been dated at 4.8 Ma (Ishizuka et al., 2004), an age penecontemporaneous with the late- to post-rift phase Kinan volcanism that occurred in the Shikoku Basin (Sato et al., 2002). The Kinan volcanics are a series of eastward younging seamounts that span the eastern margin of the Shikoku Basin. The seamounts are thought to have formed in response to steepening of the subducting slab or changes in mantle convection or heat flux (Ishizuka et al., 2009). It is inferred that the Kinan volcanism, previously defined only in the Shikoku Basin (Ishizuka et al., 2009), may have also occurred further south in the Parece Vela Basin. Further work is necessary to determine the ages of seamounts in this region.

6.1 Transform Angle

The strike of the bounding transforms change between the distal, medial, and proximal sections. In the distal section the transforms strike 030° , changing to 025° in the medial and proximal and steps across to an angle of 030° adjacent to the termination. These changes in direction have widened the bounding transform to the northwest and

shortened the southeast. In the later parts of the proximal section both transform margins widened.

The development of transforms requires orthogonal deformation that has been related to the spreading rate (Atwater and Macdonald, 1977), heat, and lithosphere/asthenosphere viscosity contrasts (Marques, 2012). Transform faults maintain a geometry that is orthogonal to rifts because of their very low shear strength (Escartín et al., 2001). Furthermore, numerical models show that offsets along transforms change through time and are related to asymmetric plate growth and ridge jumps (Gerya, 2010). Insights provided by both physical and numerical models of transforms and asymmetric spreading are fundamental to the study of the Godzilla Megamullion development because the results confirm that orders of segmentation correlate with ridge angle offset, spreading rate, and the mode of spreading (symmetric vs asymmetric). The changes observed in amagmatic segments are driven by the mantle (Dick et al., 2003). Local changes in spreading character can be controlled by changes in the thermal lithosphere and mantle composition (melting).

Menard and Atwater (1968, 1969) showed that that spreading direction controls interaction within ridge segments, and that fracture zones cannot adapt to changes in spreading direction. Part of their work included a model for oceanic crust formation that involves rotation of abyssal hills during their creation. An alternative, more widely accepted hypothesis for the geometry observed in bathymetry and magnetic data, for reorientation of ridge axes is the propagating rift model, first proposed in the Eastern

Pacific (Hey et al., 1988). In the Godzilla region of the Parece Vela Basin, the magnetic, or age data required to differentiate between these two models is not available.

The solutions to a lack of malleability in transform faults are adjustment fractures that develop when spreading occurs at an oblique angle. Ridges adjust to changes in the spreading direction by breaking into stair-stepping segments that facilitate the new spreading direction. From existing models (e.g., Marques, 2012) we know that transforms must form orthogonal to the spreading direction. Changes in the spreading direction through time thus change the angle of the transforms. These changes in the spreading direction necessitate the formation of adjustment fractures and transforms that accommodate some extension and the impact this may have on spreading rate is unquantified. Menard and Atwater (1969) suggest in a configuration where the edges of ridges are in compression due to overlapping crests, spreading could not proceed at the same rate as others ridges in the same region.

6.2 Melt Extraction

Godzilla Megamullion has two large corrugations that are persistent from the breakaway through, distal to the start of the medial section. Both corrugations end before the medial section in circular features that resemble craters. This suggests that the corrugations represent magmatically robust sections of the detachment surface. There is also a possibility that the volcanism may be of the serpentinite/mud variety (e.g., Fryer, 2012). However, the steep slopes on the outer walls of the central volcanic edifice suggest that the volcanism is not mud related, as serpentinite typically cannot support

slopes greater than 20° (Cannat et al., 2013). Rock samples collected from the corrugations are a mix of peridotite, gabbro, and basalt suggesting that the corrugations are parts of the crust and upper mantle. In the medial section that follows the volcanic craters, using spinel chemistry from peridotites, Loocke et al. (2013) identified a change in the eruptive style from robust magmatic spreading in the distal section to a drop in melt productivity in the medial, and observed significant melt stagnation in the proximal section. These observations agree with results from seismic investigations that have shown that changes in the spreading rate affect melt extraction processes (Lizarralde et al., 2004). At Godzilla Megamullion, decreases in melt supply causes stagnation in the lithosphere and crustal thickening (Loocke et al., 2013).

Corrugations found on oceanic core complexes represent the geometry of the detachment fault surface, or are the result of an irregular shaped brittle-ductile transition zone at depth (Tucholke et al., 2008), or are the result of extension perpendicular shortening due to crustal thinning and lateral migration of the lower crust (Singleton, 2012). The suggestion that corrugations may be fractal lends some support to a model that is based on fault linkage rather than crustal flow. However, if the corrugations are related to magmatic activity at the ridge axis, the absence of volcanic corrugations in the medial and proximal sections (Fig. 2.21) suggests that volcanic activity lessened during this time. The two volcanic craters adjacent to the medial section may therefore be the result of a last gasp of deep melt prior to melt stagnation as a result of the change in spreading rate and orientation. This last gasp of volcanism has also been identified using geochemical data by Wilson et al. (2013), who showed that the composition of erupted

material prior to oceanic core complex formation is a deeper enriched source that produces an extreme EMORB type lava coupled with enriched HREE (garnet field melting).

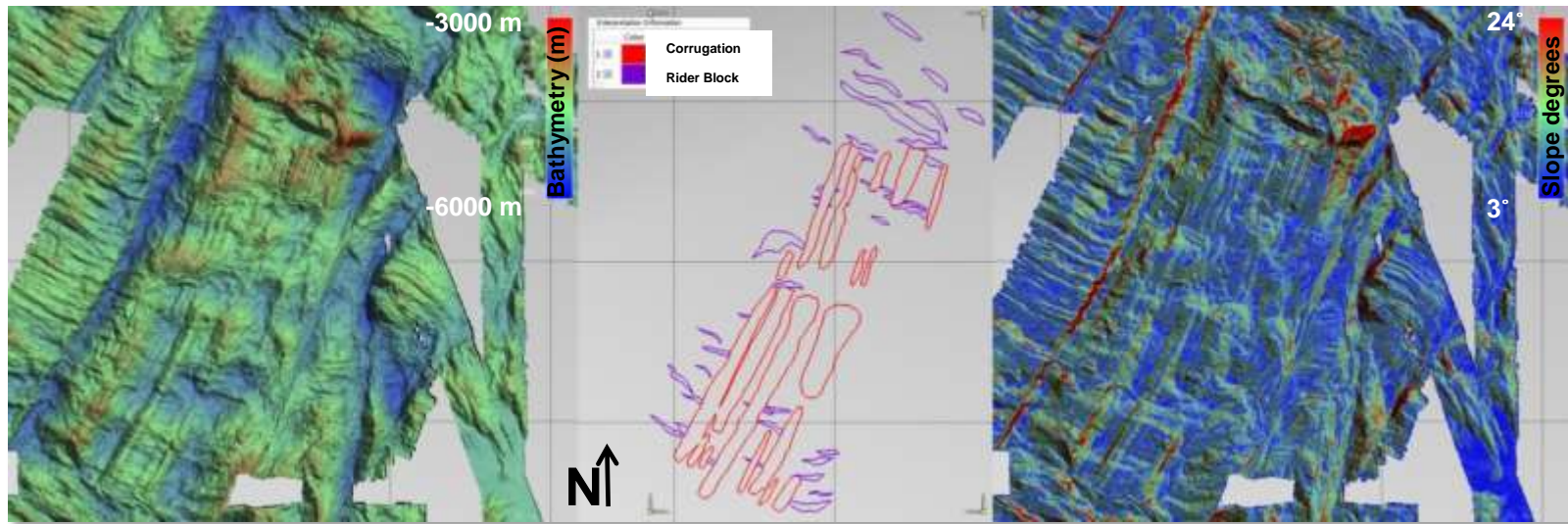


Figure 2.21. From left to right: Bathymetry, interpretation, slope map. The interpretation includes corrugations in red and fault scarps in purple. Surfaces with normal fault-like geometry tilted towards and away from the termination were recorded as sometimes back-tilted surfaces proved useful where the fault scarp was covered by subsequent rider blocks. Where there are more fault scarps there are fewer corrugations, because the fault scarps are related to rider blocks that override and hide the corrugations. For a full discussion of this process and its prevalence see Reston and Ranero (2011).

6.3 Oceanic Core Complex Initiation

The transition from magmatic (symmetric) to starved (asymmetric) spreading occurs at the breakaway. Distances measured from the breakaway to the start of the corrugations provide a proxy for crustal thickness. The relatively short distance between the breakaway and corrugations suggest that the crust at the time of the breakaway was ~5 – 10 km thick. Prior to the breakaway the faults were higher and steeper than other normal faults in the region. Before the initiation of an oceanic core complex, it is likely that the strain rate was higher due to higher spreading rates. The rift-flank faults accommodated increasing amounts of strain leading up to the development of slip, in excess of conventional fault-growth models, on a detachment fault plane.

The presence of two domal highs in the breakaway region signifies that the Godzilla megamullion initiated on two smaller oceanic core complexes that subsequently linked up along the entire segment. The development of Godzilla into a segment-filling oceanic core complex may be a result of the proximity of the transform faults to the bounding non-transform offsets. This occurs because strain is more easily partitioned along the two preexisting transform faults than four new non-transform offsets.

The en-echelon faults that cross cut the corrugations have two possible explanations: 1) the surface of the oceanic core complex was stretched during extension, or 2) slivers of crustal material (rider blocks) started to form in the proximal section. Stretch-related features would have to form after exhumation resulting in the faults cutting the corrugations. In fact, the opposite is observed; corrugations frequently cross-cut the

faults creating offset blocks, so they are interpreted as faults. Where there are more fault scarps there are fewer corrugations. In some regions the angular and blocky morphology of the seafloor is indicative of fault-bounded blocks likely to be rider blocks rafted onto the footwall surface. Thus, much of the proximal section of Godzilla is hidden beneath rider blocks, as evidenced by the presence of rotated fault scarps and the chaotic and blocky morphology of this region.

The smaller en-echelon fractures and faults seen across the surface of Godzilla Megamullion, and that are prevalent in the medial and proximal regions, may be related to reaction-driven cracking caused by shallow hydrothermal circulation driven by melt stagnation in the lithosphere (Loocke et al., 2013; Pontbriand and Sohn, 2014). In this scenario thermal contraction of the extruded seafloor generates tectonic fracturing (Sohn et al., 2004). Fractures and fissures created by the thermal contraction of the seafloor are driven by magmatic intrusion in the shallow subsurface facilitates above average heat transfer and drives hydrothermal convection. Fractures and fissures associated with reaction-driven cracking occur to depths of ~120 m, and are associated with the precipitation of the retrograde soluble mineral anhydrite. Anhydrite is a useful identifier of hydrothermal activity because it precipitates at ~150°C and dissolves at colder temperatures. Targeted drill coring of the Godzilla Megamullion surface using a remotely operated drilling system would allow further identification of anhydrite bearing fractures and allow further recognition of the formative processes.

Convex slopes exist in several places on the Godzilla's surface. For example, above where the fault plane of South Tail Rise disappears there is a large region of convex

slope. In some places the convex nature of the footwall is inferred because of the presence of numerous rider blocks that cover the detachment surface. Exhumation of dome shaped footwall fault plane is in agreement with the conventional rolling hinge model for oceanic core complex development (Buck, 1988; MacLeod et al., 2011).

Seafloor spreading ceased in the Godzilla Megamullion region at ~8 Ma; the water depth in this region is approximately 4 km. In contrast, recently formed oceanic core complexes at 14°N in the Mid-Atlantic occur in water depths of ~2500 m. Seafloor spreading at Godzilla Megamullion started at 14 Ma and terminated at ~8 Ma (Tani et al., 2011). The depth of the seafloor is proportional to the square root of age and depth data from global ocean basins indicates that rates of $324 - 348 \text{ m/Ma}^{-1/2}$ are typical (Tréhu et al., 1975). Using depth data from a multi-resolution synthesis of gravity and bathymetry (Geomapp.org; Ryan et al., 2009) and the rate of extension from Tani et al. (2011), a paleo-depth range has been constructed for the Godzilla Megamullion region (Fig. 2.22). The best fit line indicates an increase in depth equivalent to 246 m/Ma. In comparison, the \sqrt{t} equation provides a depth trend identical to the depth data, but 1000 m shallower. Furthermore, the mean depth over Godzilla Megamullion is ~4 km below sea level and the age range is between 8 - 14 Ma. A comparison between the sea level, age range, and the depth-age model of Stein and Stein (1992) indicates that there has been a ~1 km increase in water depth over the previous ~15 Ma. This also means that the seafloor in this back arc basin is presently ~1 km deeper than the standard \sqrt{t} age model predicts. The paleo water depth as constrained by the trend line fit of the bathymetric data suggests a depth increase of ~2053 m following the emplacement of the oceanic core complexes.

Alternatively, the depth curves from the \sqrt{t} age model and Stein and Stein (1992) indicate a depth increase of 1 km. Using a present day water depth of 4000 m these results place the paleo water depth at approximately 2000 – 3000 m, similar to the water depth over recently developed oceanic core complexes at 14°N on the Mid-Atlantic Ridge.

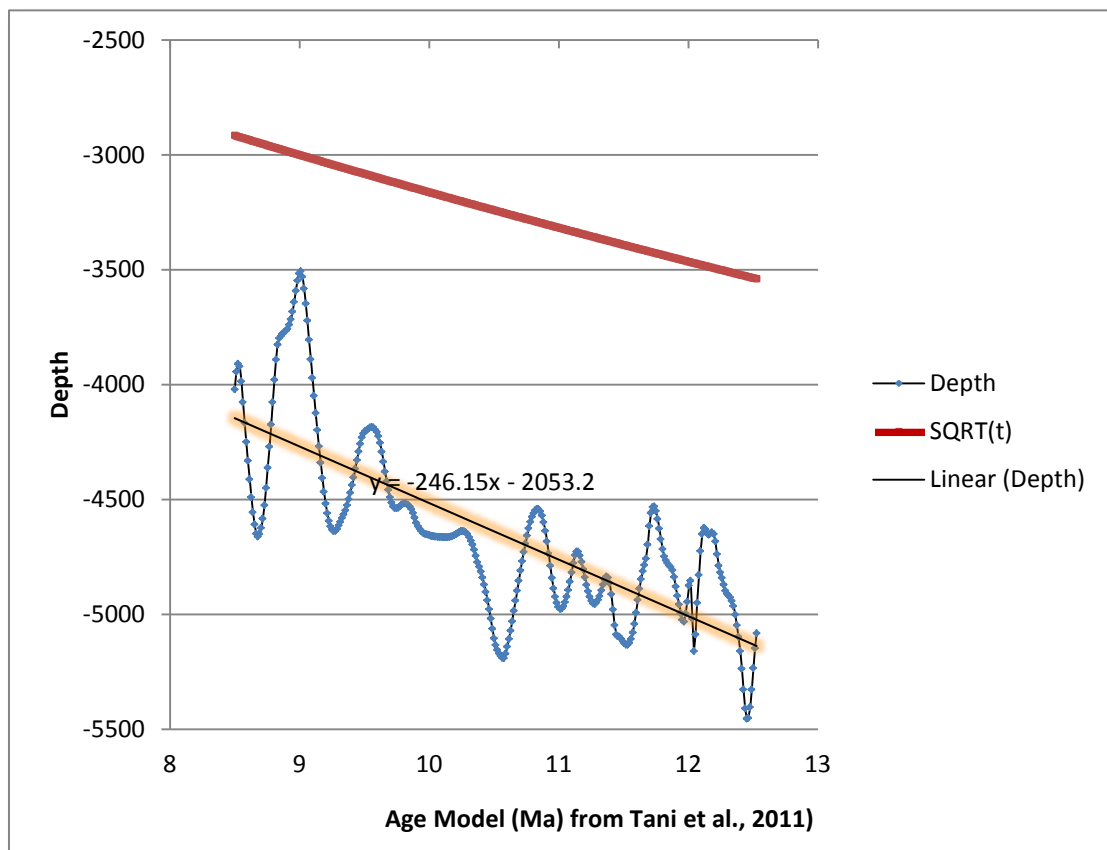


Figure 2.22. Depth – age plot for Godzilla Megamullion. The general trend is 246 m/Ma increase in depth away from the ridge axis. Also included is the general ocean depth – age relationship in red, where depth is proportional to the square root of age (SQRT(t)).

6.4 Corrugations and Ridges

A “false color bathymetry” (Spencer and Ohara, 2014) map was used to identify the corrugations and ridges. Furthermore, gridding the data at a resolution determined by the sounding density has allowed the creation of bathymetric maps at a resolution appropriate to the acquired data that is available to allow a more detailed interpretation of the seafloor. Mapping all of the corrugations, ridges, faults, and fractures in the region has allowed us to make a more detailed interpretation of the geologic structure of Godzilla Megamullion (Fig. 2.23). In total, 495 linear ridges or fault related features, and over 100 corrugations, were mapped. The undiscovered origin of the corrugations does not preclude the fact that they record the plate separation direction. Thus, the curvature of the corrugations clearly identifies changes in the orientation of the spreading direction during the development of Godzilla Megamullion. A change in the orientation of ridges can clearly be identified from east west spreading in the west at magnetic isochron 6A (~19 Ma) towards a more northeast – southwest component towards the breakaway and transitioning back to a north – south-spreading direction at the breakaway (~9 Ma).

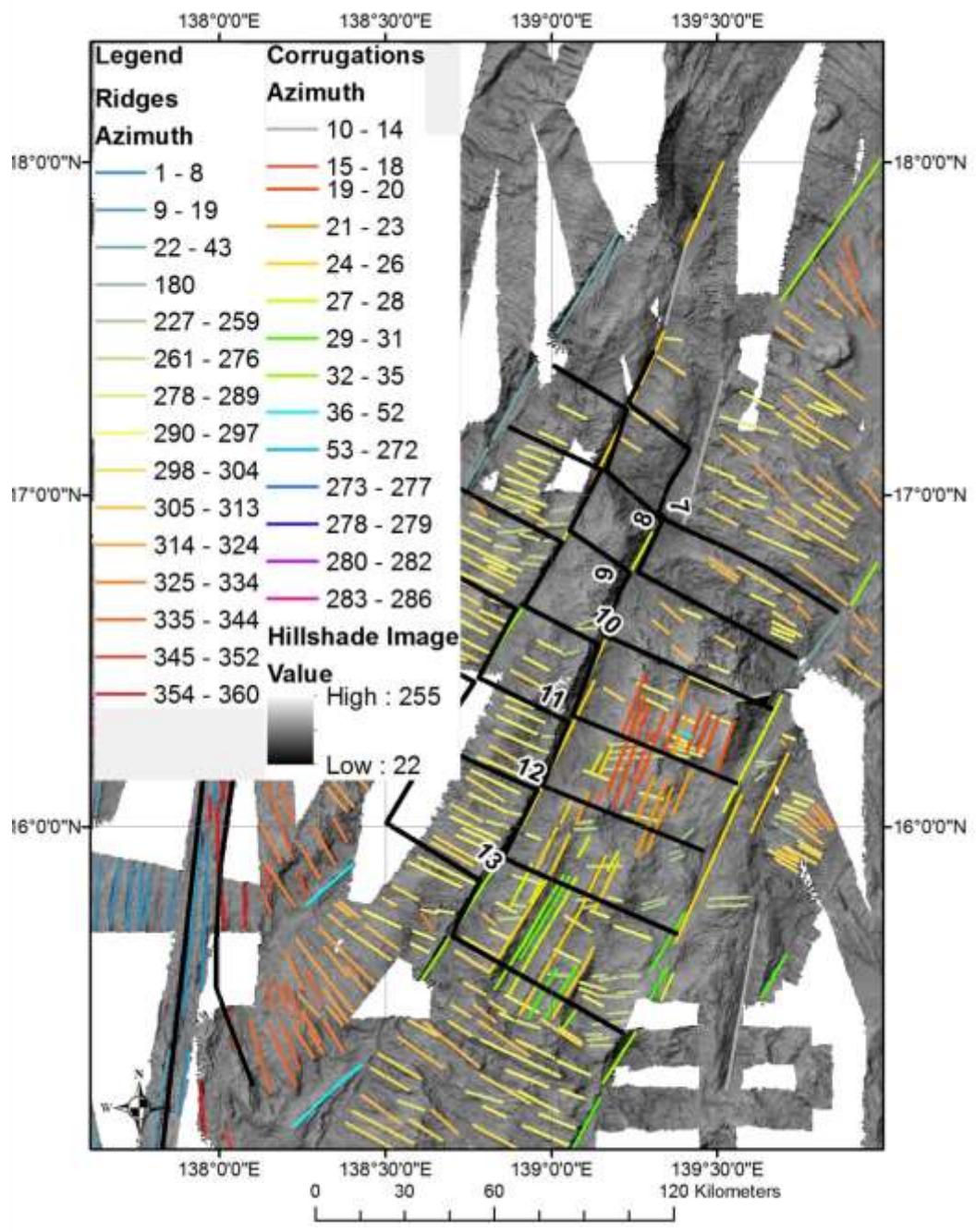


Figure 2.23. Measurements of length and azimuth of linear features interpreted to be corrugations and ridges from the Godzilla Megamullion bathymetry dataset. Dates from Tani et al., 2011 are also shown along with interpreted regions of equal age.

The azimuth of corrugations and normal to the ridge axes plotted along with the age range and azimuth of the corrugations in the different segments of the Godzilla region provides further evidence for a trend in seafloor spreading towards a more northerly direction during oceanic core complex development (Fig. 2.24). The corrugation and ridge data trend at right angles to one another showing that they developed together as a result of a singular extension direction (Fig. 2.25).

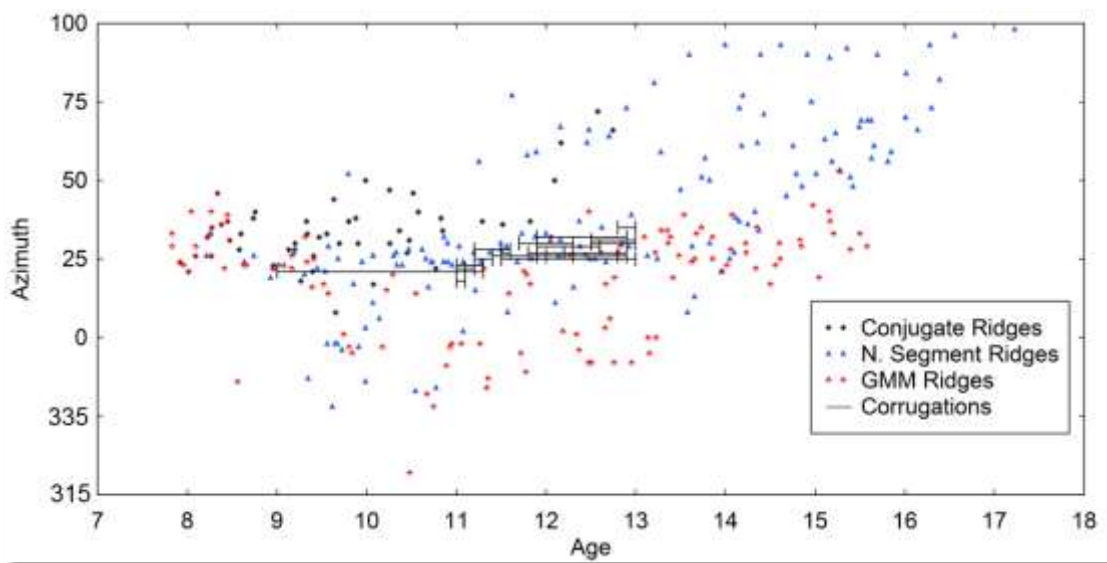


Figure 2.24. Cross plot of corrugation azimuth (degrees) with age range of corrugations and ridges (Ma).

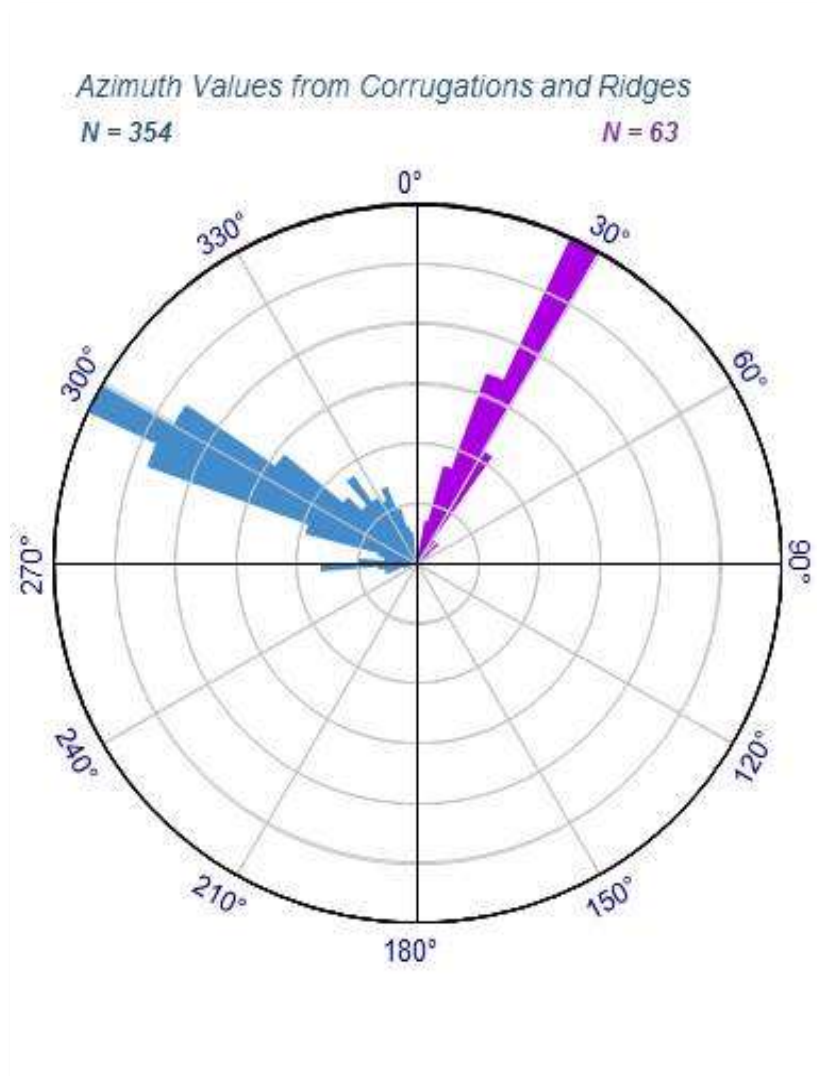


Figure 2.25. Rose plot of corrugation and ridge azimuth data. The Corrugations (purple) trend towards 30° and the ridges (blue) trend toward 300°. The corrugation and ridge data lie at right angles to one another. 354 ridge measurements and 63 corrugation measurements were used to make this figure.

7. Conclusions

The evolution of oceanic core complexes in a back-arc spreading environment provides an opportunity to observe extensional crust accretion under a somewhat different set of geodynamic boundary conditions than at most mid-ocean ridges. The integrated bathymetric dataset makes it possible to identify new features in the Parece Vela Basin and further characterize the life cycle Godzilla Megamullion. Using advanced processing techniques and software we were able to view publicly available bathymetry at the highest possible resolution, the main requirement for recognition of new, and better assessment of the existing features.

Conclusions that can be drawn from this study are:

1. The breakaway region of the Godzilla Megamullion contains two oceanic core complexes that formed during the initiation of asymmetric spreading and that subsequently linked across the entire segment.
2. Rider block are present on the oceanic core complex surface in the medial and distal section and obscure surface corrugations.
3. Changes in the spreading direction through time may have changed the state of stress in the transform faults and is likely to have been driven by changes in the mantle composition and thermal structure.
4. The presence of volcanic corrugations and en-echelon fractures and fissures created by reaction driven cracking are present on the Godzilla Megamullion surface, in agreement with recent geochemical studies (Loocke et al., 2013) that

with a decrease in spreading rate a gabbroic phase is retained in the lithosphere rather than delivered to the surface.

8. References

- Atwater, T., Macdonald, K.C., 1977. Are spreading centers perpendicular to their transform faults? *Nature* 270, 715-719.
- Blackman, D.K., Cann, J.R., Janssen, B., Smith, D.K., 1998. Origin of extensional core complexes: Evidence from the Mid-Atlantic Ridge at Atlantis fracture zone. *Journal of Geophysical Research: Solid Earth* 103, 21315-21333.
- Buck, W.R., 1988. Flexural rotation of normal faults. *Tectonics* 7, 959-973.
- Cannat, M., Casey, J.F., 1995. An ultramafic lift at the Mid-Atlantic Ridge: successive stages of magmatism in serpentinized peridotites from the 15°N region, in: Vissers, R.L.M., and Nicolas, A. (Ed.), *Mantle and lower crust exposed in oceanic ridges and in ophiolites : contributions to a specialized symposium of the VII EUG Meeting*, . Kluwer, Strasbourg, pp. 5-34.
- Cannat, M., Mangeney, A., Ondréas, H., Fouquet, Y., Normand, A., 2013. High resolution bathymetry reveals contrasting landslide activity shaping the walls of the Mid-Atlantic Ridge axial valley. *Geochemistry, Geophysics, Geosystems* 14(4), 996-1011.
- Caress, D., Chayes, D., 1995. New software for processing sidescan data from sidescan-capable multibeam sonars, OCEANS'95. MTS/IEEE. *Challenges of Our Changing Global Environment. Conference Proceedings. IEEE*, pp. 997-1000.
- Choi, E., Buck, W.R., 2012. Constraints on the strength of faults from the geometry of rider blocks in continental and oceanic core complexes. *Journal of Geophysical Research: Solid Earth* 117, B04410.
- Dawers, N.H., Anders, M.H., 1995. Displacement-length scaling and fault linkage. *Journal of Structural Geology* 17, 607-614.
- Dick, H.J.B., Lin, J., Schouten, H., 2003. An ultraslow-spreading class of ocean ridge. *Nature* 426, 405-412.
- Escartín, J., Hirth, G., Evans, B., 1997. Effects of serpentinization on the lithospheric strength and the style of normal faulting at slow-spreading ridges. *Earth and Planetary Science Letters* 151, 181-189.
- Escartín, J., Hirth, G., Evans, B., 2001. Strength of slightly serpentinized peridotites: Implications for the tectonics of oceanic lithosphere. *Geology* 29, 1023-1026.
- Fryer, P., 2012. Serpentine mud volcanism: observations, processes, and implications. *Annual Review of Marine Science* 4, 345-373.
- Gerya, T., 2010. Dynamical instability produces transform faults at mid-ocean ridges. *Science* 329, 1047-1050.

Grimes, C.B., John, B.E., Cheadle, M.J., Wooden, J.L., 2008. Protracted construction of gabbroic crust at a slow spreading ridge: Constraints from 206Pb/238U zircon ages from Atlantis Massif and IODP Hole U1309D (30°N, MAR). *Geochemistry, Geophysics, Geosystems* 9, Q08012.

Harigane, Y., Michibayashi, K., Ohara, Y., 2011. Relicts of deformed lithospheric mantle within serpentinites and weathered peridotites from the Godzilla Megamullion, Parece Vela Back-arc Basin, Philippine Sea. *Island Arc* 20, 174-187.

Hey, R.N., Menard, H.W., Atwater, T.M., Caress, D.W., 1988. Changes in direction of seafloor spreading revisited. *Journal of Geophysical Research: Solid Earth* 93, 2803-2811.

Ishizuka, O., Ohara, Y., Sato, H., Okino, K., 2004. "Rejuvenated" volcanism in the Parece Vela backarc basin: its timing and chemical characteristics, AOGS Abstract, 57-OSE-A1500, 2004.

Ishizuka, O., Yuasa, M., Taylor, R.N., Sakamoto, I., 2009. Two contrasting magmatic types coexist after the cessation of back-arc spreading. *Chemical Geology* 266, 274-296.

Karig, D.E., 1971. Structural history of the Mariana island arc system. *Geological Society of America Bulletin* 82, 323-344.

Lizarralde, D., Gaherty, J.B., Collins, J.A., Hirth, G., Kim, S.D., 2004. Spreading-rate dependence of melt extraction at mid-ocean ridges from mantle seismic refraction data. *Nature* 432, 744-747.

Loocke, M., Snow, J.E., Ohara, Y., 2013. Melt stagnation in peridotites from the Godzilla Megamullion Oceanic Core Complex, Parece Vela Basin, Philippine Sea. *Lithos* 182, 1-10.

Macdonald, K.C., 1982. Mid-ocean ridges: Fine scale tectonic, volcanic and hydrothermal processes within the plate boundary zone. *Annual Review of Earth and Planetary Sciences* 10, 155.

MacLeod, C.J., Searle, R.C., Murton, B.J., Casey, J.F., Mallows, C., Unsworth, S.C., Achenbach, K.L., Harris, M., 2009. Life cycle of oceanic core complexes. *Earth and Planetary Science Letters* 287, 333-344.

MacLeod, C.J., Carlut, J., Escartín, J., Horen, H., Morris, A., 2011. Quantitative constraint on footwall rotations at the 15 degrees 45 ' N oceanic core complex, Mid-Atlantic Ridge: Implications for oceanic detachment fault processes. *Geochemistry, Geophysics, Geosystems* 12, Q0AG03.

Mallows, C., 2011. Geophysical Studies of Oceanic Core Complexes: The Mid-Atlantic Ridge, 13-14°N. Unpublished doctoral dissertation, Durham University, UK.

Mallows, C., Searle, R.C., 2012. A geophysical study of oceanic core complexes and surrounding terrain, Mid-Atlantic Ridge 13°N - 14°N. *Geochemistry, Geophysics, Geosystems* 13, Q0AG08.

Marques, F., 2012. Transform faults orthogonal to rifts: Insights from fully gravitational physical experiments. *Tectonophysics* 526, 42-47.

McCaig, A.M., Cliff, R.A., Escartín, J., Fallick, A.E., MacLeod, C.J., 2007. Oceanic detachment faults focus very large volumes of black smoker fluids. *Geology* 35, 935-938.

McCaig, A.M., Delacour, A., Fallick, A.E., Castelain, T., Fruh-Green, G., 2010. Detachment fault control on hydrothermal circulation systems: Interpreting the subsurface beneath the TAG hydrothermal field using the isotopic and geological evolution of oceanic core complexes in the Atlantic. *Diversity of Hydrothermal Systems on Slow Spreading Ocean Ridges, Geophysical Monograph Series* 188, 207-240.

Menard, H.W., Atwater, T., 1968. Changes in direction of sea floor spreading. *Nature* 219, 463-467.

Menard, H.W., Atwater, T., 1969. Origin of fracture zone topography. *Nature* 222, 1037-1040.

Ohara, Y., Yoshida, T., Kato, Y., Kasuga, S., 2001. Giant megamullion in the Parece Vela backarc basin. *Marine Geophysical Researches* 22, 47-61.

Ohara, Y., Snow, J., 2009. Godzilla Mullion: Current understanding on the nature of the world's largest oceanic core complex, AGU Fall Meeting Abstracts, p. 06.

Ohara, Y., Okino, K., Snow, J.E., 2011. Tectonics of magma-starved crust formation in the Parece Vela Basin. *Modern Approaches in Solid Earth Sciences* 8, 149-168.

Pontbriand, C.W., Sohn, R.A., 2014. Microearthquake evidence for reaction-driven cracking within the Trans-Atlantic Geotraverse active hydrothermal deposit. *Journal of Geophysical Research: Solid Earth* 119, 822-839.

Reston, T.J., Ranero, C.R., 2011. The 3-D geometry of detachment faulting at mid-ocean ridges. *Geochemistry, Geophysics, Geosystems* 12, Q0AG05.

Ryan, W.B., Carbotte, S.M., Coplan, J.O., O'Hara, S., Melkonian, A., Arko, R., Weissel, R.A., Ferrini, V., Goodwillie, A., Nitsche, F., 2009. Global Multi - Resolution Topography synthesis. *Geochemistry, Geophysics, Geosystems* 10, Q03014.

Sato, H., Machida, S., Kanayama, S., Taniguchi, H., Ishii, T., 2002. Geochemical and isotopic characteristics of the Kinan Seamount Chain in the Shikoku Basin. *Geochemical Journal Japan* 36, 519-526.

Sauter, D., Cannat, M., Rouméjon, S., Andreani, M., Birot, D., Bronner, A., Brunelli, D., Carlut, J., Delacour, A., Guyader, V., 2013. Continuous exhumation of mantle-derived rocks at the Southwest Indian Ridge for 11 million years. *Nature Geoscience* 6, 314-320.

Searle, R.C., MacLeod, C.J., Murton, B.J., Casey, J.F., Mallows, C., Unsworth, S., Achenbach, K., Wallis, D., Pheasant, I., Baxter, D., Baxter, M., and, 2007. Geological and Geophysical Studies of the Mid-Atlantic Ridge, 12°30'N to 14°30'N, Maiden Scientific Voyage RRS James Cook Cruise JC007. Durham University, Department of Earth Sciences.

Smith, D., 2013. Tectonics: Mantle spread across the sea floor. *Nature Geosci* 6, 247-248.

Sohn, R. A., Barclay, A.H., Webb, S.C., 2004. Microearthquake patterns following the 1998 eruption of Axial Volcano, Juan de Fuca Ridge: Mechanical relaxation and thermal strain. *J. Geophys. Res.* 109, B01101, doi:10.1029/2003JB002499.

Spencer, J.E., Ohara, Y., 2014. Curved grooves at the Godzilla Megamullion in the Philippine Sea and their tectonic significance. *Tectonics*, *in press*.

Stein, C.A., Stein, S., 1992. A model for the global variation in oceanic depth and heat flow with lithospheric age. *Nature* 359, 123-129.

Tani, K., Dunkley, D.J., Ohara, Y., 2011. Termination of backarc spreading: Zircon dating of a giant oceanic core complex. *Geology* 39, 47-50.

Teagle, D.A., Ildefonse, B., Blum, P., 2012. IODP Expedition 335: Deep Sampling in ODP Hole 1256D. *Scientific drilling*, 28-34.

Tréhu, A.M., 1975. Depth versus (age)^{1/2}: A perspective on mid-ocean rises. *Earth and Planetary Science Letters* 27, 287-304.

Tucholke, B.E., Lin, J., 1994. A geological model for the structure of ridge segments in slow spreading ocean crust. *J. Geophys. Res.* 99, 11937-11958.

Tucholke, B.E., 1998. Discovery of "Megamullions" reveals gateways into the ocean crust and upper mantle. *Oceanus* 41, 15-19.

Tucholke, B.E., Behn, M.D., Buck, W.R., Lin, J., 2008. Role of melt supply in oceanic detachment faulting and formation of megamullions. *Geology* 36, 455-458.

Walsh, J.J., Nicol, A., Childs, C., 2002. An alternative model for the growth of faults. *Journal of Structural Geology* 24, 1669-1675.

Wilson, S., Murton, B., Taylor, R., 2013. Mantle composition controls the development of an Oceanic Core Complex. *Geochemistry, Geophysics, Geosystems* 14(4), 979-995.

Yeo, I., Searle, R.C., Achenbach, K.L., Le Bas, T.P., Murton, B.J., 2012. Eruptive hummocks: Building blocks of the upper ocean crust. *Geology* 40, 91-94.

***Quantitative Morphology of the Chaotic Terrain Region from
Multiple Bathymetric Surveys, Parece Vela Basin, Philippine Sea***

Abstract

The Chaotic Terrain region of the Parece Vela Basin is a large region of hummocky bathymetry. Using multibeam data gridded at high resolution from cruises to the region, this study documents the seafloor features and the spatial relationships that exist. Five distinct morphologic types of seafloor features have been interpreted: 1) breakaway faults, 2) corrugations, 3) rafted blocks, 4) normal rift flank faults, and 5) volcanoes. Based on this interpretation, the Chaotic Terrain in this survey region is shown to host several areas of asymmetric spread crust caused by the formation of oceanic core complexes during seafloor spreading. The data from different fault populations are interpreted as: breakaway faults, normal rift-flank faults, and rider blocks. Normal faults are observed to cut corrugated surfaces and also terminate the oceanic core complexes. The presence of multiple domal highs with a single breakaway fits a model of oceanic core complex development by consecutive faults. Observed changes in the orientations of corrugations shows that local changes in the spreading direction differed from the generalized tectonic regime at the time of spreading.

1. Introduction

The Chaotic Terrain is a large region of asymmetric spread crust located between 136.5 – 138°E in the western Parece Vela Basin (Okino et al., 1999; Ohara et al., 2001) (Fig. 3.1). The bathymetry is characterized by ~6000 m deep basins and ~4000 m shoals on the surfaces of oceanic core complexes. The deep basins are flat bottomed, suggesting they are old features that have been filled with sediment. In some regions it appears that several oceanic core complexes initiated along one breakaway fault. Linear fault scarps that connect and occur between the oceanic core complexes have been rotated. Corrugations are extremely well developed and, in some cases, can be traced over multiple domal surfaces. Oceanic core complexes in the Chaotic Terrain have corrugated domes and fault scarps similar to those identified in other ocean basins. The importance of low-angle normal faults in mid-ocean ridge tectonics was first recognized by Dick (1981), and is now accepted to be a dominant mode of spreading in ocean basins (Escartín et al., 2008). The presence of long linear fault scarps on the initiating edge of corrugated domal surfaces suggests a breakaway mechanism similar to Mid Atlantic oceanic core complexes (Smith et al., 2006; MacLeod et al., 2009). Seismic results from this area show increases in the p-wave velocities up to 4 - 6 km/s (Ohara et al., 2007) in the shallow crustal section of oceanic core complex footwalls, comparable with velocities of serpentized peridotite and gabbro. Ohara et al. (2007) also observed three main episodes of oceanic core complex initiation in the Chaotic Terrain. Much remains unknown about this area so this paper seeks to document the morphology of oceanic core complexes in detail and describe possible mechanism for the formation of the seafloor

features. Oceanic core complexes have been found in every ocean basin (Blackman, 2009). The Chaotic Terrain is unique because the region consists of entirely asymmetric spread crust surrounded by symmetric spread crust. This paper describes the morphology of the Chaotic Terrain region of the Parece Vela Basin where numerous oceanic core complexes have been identified.

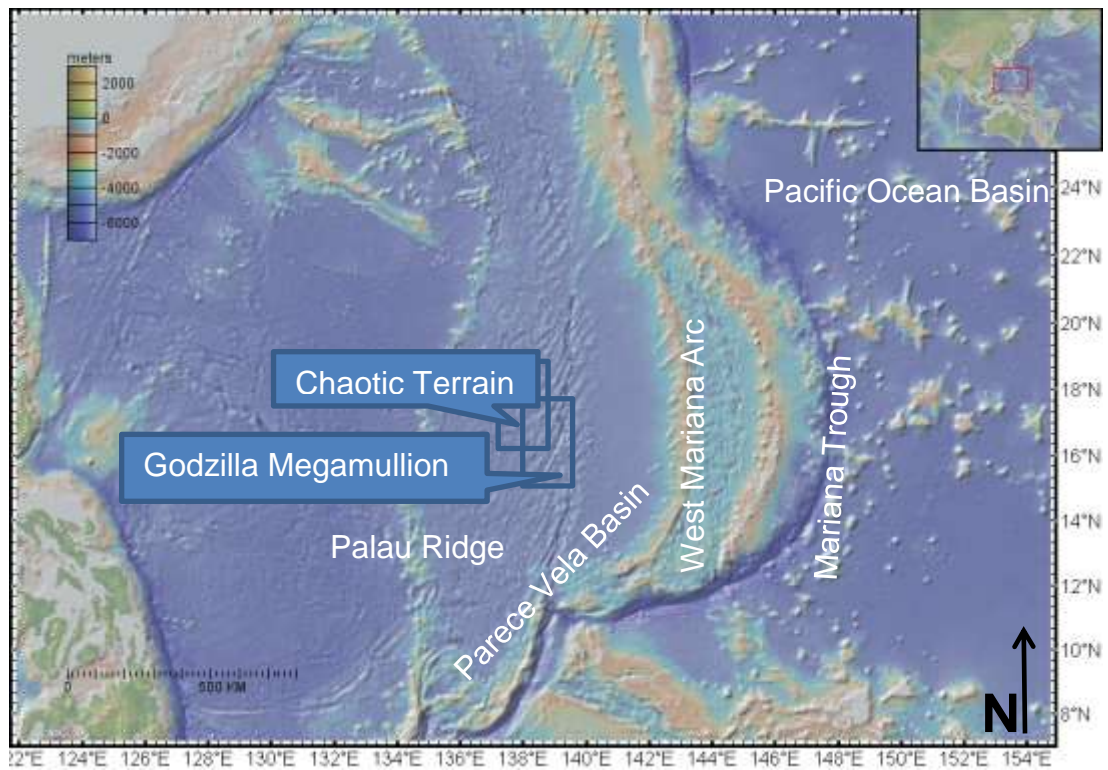


Figure 3.1. Location map for the Chaotic Terrain and Godzilla Megamullion in the Parece Vela Basin, Philippine Sea.

2. Geologic Setting

The Parece Vela Basin separates the Kyushu-Palau ridge from the West Mariana ridge. The extinct back-arc basin is a remnant of the proto-Izu-Bonin-Mariana arc. Two stages of basin formation have been identified: 1) east – west spreading from 26 – 19 Ma with a half rate 44 mm/yr, and 2) northeast – southwest spreading from 18 – 12 Ma at a rate of 25 – 35 mm/yr (Okino et al., 1999; Ohara et al., 2001; Tani et al., 2011). Sanfilippo et al. (2013) argue that because the half-spreading rate of 25 mm/yr was obtained in asymmetric spread crust where all of the extension is accommodated by one plate, the ridge appears to have been a slow spreading, rather than an intermediate spreading ridge.

3. Background

Oceanic core complexes were first discovered on the inside corners of ridge-transform intersections (Cann et al., 1997; Blackman et al., 1998). They are now known to be widespread and the mechanisms for their formation are complex. Large regions of the seafloor spread by asymmetric accretion (Ohara et al., 2001; Okino, 2004; Escartín et al., 2008). The amount of extension accommodated by oceanic core complexes can be from 10's to 100's km and can accommodate up to 100% of the spreading rate (Grimes et al., 2008). Using 2D numerical models (Tucholke and Lin, 1994; Tucholke et al., 2008) and field-based observations (MacLeod et al., 2009; Mallows and Searle, 2012) it has been shown that melt supply controls the first-order structural evolution of oceanic core complexes and that mantle chemistry is an important underlying factor in their

development (Loocke et al., 2013; Wilson et al., 2013). Further results from 3D models Pütke and Gerya (2014) argue that for a dominant control of temperature on melt supply driven by spreading rate that drives the transition from asymmetric to symmetric spreading.

Identifying regions of the seafloor that spread asymmetrically by detachment faulting can be achieved by distinguishing regions of chaotic or hummocky bathymetry from the linear ridge flank faults commonly observed in symmetric spread crust. Using only bathymetric data, there are three basic morphological building blocks of asymmetric spread crust that can be mapped and are related to the processes by which they form. These three features are: faults, corrugations, and volcanoes. Under the faults category there are several sub-categories (rider blocks, normal rift-flank faults, and breakaways) that are discussed in more detail later. The location of seafloor features, their different scales, and geometric relationships provide useful information that can be used to interpret the processes that formed them.

4. Location and Geology

The Parece Vela Basin is a back-arc basin situated in the southeastern Philippine Sea. Development of the basin occurred in three main stages: 1) trench formation, 2) arc volcanism, 3) rifting, and 4) back arc spreading (Karig, 1971). Based on marine magnetic and bathymetry data, the basin has been divided into western and central domains (Ohara et al., 2011). The western part of the basin was actively spreading up to 21 Ma at a rate of ~ 80 mm/yr with an east-west extension direction. Most of the

western basin is characterized by symmetrically spread basaltic crust. The central basin is defined by magnetic data to the east of 138°E. The extension direction changes to a northeast-southwest direction and stair-step ridges developed to accommodate the change in spreading direction. The extinct axis of the spreading ridge has been divided into 7 first-order segments offset by en-echelon fracture zones (Ohara et al., 2001; Ohara et al., 2011). The three most southerly segments (S3, S2, and S1) host oceanic core complexes (Ohara et al., 2001). The Chaotic Terrain is a region of hummocky seafloor about 100 km² to the northwest of Godzilla Megamullion (Fig. 3.2)

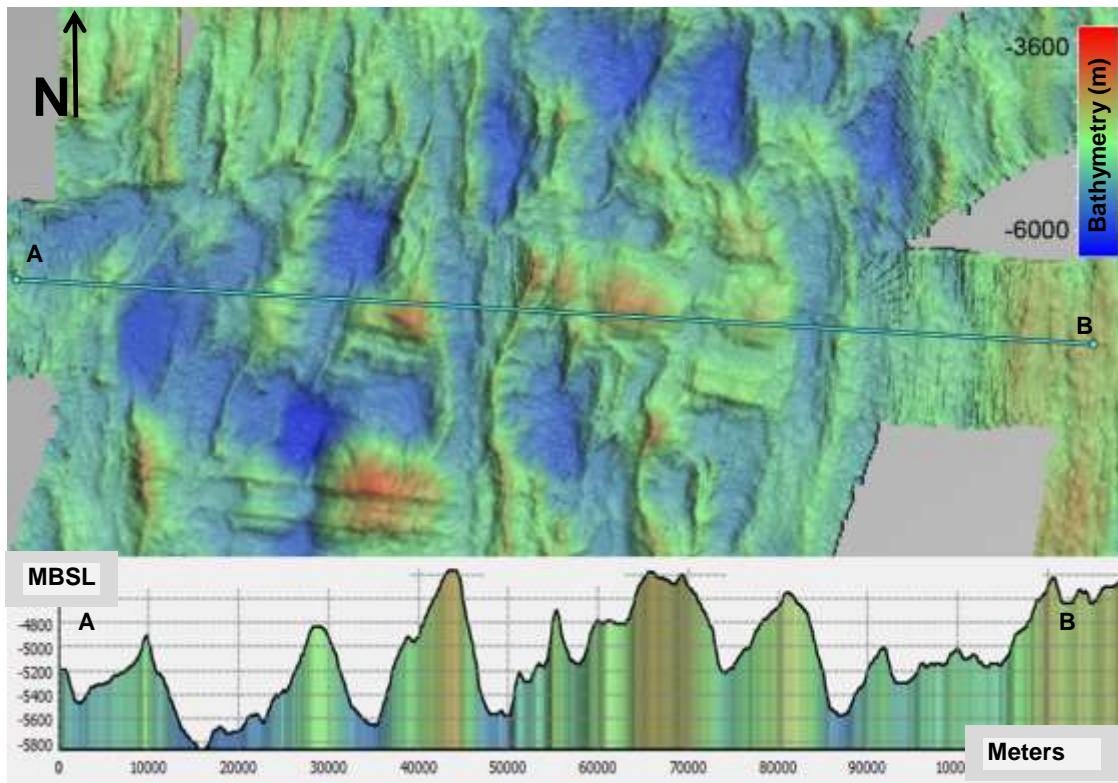


Figure 3.2. Bathymetry of the Chaotic Terrain region.

5. Methods

Data were downloaded from the Data Research System for Whole Cruise Information (DARWIN) database available through the Japan Agency for Marine-Earth Science and Technology (JAMSTEC). Data used in this study was acquired as part of the following research cruises: KR98-01, KR98-12, KR02-14, KR03-01, KR03-04 Leg 2, KR04-14 Leg 2, KR05-14, KR05-16, KR06-11, KR06-13, KR06-14, KR08-05 Leg 1, KR08-15, KY01-11 Leg 2, MR00-K04, MR00-K07 Leg 34, MR01-K05 Leg 12, MR01-K05 Leg 34, MR02-K04, MR02-K06, MR04-01, MR04-03 Leg 1, MR05-03 Leg 3, MR09-01 Leg 3, MR06-05 Leg 3, MR07-03, MR10-02, MR10-03 Leg 1, MR10-03 Leg 2, MR11-06, MR11-08 Leg 2, MR98-K02, MR99-K03, YK00-01, YK02-07 Leg 2, YK03-09 Leg 2, YK05-09 Leg 1, YK10-14, YK09-08, YK09-05, YK06-11, YK11-08, YK12-11. This dataset provides almost complete coverage of the Chaotic Terrain. Further cruises may be integrated into the database at a future date to complete the more regional coverage. The data were loaded into the QPS-SAAB modules for processing and analysis. Where necessary file formats were converted and processing steps conducted in MBsystems (Caress and Chayes, 1995). Using the Dmagic module a giant Pure File Magic area based editing database was created. From this database surfaces were exported that maintained an editable relationship between the soundings and the surface bins. The created bathymetric surface was gridded at 250 m. Data were then loaded into the Fledermaus module for visualization and analysis in 3D. Bathymetric maps were integrated with slope maps to interpret geologic features. The slope map is created by computing the slope for each cell center based on the relationship to cell neighbors

(north, east, south, and west) and then calculating as an arctan function slope in degrees from horizontal. Using this method a 90° slope is vertical.

In the following 3D figures a widget is used to identify azimuthal direction of the view and as a scale for distances. The widget has a vertical component that provides the view angle in degrees from horizontal. The horizontal component provides the view direction as a bearing. Vertical and horizontal scale bars provide 3D dimensions for the image. Where not labelled by a widget north is always up. When using the profile tool a green dot on the profile line in the 3D image corresponds to the vertical black line in the profile image. The color ramps for both 3D images and profiles are the same.

6. Bathymetry of the Chaotic Terrain

The Chaotic Terrain hosts several Oceanic Core Complexes that are clearly identified in the slope map (Figs. 3.3, 3.4 & 3.5) by the corrugations that run parallel with the spreading direction along their domal surfaces. There are several features that contribute to the morphology of the seafloor in this region that have been mapped in detail using a slope map. The features are: 1) breakaway faults, 2) corrugations, 3) rafted blocks, 4) normal rift-flank faults, and 5) volcanoes (Figs. 3.4 & 3.5). The breakaway faults are identified by their elevation; steep back-tilted surfaces, and shallow fault-dip surfaces that are occasionally corrugated.

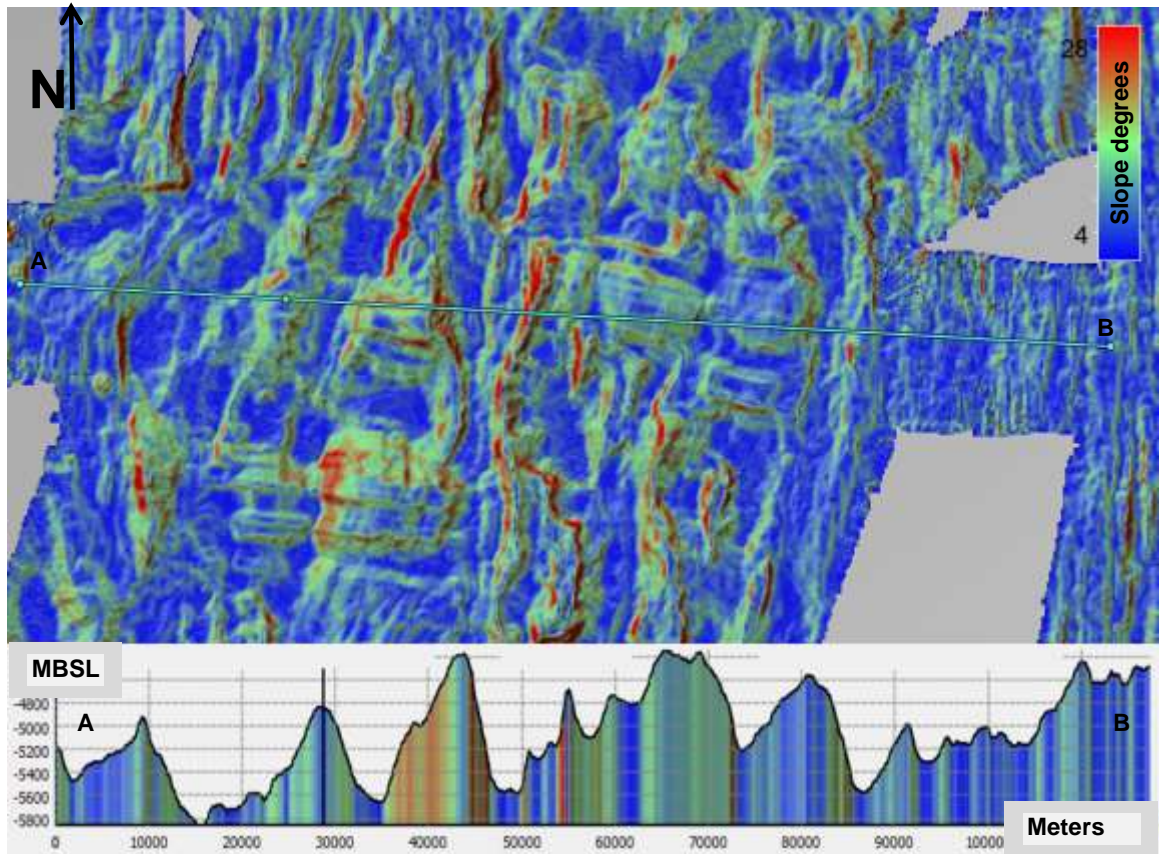


Figure 3.3. Slope map of the Chaotic Terrain region.

The breakaway faults occur adjacent to regions of seafloor, in the direction of spreading, that are corrugated. Because the surface expression of the breakaway faults includes several arc-shaped segments that suggest multiple faults have linked along strike to create a single breakaway fault. The corrugations have a wavelength of 1 – 3 km and are laterally extensive, extending over distances up to 30 km. In the region mapped (~10,000 km²) the corrugated surfaces cover 2200 km² or about 22% of the seafloor. The direction of the corrugations, and therefore spreading, changed from the western oceanic core complexes where the corrugations are aligned to ~100°, to the east where

corrugations occur on a bearing of 115° . Rafted blocks can be recognized by their occurrence on the surfaces of corrugations and by their rotation of the fault blocks. Whereas normal rift-flank faults in places cut the corrugated surfaces are orthogonal to the spreading direction and typically have elongate fault tips. Volcanoes cover 79 km^2 of the region ($\sim 1\%$) and rise $100 - 300 \text{ m}$ above the seafloor. The volcanoes occur in parts of the crust interpreted to have normal rift flank faults and are not seen in parts of the seafloor where corrugations or rafted blocks occur.

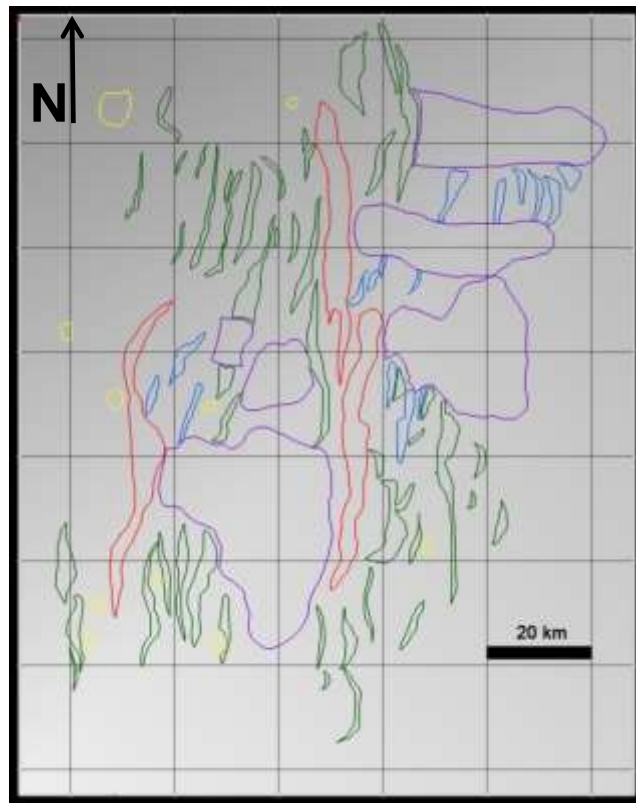


Figure 3.4. Interpretation of bathymetric features in the Chaotic Terrain. Purple: corrugated surfaces. Red: breakaway faults. Green: normal rift-flank faults. Blue: Rider blocks. Yellow: volcanoes.

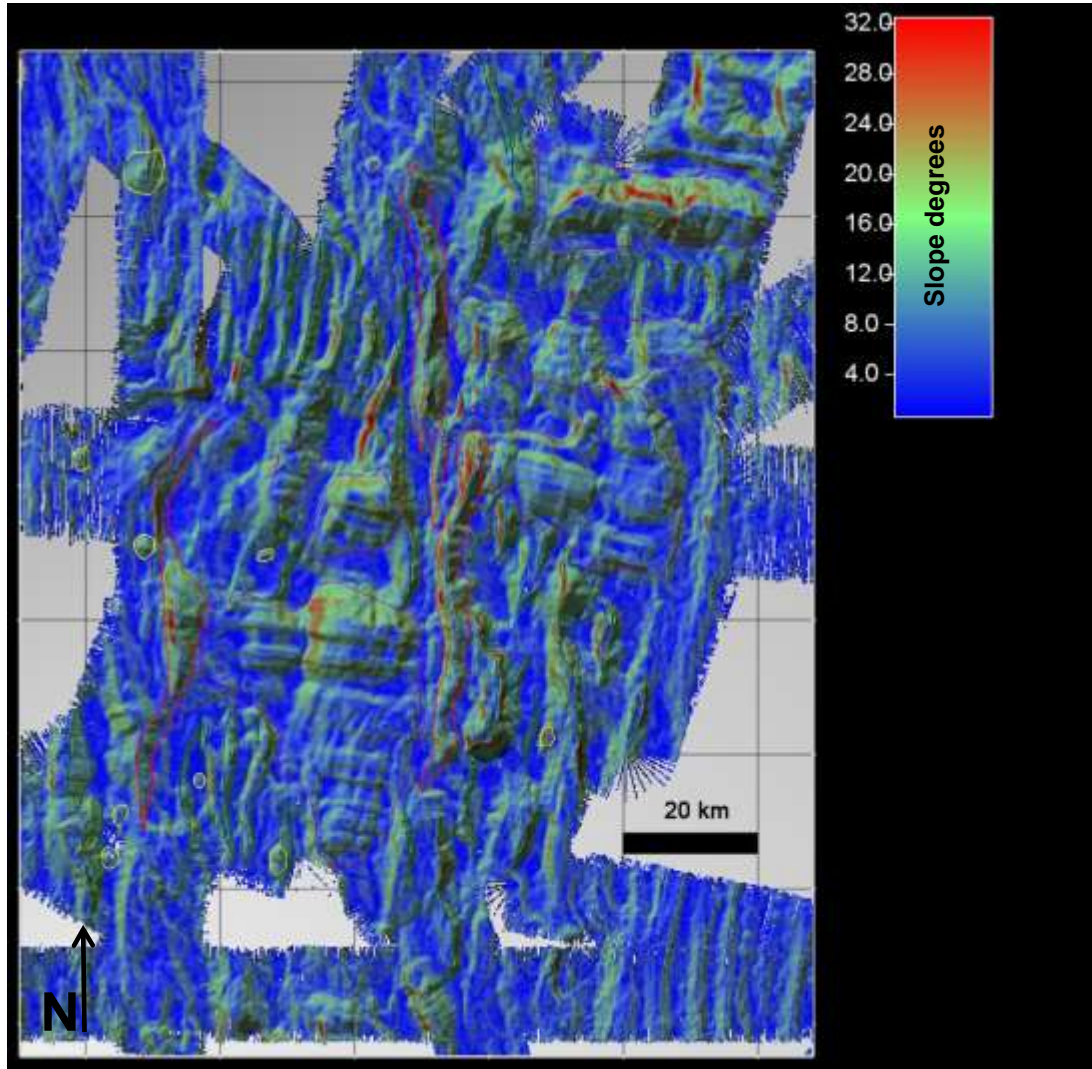


Figure 3.5. Combined interpretation and slope map of seafloor features in the Chaotic Terrain.

7. Discussion

In contrast to the Mid-Atlantic where the breakaway of oceanic core complexes are easily identified (Smith et al., 2006; MacLeod et al., 2009), in this region the breakaways are far less pronounced and in some cases difficult to identify. Rotated linear ridges linking oceanic core complexes and deep nodal basins behind the exposed dome-shaped footwall exist in both locations. That is where the similarities end; the dome-shaped surfaces in the Parece Vela Basin are larger and feature steeper slopes and longer wavelength corrugations compared to those from 13°N on the Mid-Atlantic Ridge. The variation in dome size and morphology is possibly differences in the spreading rates of the two regions, and related to fault strength at different water depths. Mohr-Coulomb theory predicts that fault rotation is more limited at greater depths that should result in steeper fault angles (Choi and Buck, 2012) that would lead to greater deformation in the footwall and could potentially result in larger domes.

The detachment faults identified in this region are interpreted to be formed by linkage of several large offset rift-flank faults with rotated fault tips. Detachment faults initiate in a steeply dipping pre-existing normal fault, termed a breakaway. Subsequently, runaway slip along a rift-flank normal fault results in creation of a detachment fault, exposure of the footwall surface and fault-block rotation (MacLeod et al., 2009). Drill cores collected from core complexes suggest a combination of high-displacement rolling hinge normal faults and secondary low-displacement high-angle normal faults exist (Schroeder et al., 2007). Paleomagnetic evidence (Garcés and Gee, 2007) and microseismic evidence (e.g.,

TAG; Trans-Atlantic Geotraverse) indicate 60-90° rotations of the footwall as oceanic core complexes are exhumed (MacLeod et al., 2011). Because the breakway massifs may be composed of peridotite that cannot support slopes greater than 20° (Cannat et al., 2013) the rotation of breakaway faults and subsequent mass-wasting processes may explain the relatively high angles (~30°) observed on the back-tilted breakway surfaces in the Chaotic Terrain.

By combining the bathymetric maps with slope maps it has been possible to extract some information about the faults. Two types of linkage are possible, along-strike linkage where fault tips link up and stacked linkage where successive faults link into a detachment (e.g., Bose and Mitra, 2009). Furthermore, changes in the fault geometry (e.g., tip propagation) and linkages can also result in variations in the cumulative slip and fault length (Nicol et al., 2005). Thus, the slip distribution and cumulative displacement of a fault can be used to understand fault development (Walsh and Watterson, 1987; Dawers et al., 1993; Dawers and Anders, 1995).

Based on empirical data the length to displacement ratios of fault systems have been shown to have slopes of 1 – 1.5 over magnitudes of fault length spanning five or more orders of magnitude (Walsh et al., 2002; Nicol et al., 2010). This conventional growth model can be described by:

$$D = cL^n$$

where, D is displacement, n varies between 1 – 1.5, and c is a constant.

In contrast with models of fault development that suggest concomitant increases in displacement and length with time, it has also been argued that faults can increase their cumulative slip/length ratio, as the fault propagates when preexisting weaknesses occur in the host rocks (Walsh et al., 2002). In this alternative model strain focusses on large faults at the expense of numerous other smaller faults. The results of this study clearly differentiate the three different fault populations on a fault length vs fault heave plot (Fig. 3.6).

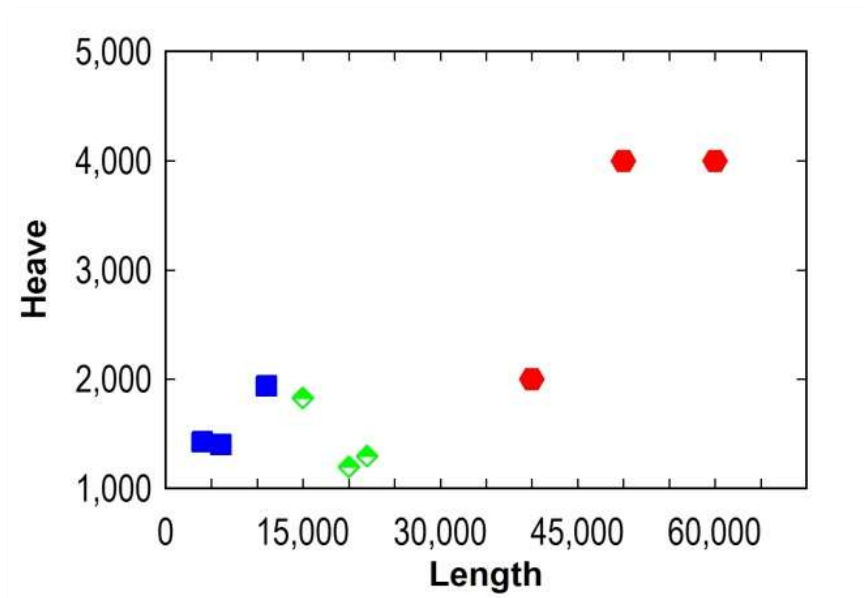


Figure 3.6. Length vs heave plot for breakway faults (blue hexagons), normal rift-flank faults (grey diamonds), and rider blocks (pink squares). Units for x and y axes are in meters.

Several difficulties were encountered when trying to relate this information to the existing models of fault displacement and length. Fault displacement can be

calculated using the fault heave and an average value for the fault angle of $\sim 70^\circ$. What is not known is how much denudation has flattened the seafloor landscape. Evidence suggests that slopes greater than 20° cannot be supported in seafloor peridotites, meaning that the seafloor in areas where a lot of peridotite exists has slopes that are shallower than are expected.

The smooth seafloor in this region is similar to that found at the Australian-Antarctic discordance and along the Southwest Indian Ridge that led to the development of the opposing polarity “flip-flop” model of seafloor formation (Sauter et al., 2013). In smooth seafloor terrain two models for the development of oceanic core complex low-angle normal faults have been proposed: 1) a continuous fault model where a single low-angle normal fault is responsible for the duration of tectonic extension, and 2) a consecutive fault model where multiple low-angle normal faults create oceanic core complexes (Smith et al., 2008) (Fig. 3.7). These two models emphasize that different fault-based mechanisms can produce similar seafloor morphologies. In contrast, it is also possible that these two very different models result in seafloor morphologies that differ significantly. This difference in geometry is made possible by the contrasting detachment fault styles. The continuous model predicts a single dome-shaped footwall whereas the consecutive fault model may encourage the formation of multiple domal surfaces. The creation of smooth seafloor by successive detachment faults of opposing polarities was first proposed by Hess (1962) and the consecutive model discussed here is similar in bathymetric character to numerical models using zero magmatic spreading (Tucholke et al., 2008) and the conceptual flip-flop model of Sauter et al. (2013).

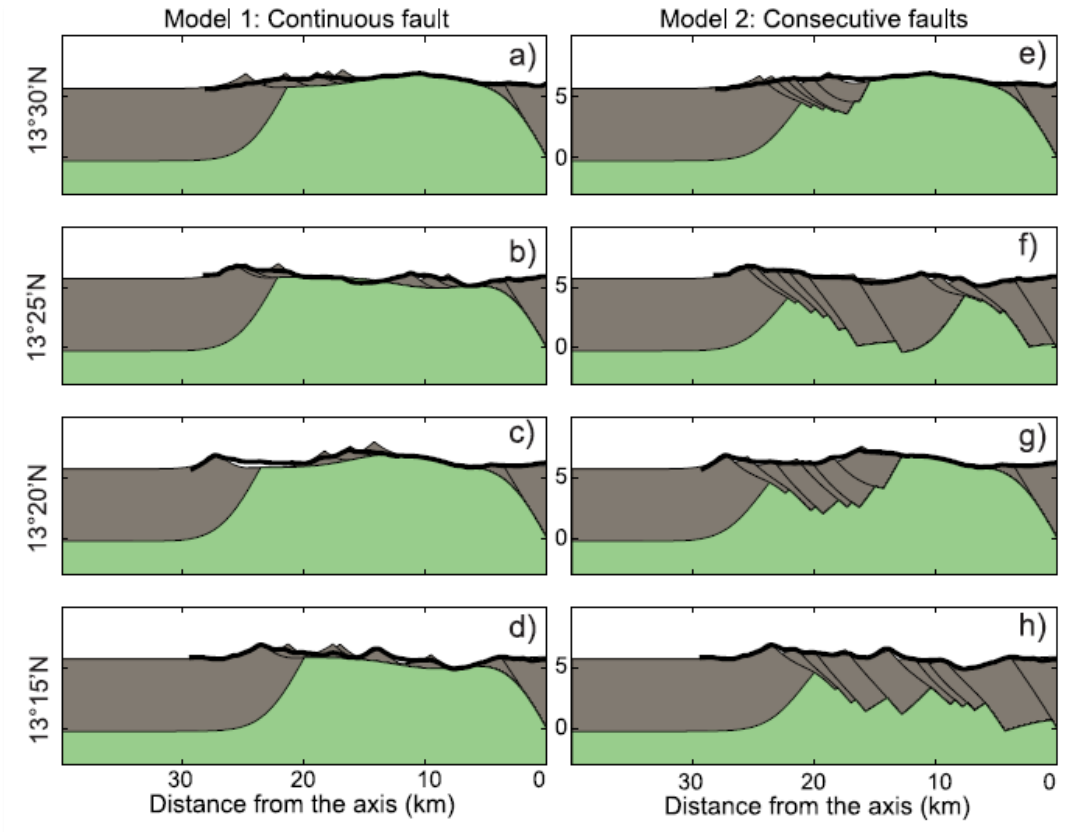


Figure 3.7. Kinematic models for detachment faulting from (Smith et al., 2008). The seafloor topography in adjacent horizontal panels is the same but the mechanisms behind its creation different. In the continuous model one detachment fault is responsible for the creation of the dome-shaped surface. In contrast in the consecutive fault model multiple detachments add sections of the rift valley to the footwall block. The consecutive model may also permit the creation of multiple domal surfaces.

Corrugations and faults were identified in this study by using multibeam echo soundings gridded at a resolution of ~250 m, so features smaller than 250 m cannot be identified. Mapping all of the linear features interpreted to be corrugations and ridges in

the Chaotic Terrain region allows some simple interpretations of the history of extension to be made (Fig. 3.8). Typically corrugations are slip-parallel and have similar wavelengths and amplitudes to those found in detachments systems on land such as in the Chemehuevi Mountains in the southwestern United States (Cann et al., 1997). The change in direction of the corrugations, and therefore spreading, from the western oceanic core complexes, where the corrugations are aligned to $\sim 100^\circ$, to the east, where corrugations occur on a bearing of 115° , is unusual because the large-scale reorganization of the spreading direction (Fig. 3.9) change is thought to occur after the western parts of the basin and Chaotic Terrain formed. Changes in the spreading direction within the Chaotic Terrain indicate that the process driving the basin closure and late-stage volcanism may have started earlier than previously identified by Ishizuka et al. (2009). It is also possible that the observed 15° change in the spreading direction was due to local differences in magmatism along the paleo ridge axis. Furthermore, the relationship between the faults and corrugations is often not orthogonal as can be seen in the lineation map and rose plot (Figs. 3.8 & 3.9).

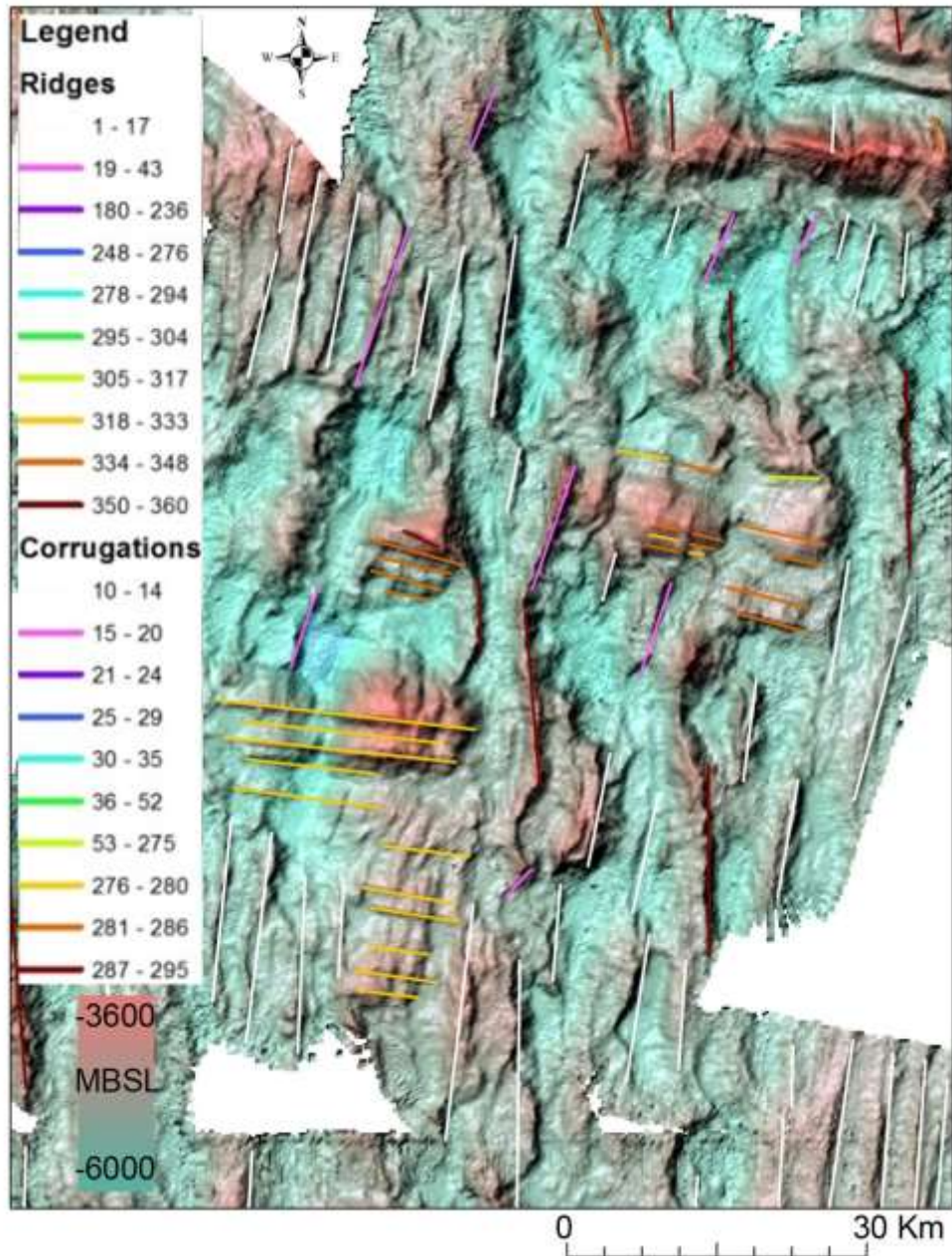


Figure 3.8. Measurements of length and azimuth of linear features interpreted to be corrugations and ridges from the Godzilla Megamullion bathymetry dataset.

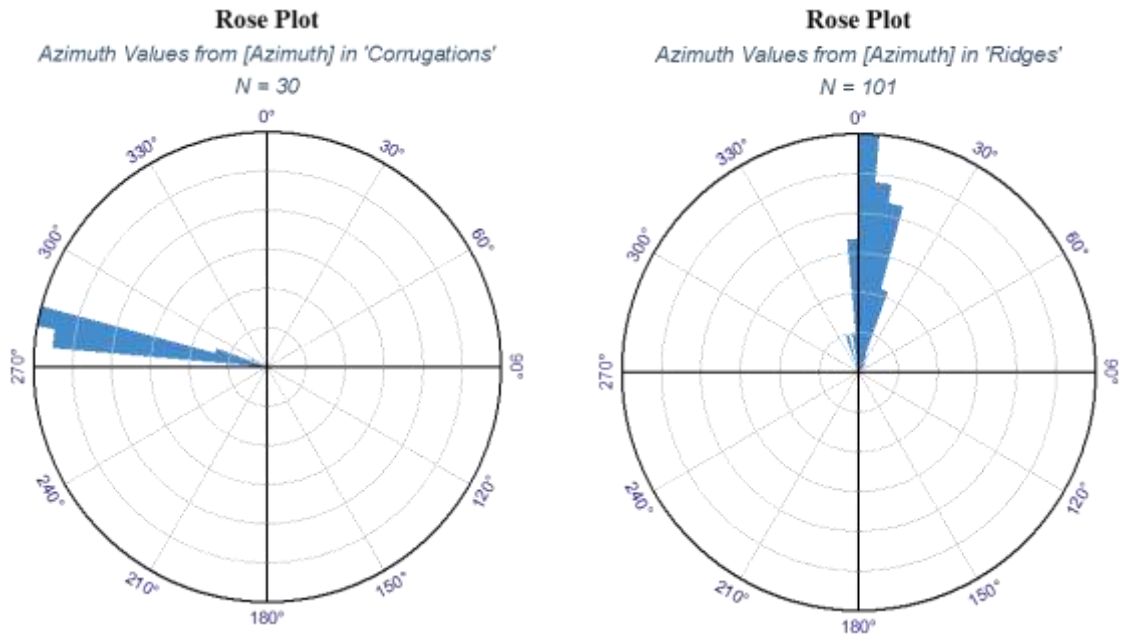


Figure 3.9. Rose plots of the azimuth of corrugations and ridges in the Chaotic Terrain region.

Even though corrugations are the defining morphologic feature of oceanic core complexes, there is little data, or research, that addresses how corrugations form, describes possible mechanisms, or compares corrugations from different regions. The corrugations found on oceanic core complexes have been suggested to represent the geometry of the detachment fault surface, or are the result of an irregular shaped brittle ductile transition zone at depth (Tucholke et al., 2008). More recently, based on rock fabrics from onshore core complexes, the corrugations have been explained by invoking extension perpendicular shortening due to crustal thinning and lateral migration of the lower crust (Singleton, 2012). Arguments have also been made, based on a broad similarity to industrial smelting processes that corrugations are created by the continuous

casting of the lithosphere (Spencer and Ohara, 2014). In the lower crustal flow model the corrugations would be expected to have a wavelength and amplitude that is related to the amount of material being removed from the lower crust and would therefore change in size and shape throughout the lifecycle of an oceanic core complexes. The corrugations typically remain the same size throughout the life of an oceanic core complex. In an upcoming seminar on oceanic core complexes at UTIG, Prof Joe Cann from Leeds University is presenting evidence that corrugations are seen at an extremely wide variety of scales (<http://www.ig.utexas.edu/news/seminars/spring14/cann.htm>). The suggestion that corrugations may be fractal lends some support to a model that is based on fault linkage rather than crustal flow; however a full discussion of these models and their implications is beyond the scope of this work. Because so little is known about how and why they form presently corrugations are used only to determine the direction of spreading and cumulative slip. Australian-Antarctic Discordance and Godzilla Megamullion corrugations are 50 – 150 km long whereas in the Mid Atlantic corrugations occur on a much smaller scale, however to date no detailed global comparisons exist.

The volcanoes in the Chaotic Terrain region have basal diameters of ~3 km. Where the volcanoes occur they are isolated and appear to be the result of point source volcanism rather than the eruptive hummocks that form the building blocks of the upper crust (Yeo et al., 2012). Hummocks are composed of numerous volcanic cones or dome shaped edifices and are 50 – 350 m in diameter, smaller than the grid cell resolution the survey used in this study. Subsea volcanoes are different in that they are morphologically distinct features on the seafloor that have a central crater. Subsea volcanoes are built by

constructive magmatic processes that can be dominated by lava flows or dike intrusions. By conducting shape analysis of seamounts Smith (1988) showed that volcano flatness (diameter summit/diameter base) and summit height can be used to describe most of the variation observed in the shape statistics of 85 Pacific seamounts (Smith and Cann, 1992). Using a buoyancy argument Smith and Cann (1993) showed that volcano height above the seafloor can be related to the magma and depth of the magma source via imbalances in pressures between the magma chamber, lithostat, and hydrostat. The result is that volcanoes grow vertically as peaked cones until restricted at which point they develop flat tops. These observations show that the analysis of the morphology of subsea volcanoes can be used to further understand the processes that created them.

7.1 Comparison of the Chaotic Terrain to Mid-Atlantic Oceanic Core Complexes

Oceanic core complexes from the 14°N region of the Mid Atlantic have both similarities and differences when compared to Chaotic Terrain. The striking difference between the bathymetric maps is in part a function of the higher resolution of the Mid Atlantic dataset (50 m) over the Chaotic Terrain (250 m) (Fig. 3.10). The reduced angle of slopes in the Chaotic Terrain and the presence of slope failure scarps indicates more mass wasting and seafloor weathering has occurred in this region.

The shape and size of the two breakaway faults along which the Godzilla Megamullion initiated are similar to breakaway faults observed in the Mid Atlantic. Similarly, rider blocks and volcanoes are common features of asymmetric spread crust in

both locations. Furthermore, oceanic core complexes in both regions have domed, corrugated, surfaces that feature changes in the azimuth of corrugations (e.g., Mallows, 2011, fig. 3.2.15a). To compare the subsidence information from several oceanic core complexes from the Atlantic and Parece Vela Basin their depths and ages have been plotted together with $\sqrt{\text{time}}$ (Fig. 3.11). The Atlantic oceanic core complexes were assigned zero ages but are likely to have initiated between 0 – 10 Ma. The Atlantic and Parece Vela Basin data plots along the $\sqrt{\text{time}}$ line suggesting that both regions are experiencing typical seafloor subsidence rates and that there is a similarity in the water depths at which these oceanic core complexes formed.

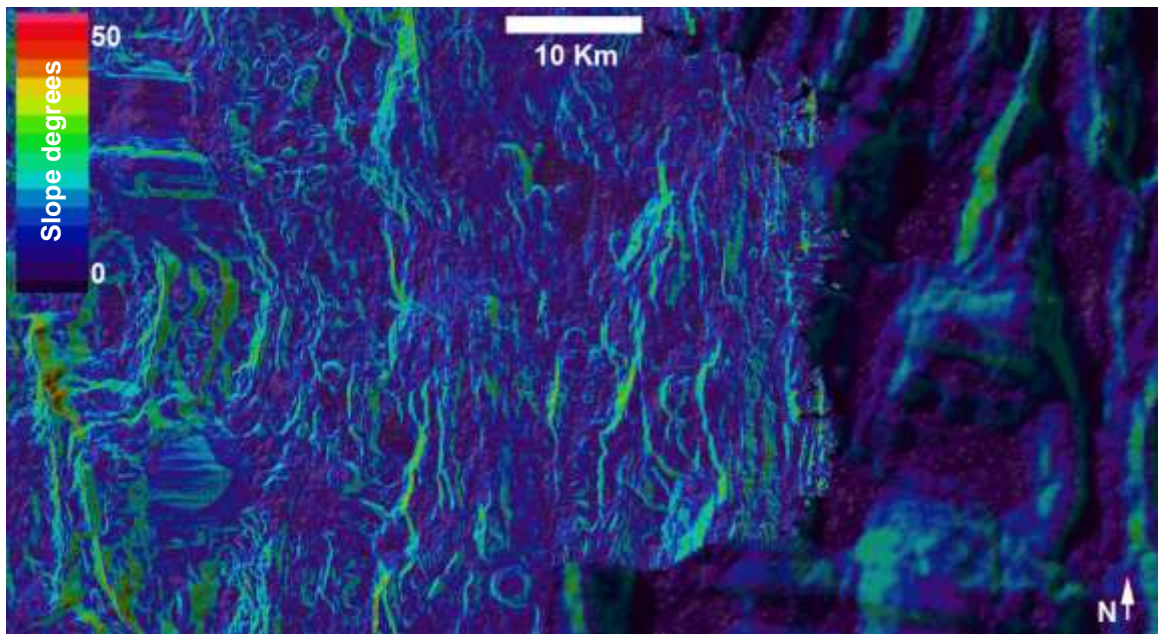


Figure 3.10. Left-hand side: Mid Atlantic Ridge slope map (14°N), Right-hand side: Chaotic Terrain slope map. Some difference is caused by the different grid sizes of two datasets (Cell size: Mid Atlantic=25 m, Godzilla=250 m). Obvious differences can be

observed between the breakaway and domal morphology of both regions of asymmetric spread crust.

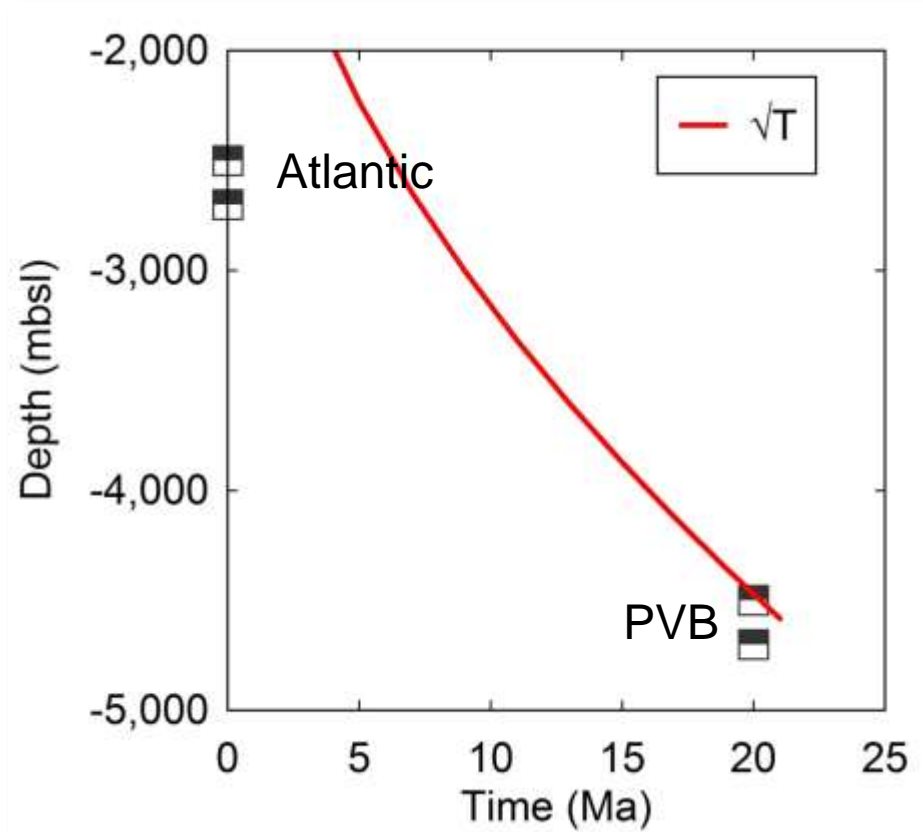


Figure 3.11. Depth – age plot for oceanic core complexes from the Parece Vela Basin (PVB) and 14°N in the Mid-Atlantic (Atlantic). Note that although a zero data was assigned to the Atlantic oceanic core complexes their ages are likely to be between 0 – 10 Ma. Also included is the general ocean depth – age relationship where depth is proportional to the square root of age.

8. Conclusions

The features that have been identified are: 1) breakaway faults, 2) corrugations, 3) rafted blocks, 4) normal rift flank faults, and 5) volcanoes. The corrugations clearly define six regions of seafloor that spread asymmetrically during oceanic core complex formation. Different fault populations were characterized using spatial relationships in the bathymetric surfaces and measurements of the length and heave of the faults. The three fault populations that were identified are: breakaway faults, normal rift-flank faults, and rider blocks.

This study used multibeam deliverables to identify and analyze seafloor features in the Chaotic Terrain region of the Parece Vela Basin. Where the survey resolution allowed recognition of volcanoes they were found to be isolated volcanic centers in regions of symmetric spread crust. The spatial relationships that exist in this region fit a model of oceanic core complex formation by consecutive faults (Smith et al., 2008), but no data has been found that supports a model where detachment faults change polarity (Sauter et al., 2013). From measurements taken along corrugations, the spreading direction was observed to change from $\sim 100^\circ$ in the west to $\sim 115^\circ$ in the eastern part of the survey region.

9. References

- Blackman, D.K., Cann, J.R., Janssen, B., Smith, D.K., 1998. Origin of extensional core complexes: Evidence from the Mid-Atlantic Ridge at Atlantis fracture zone. *Journal of Geophysical Research: Solid Earth* 103, 21315-21333.
- Blackman, D.K., 2009. Geophysical signatures of oceanic core complexes. *Geophysical Journal International* 178, 593-613.
- Bose, S., Mitra, S., 2009. Deformation along oblique and lateral ramps in listric normal faults: Insights from experimental models. *AAPG Bulletin* 93, 431-451.
- Cann, J.R., Blackman, D.K., Smith, D.K., McAllister, E., Janssen, B., Mello, S., Avgerinos, E., Pascoe, A.R., Escartín, J., 1997. Corrugated slip surfaces formed at ridge-transform intersections on the Mid-Atlantic Ridge. *Nature* 385, 329-332.
- Cannat, M., Mangeney, A., Ondréas, H., Fouquet, Y., Normand, A., 2013. High-resolution bathymetry reveals contrasting landslide activity shaping the walls of the Mid-Atlantic Ridge axial valley. *Geochemistry, Geophysics, Geosystems* 14(4), 996-1011.
- Caress, D., Chayes, D., 1995. New software for processing sidescan data from sidescan-capable multibeam sonars, OCEANS'95. MTS/IEEE. Challenges of Our Changing Global Environment. Conference Proceedings. IEEE, pp. 997-1000.
- Choi, E., Buck, W.R., 2012. Constraints on the strength of faults from the geometry of rider blocks in continental and oceanic core complexes. *Journal of Geophysical Research: Solid Earth* 117, B04410.
- Dawers, N.H., Anders, M.H., Scholz, C.H., 1993. Growth of normal faults: Displacement-length scaling. *Geology* 21, 1107-1110.
- Dawers, N.H., Anders, M.H., 1995. Displacement-length scaling and fault linkage. *Journal of Structural Geology* 17, 607-614.
- Dick, H.J.B., Bryan, W.B., Thompson, G., 1981. Low-angle detachment faulting and steady-state emplacement of plutonic rocks at ridge-transform intersections. *Eos: Transactions* 62, 406.
- Escartín, J., Smith, D.K., Cann, J., Schouten, H., Langmuir, C.H., Escrig, S., 2008. Central role of detachment faults in accretion of slow-spreading oceanic lithosphere. *Nature* 455, 790-794.
- Garcés, M., Gee, J.S., 2007. Paleomagnetic evidence of large footwall rotations associated with low-angle faults at the Mid-Atlantic Ridge. *Geology* 35, 279-282.
- Grimes, C.B., John, B.E., Cheadle, M.J., Wooden, J.L., 2008. Protracted construction of gabbroic crust at a slow spreading ridge: Constraints from ²⁰⁶Pb/²³⁸U zircon ages

from Atlantis Massif and IODP Hole U1309D (30°N, MAR). *Geochemistry, Geophysics, Geosystems* 9, Q08012.

Hess, H. H., 1962. History of Ocean Basins, in: Engel, A.E.J., James, H.L., Leonard, B.F. (Eds), *Petrologic Studies: A Volume to honor A.F. Buddington*, Geological Society of America, NY, pp. 599-620.

Ishizuka, O., Yuasa, M., Taylor, R.N., Sakamoto, I., 2009. Two contrasting magmatic types coexist after the cessation of back-arc spreading. *Chemical Geology* 266, 274-296.

Karig, D.E., 1971. Structural history of the Mariana island arc system. *Geological Society of America Bulletin* 82, 323-344.

Loocke, M., Snow, J.E., Ohara, Y., 2013. Melt stagnation in peridotites from the Godzilla Megamullion Oceanic Core Complex, Parece Vela Basin, Philippine Sea. *Lithos* 182, 1-10.

MacLeod, C.J., Searle, R.C., Murton, B.J., Casey, J.F., Mallows, C., Unsworth, S.C., Achenbach, K.L., Harris, M., 2009. Life cycle of oceanic core complexes. *Earth and Planetary Science Letters* 287, 333-344.

MacLeod, C.J., Carlut, J., Escartín, J., Horen, H., Morris, A., 2011. Quantitative constraint on footwall rotations at the 15°45'N oceanic core complex, Mid-Atlantic Ridge: Implications for oceanic detachment fault processes. *Geochemistry, Geophysics, Geosystems* 12(5) Q0AG03.

Mallows, C., 2011. *Geophysical Studies of Oceanic Core Complexes: The Mid-Atlantic Ridge, 13-14°N*. Unpublished doctoral dissertation, Durham University, UK.

Mallows, C., Searle, R.C., 2012. A geophysical study of oceanic core complexes and surrounding terrain, Mid-Atlantic Ridge 13°N - 14°N. *Geochemistry, Geophysics, Geosystems* 13, Q0AG08.

Nicol, A., Walsh, J., Berryman, K., Nodder, S., 2005. Growth of a normal fault by the accumulation of slip over millions of years. *Journal of Structural Geology* 27, 327-342.

Nicol, A., Walsh, J.J., Villamor, P., Seebeck, H., Berryman, K.R., 2010. Normal fault interactions, paleoearthquakes and growth in an active rift. *Journal of Structural Geology* 32, 1101-1113.

Ohara, Y., Yoshida, T., Kato, Y., Kasuga, S., 2001. Giant megamullion in the Parece Vela backarc basin. *Marine Geophysical Researches* 22, 47-61.

Ohara, Y., Okino, K., Kasahara, J., 2007. Seismic study on oceanic core complexes in the Parece Vela back-arc basin. *Island Arc* 16, 348-360.

Ohara, Y., Okino, K., Snow, J.E., 2011. Tectonics of magma-starved crust formation in the Parece Vela Basin. *Modern Approaches in Solid Earth Sciences* 8, 149-168.

Okino, K., Ohara, Y., Kasuga, S., Kato, Y., 1999. The Philippine Sea: New survey results reveal the structure and the history of the marginal basins. *Geophysical Research Letters* 26, 2287-2290.

Okino, K., 2004. Development of oceanic detachment and asymmetric spreading at the Australian-Antarctic discordance. *Geochemistry, Geophysics, Geosystems* 5(12), 1525-2027.

Püthe, C., Gerya, T., 2014. Dependence of mid-ocean ridge morphology on spreading rate in numerical 3-D models. *Gondwana Research* 25, 270-283.

Sanfilippo, A., Dick, H.J.B., Ohara, Y., 2013. Melt–rock reaction in the mantle: Mantle troctolites from the Parece Vela ancient back-arc spreading center. *Journal of Petrology* 54, 861-885.

Sauter, D., Cannat, M., Rouméjon, S., Andreani, M., Birot, D., Bronner, A., Brunelli, D., Carlut, J., Delacour, A., Guyader, V., 2013. Continuous exhumation of mantle-derived rocks at the Southwest Indian Ridge for 11 million years. *Nature Geoscience* 6, 314-320.

Schroeder, T., Cheadle, M.J., Dick, H.J.B., Faul, U., Casey, J.F., Kelemen, P.B., 2007. Nonvolcanic seafloor spreading and corner-flow rotation accommodated by extensional faulting at 15°N on the Mid-Atlantic Ridge: A structural synthesis of ODP Leg 209. *Geochemistry, Geophysics, Geosystems* 8, Q06015.

Singleton, J.S., 2012. Kinematic and geometric evolution of the Buckskin-Rawhide metamorphic core complex, west-central Arizona. Unpublished doctoral dissertation, University of Texas, Austin.

Smith, D.K., 1988. Shape analysis of Pacific seamounts. *Earth and Planetary Science Letters* 90, 457-466.

Smith, D.K., Cann, J.R., 1992. The role of seamount volcanism in crustal construction at the Mid-Atlantic Ridge (24°–30° N). *Journal of Geophysical Research: Solid Earth* 97, 1645-1658.

Smith, D.K., Cann, J.R., 1993. Building the crust at the Mid-Atlantic Ridge. *Nature* 365, 707-715.

Smith, D.K., Cann, J.R., Escartín, J., 2006. Widespread active detachment faulting and core complex formation near 13°N on the Mid-Atlantic Ridge. *Nature* 442, 440-443.

Smith, D.K., Escartín, J., Schouten, H., Cann, J.R., 2008. Fault rotation and core complex formation: Significant processes in seafloor formation at slow-spreading mid-ocean ridges (Mid-Atlantic Ridge, 13°-15°N). *Geochemistry, Geophysics, Geosystems* 9, Q03003.

Spencer, J.E., Ohara, Y., 2014. Curved grooves at the Godzilla Megamullion in the Philippine Sea and their tectonic significance. *Tectonics* 33, 1028-1038.

Tani, K., Dunkley, D.J., Ohara, Y., 2011. Termination of backarc spreading: Zircon dating of a giant oceanic core complex. *Geology* 39, 47-50.

Tucholke, B.E., Lin, J., 1994. A geological model for the structure of ridge segments in slow spreading ocean crust. *J. Geophys. Res.* 99, 11937-11958.

Tucholke, B.E., Behn, M.D., Buck, W.R., Lin, J., 2008. Role of melt supply in oceanic detachment faulting and formation of megamullions. *Geology* 36, 455-458.

Walsh, J.J., Watterson, J., 1987. Distributions of cumulative displacement and seismic slip on a single normal fault surface. *Journal of Structural Geology* 9, 1039-1046.

Walsh, J.J., Nicol, A., Childs, C., 2002. An alternative model for the growth of faults. *Journal of Structural Geology* 24, 1669-1675.

Wilson, S., Murton, B., Taylor, R., 2013. Mantle composition controls the development of an Oceanic Core Complex. *Geochemistry, Geophysics, Geosystems* 14(4), 979-995.

Yeo, I., Searle, R.C., Achenbach, K.L., Le Bas, T.P., Murton, B.J., 2012. Eruptive hummocks: Building blocks of the upper ocean crust. *Geology* 40, 91-94.

Dissertation Conclusions

Multibeam data from the Barbados Accretionary Complex were used to identify and analyze several gas plumes 500 – 1000 m high. There are three main conclusions from this study. First, 3D images of bubble streams can be used to identify current direction in subsea environments where this is otherwise impossible. Second, methane released in deep water (~1500 m) does not reach the ocean surface. And third, to rise ~1000 m through the water column a bubble would need to start out at a size of ~ 40 cm. Bubbles of such a great size do not exist in nature, thus the gases the bubbles contain must not be interacting with the water column. In order to protect the bubbles from dissolution a gas hydrate rim forms and exists only within the gas hydrate stability zone.

Both the climate, and oil and gas, communities have urgent needs for a better understanding of the quantities of gases, and fluids, released into the oceans. In light of the pressing demands of climate system modelers for more accurate inputs and the recent high profile marine based disasters understanding fluxes from the seafloor has never been more critically important than it is today. Integrated multi-scale investigations that feature ship-board data combined with remote and autonomous vehicles is becoming increasingly accessible. Potentially the strategies and tools outlined in this dissertation could be used to identify, analyze, and monitor subsea emissions and as the basis for the development of a global inventory.

Multiple cruise datasets from the Parece Vela Basin were then used to create a multi-resolution bathymetric dataset at a high resolution. This bathymetric dataset allowed the

recognition of new and further detailed analysis of previously known features. Analysis of the data showed that at Godzilla Megamullion the initiation of asymmetric spreading occurred along two oceanic core complexes that subsequently linked across the entire segment. Additionally, the volcanic corrugations present on the Godzilla Megamullion surface and changes in their bathymetry throughout their lifecycle are in agreement with recent geochemical studies, and provides further proof that with decreases in spreading rate, a gabbroic phase is retained in the lithosphere rather than delivered to the surface.

In the Chaotic Terrain region breakaway faults, corrugations, rafted blocks, normal rift flank faults, and volcanoes were mapped. The corrugations clearly define six regions of seafloor that spread asymmetrically during oceanic core complex formation, and show that the spreading direction changed from $\sim 100^\circ$ in the west to $\sim 115^\circ$ in the eastern part of the survey region. The spatial relationships that exist fit a model of oceanic core complex formation by consecutive faults.

In this dissertation, industry leading commercial off-the-shelf software has been used to process and analyze multibeam sonar data. Integrating all of the multibeam sonar data deliverables into one 4D scene provides a cost-effective broad survey model for the rapid evaluation of a location, seafloor, water column characteristics, and geological context. As shown in this dissertation, these tools can be applied to a wide range of industry and scientific marine geoscience problems. It is possible to identify and analyze subsea gas emissions, and also to quantify bathymetric features. Integrating the water column data with acoustic backscatter and bathymetry data provides a better understanding of the relationships that exist between water column features and the seafloor.

Appendix

Published Research/Review Article

<http://www.polarresearch.net/index.php/polar/article/view/17236>

Late Holocene Climate Change Recorded in Proxy Records from Bransfield Basin Sediment Core, Antarctic Peninsula

A. Barnard^{1*}, J.S. Wellner¹, and J.B. Anderson²

¹Department of Earth and Atmospheric Sciences, University of Houston, 4800 Calhoun Road, Houston, 77204-2693 TX, USA.

²Department of Earth Science, Rice University MS-126, 6100 Main Street, Houston, 77005 TX, USA.

Correspondence, A. Barnard: ¹Department of Earth and Atmospheric Sciences, University of Houston, 4800 Calhoun Road, Houston, 77204-2693 TX, USA.

Abstract

The glacimarine environment of the Antarctic Peninsula region is one of the fastest warming places on Earth today, but details of changes in the recent past remain unknown. Late Holocene paleoclimate reconstructions in this region are separated by large distances and widespread variability. This study focuses on a marine sediment core collected from ca. 2000 m below sea level in the Central Bransfield Strait that serves as a key for understanding changes in this region. The core yielded a high sedimentation rate and therefore provides an exceptional high-resolution sedimentary record composed of hemipelagic sediment, with some turbidites. An age model has been created using radiocarbon dates that span the Late Holocene: 3560 cal yr BP to present. This chronostratigraphic framework was used to establish five units, which are grouped into two super-units: a lower super-unit (3560 – 1600 cal yr BP) and an upper super-unit (1600 cal yr BP – present), based upon facies descriptions, laser particle size analysis, x-ray analysis, multi-sensor core logger data, weight percentages and isotopic values of total organic carbon and nitrogen. We interpret the signal contained within the upper super-unit as an increase in surface water irradiance and/or shortening of the sea-ice season and the five units are broadly synchronous with climatic intervals across the Antarctic Peninsula region. While the general trends of regional climatic periods are represented in the Bransfield Basin core we have examined, each additional record that is obtained adds variability to the known history of the Antarctic Peninsula, rather than clarifying specific trends.

1. Introduction

The Antarctic Peninsula is a rapidly warming region that encompasses both marine and glacial environments. Records spanning the last 50 years from the Antarctic Peninsula show a temperature increase of 0.56°C per decade when averaged over the year, and an increase of 1.09°C per decade in the austral winter months, compared to the global mean of $0.13^{\circ}\text{C} \pm 0.03$ per decade (Turner et al. 2005). Austral winter temperatures in the Antarctic Peninsula region have risen by about 6°C over the past 50 years. In addition, in recent years the western Antarctic Peninsula region has experienced more intense ocean warming than the global average, more than 1°C since 1950, as well as increased salinity, in the upper 100 m (Meredith & King 2005). The rapid warming occurring today across the Antarctic Peninsula region is unusual in both synchronicity and extent (e.g., Cook et al. 2005; Steig et al. 2009; Mulvaney et al. 2012). This contrasts with published paleoclimate records taken from marine sediment cores that document diachronous climatic change throughout the Holocene. An understanding of the historical context of this rapid, regional climate change is necessary for the development of models of future changes. To elucidate the Late Holocene climatic changes occurring in different parts of the Bransfield Basin, and their relationships to one another, this study compares new data from a central position in the region with four marine-based sedimentary records derived from similar methods (Domack et al. 2001; Heroy et al. 2008; Michalchuk et al. 2009; Milliken et al. 2009) (Fig. 1).

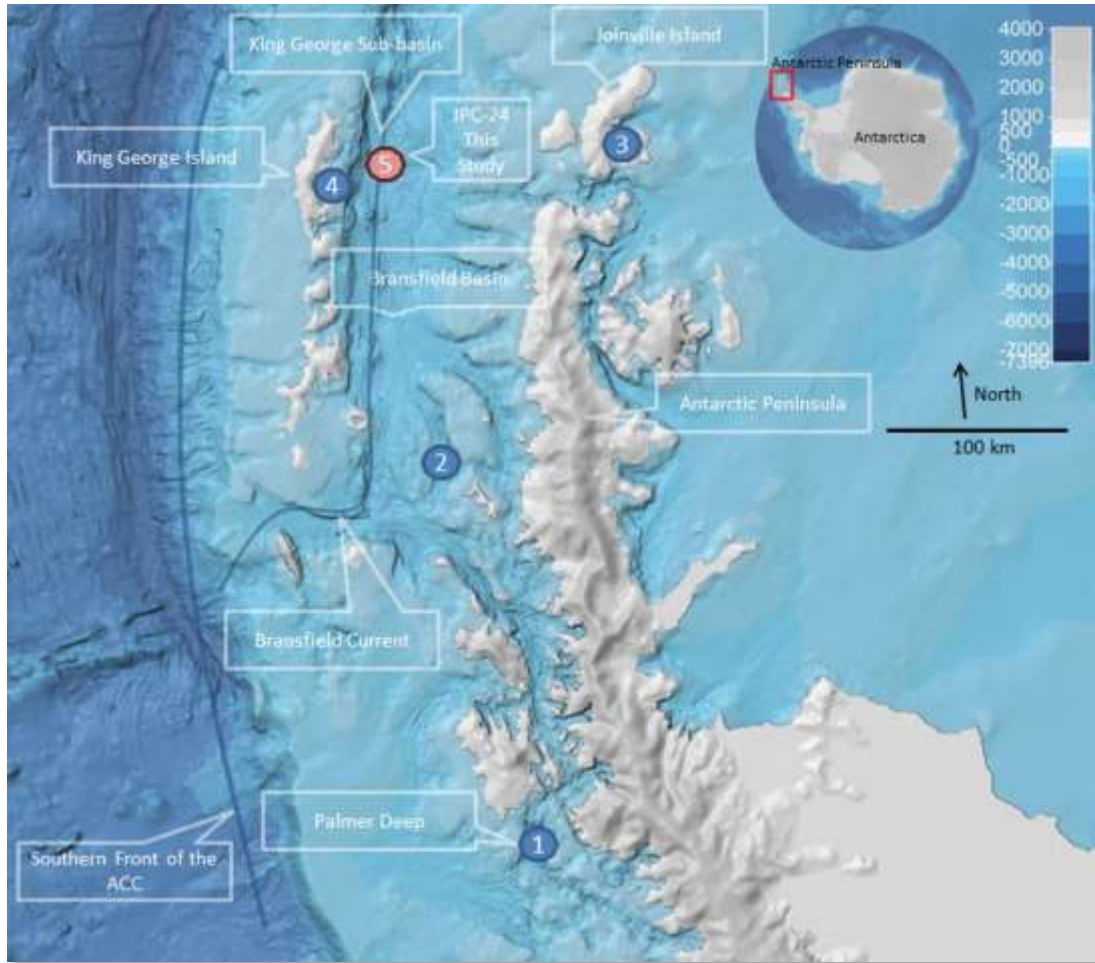


Figure 1. Inset shows the location of the Antarctic Peninsula. Main figure is a regional map of the western Antarctic Peninsula study area including multibeam bathymetry from the International Bathymetric Chart of the Southern Ocean (Arndt et al., 2013). The location of the Antarctic Circumpolar Current (ACC) and Bransfield Current are shown. Four study sites with published records that data in this study are compared to are as follows: (1) Domack et al. (2001); (2) Heroy et al. (2008); (3) Michalchuk et al. (2009); and (4) Milliken et al. (2009) and Majewski et al. (2012). This study (red dot) is the site of core JPC-24, collected during NBP0703.

1.1 Environmental Setting

The Antarctic Peninsula is the warmest and wettest part of Antarctica. Storms, generated in the Amundsen Sea, track into the Bellingshausen Sea, deflect north along the Antarctic Peninsula, and eventually reach the Scotia Sea. Because of these storms, the western/northern seaboard of the Antarctic Peninsula has a comparatively warm, humid climate. In comparison, the eastern side is colder and dryer (Reynolds 1981). The dominant controls of temperature and precipitation patterns across the peninsula are storms and orographic effects. Temperature differences between the north and south are controlled by latitudinal temperature gradients. Temperature data from across the Antarctic Peninsula (Reynolds 1981; Vaughan & Doake 1996) document a broad, regional, thermal control of ice shelves on the western Antarctic Peninsula. Ice shelves exist only on the cold side of the -5 to -9°C isotherm (Vaughan & Doake 1996). Moreover, temperature changes affect glacial sediment yields as shown by recent increases in sediment accumulation rates from the Antarctic Peninsula to Patagonia (Boldt et al. 2013).

The source of coastal waters in Antarctica is the mid-level water mass of the Antarctic Circumpolar Current, which is composed of warm, saline, Circumpolar Deep Water. Circumpolar Deep Water is divided into upper and lower units, with the Upper Circumpolar Deep Water distinguished by its relatively warm temperature and the Lower Circumpolar Deep Water by its relatively high salinity. The Antarctic Circumpolar Current bifurcates around the South Shetland Islands and traverses the length of the northern Bransfield Strait as the Bransfield Current (Meredith et al. 2010), and has in

recent years provided regular intrusions of Upper Circumpolar Deep Water onto the continental shelf (Ducklow et al. 2007). This is important because the Upper Circumpolar Deep Water is 3 – 4°C above freezing, significantly warmer than the Bransfield Strait water temperature that varies seasonally between 0 and -2°C in the austral summer and winter, respectively. In this region, where the average thickness of sea ice is less than 1 m, a 1°C increase in surface ocean temperature is equivalent to a 30 cm reduction in the formation of sea ice (Meredith & King 2005). The presence of Upper Circumpolar Deep Water has also been associated with increases in productivity (Prezelin et al. 2000).

Since the Last Glacial Maximum, when grounded ice reached the continental shelf and perennial sea ice covered the Bransfield Strait (Heroy & Anderson 2005, 2007; Simms et al. 2011), ice has continued to retreat with some minor re-advances. Bentley et al. (2009) provide a synthesis of the Holocene climate and outline five periods. Three warm periods (Mid-Holocene Warm Period, Medieval Warm Period and the recent rapid warming) that are associated with warmer ocean waters, higher productivity and higher sedimentation rates. Two intervening cold periods (Neoglacial and Little Ice Age) associated with intense perennial sea ice and colder air temperatures. Climate controlled the sedimentary evolution of the western Antarctic Peninsula throughout the Holocene, regionally determining the pattern and volume of sediment delivery and facies variability (Griffith & Anderson 1989). The present-day synchronous rapid warming of the Antarctic Peninsula contrasts with published Holocene marine sediment core records that document diachronous climatic changes across the region (Domack et al. 2001; Heroy et al. 2008; Michalchuk et al. 2009; Milliken et al. 2009; Majewski et al. 2012).

Paleoenvironmental proxy data in these studies shows that Late Holocene climate change was broadly synchronous in extent, although the timing varied with latitude and location. Published proxy records suggest that the onset of the Neoglacial varies with distance from the continent, occurring earlier in the sites closest to the Antarctic Peninsula and later in the more northerly sites (Domack et al. 2001; Taylor & Sjunneskog 2002; Heroy 2008; Michalchuk et al. 2009; Milliken et al. 2009). The existence of a Medieval Warm Period and a Little Ice Age in Antarctica is uncertain since each has been documented in only a few records (Bentley et al. 2009).

2. Study Area

The study area is the Bransfield Strait in the north-western Antarctic Peninsula (Fig. 1). This area is the most northerly part of the Antarctic continent, and extends north into the Southern Ocean to 63° S. Along the northern continental margin of the Antarctic Peninsula lie the South Shetland Islands. These islands are separated from the Antarctic Peninsula by the Bransfield Strait, a distance of about 125 km (Fig. 1). The strait opens in the west to the Bellingshausen Sea and in the east to the Weddell Sea and is the geographic counterpart of the geologic Bransfield Basin. The basin is further sub-divided into three domains: the West Bransfield Basin, the Central Bransfield Basin and the East Bransfield Basin. The flat-bottomed part of the Central Bransfield Basin adjacent to King George Island is known as the King George Sub-basin.

3. Methods

The data used in this study were collected in 2007 onboard the RV/IB *Nathaniel B. Palmer*, during cruise NBP0703. Real-time geophysical data were analyzed onboard and used to identify a coring location in the King-George Sub-basin of the Central Bransfield Basin where undisturbed hemipelagic sediment would be sampled (Garcia et al. 2008). Jumbo piston core JPC-24 (22 m) and Jumbo trigger core JTC-24 (1.33 m) were recovered from a water depth of 1980 m (62° 16.449'S, 57° 38.7000'W; Fig. 2). A hull mounted Bathy 2000 (Ocean Data Equipment Corporation, Warwick, RI, USA) unit with a 3.5 kHz swept frequency source was used in conjunction with a EM120 multibeam unit (Simrad, Horten, Norway) to provide a detailed image of the seafloor and upper sediment layers (Figs. 2, 3). In the onboard laboratory, detailed sediment core analyses were completed including: color (using a Munsell color chart), grain size and sedimentary and biogenic structures. The core was also digitally recorded using a camera and then sampled for a preliminary study of the sediment composition.

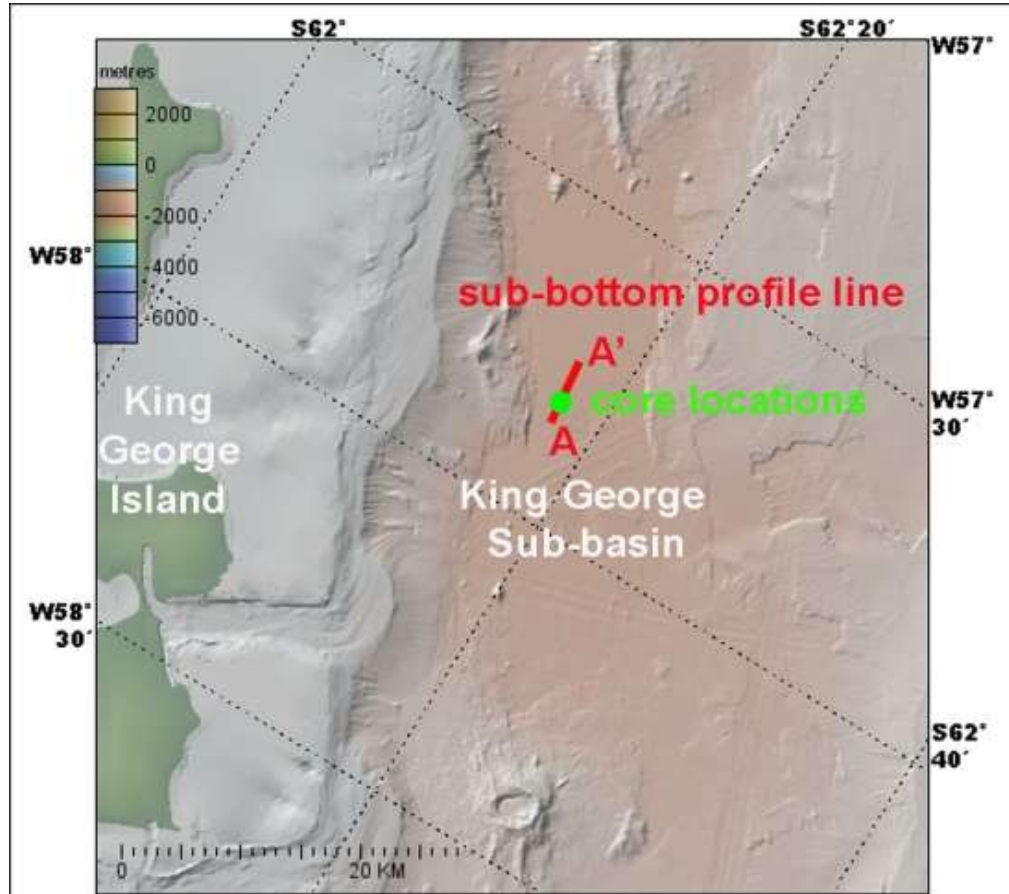


Figure 2. Bathymetry of the Bransfield Basin. Location of Fig. 3 is shown as a red line with core locations as a green circle. Map created using GeoMapApp (Carbotte et al. 2007).

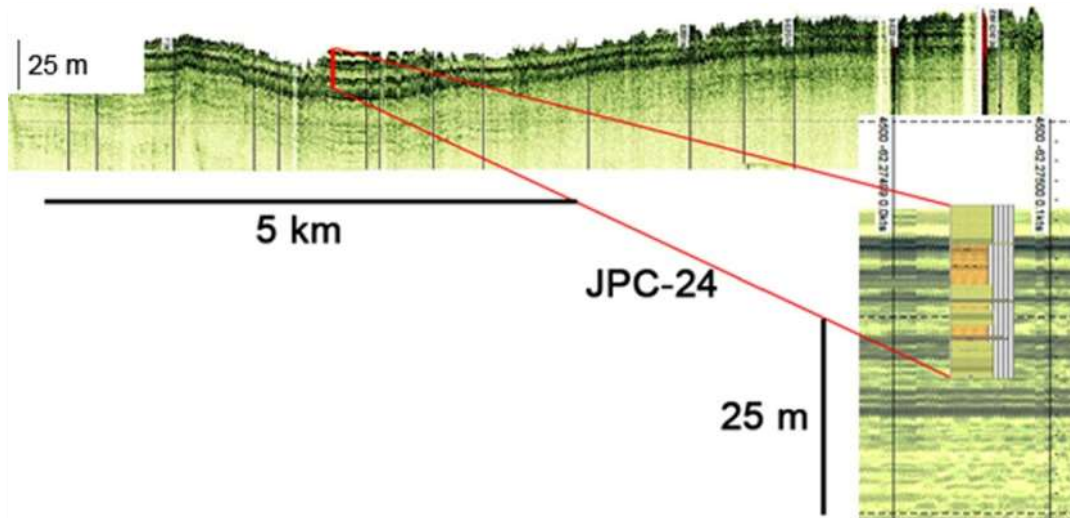


Figure 3. Chirp 3.5 kHz sub-bottom profile, y axis is depth and x axis is distance. Vertical exaggeration in the bathymetric profile is approximately 40. Inset: changes in the core lithology (JPC-24) correlate with acoustic reflection surfaces. The location shown in Fig. 2. Inset: core lithology represented by colors, where green is clayey mud, orange is clay, and gray is sand–gravel and mottling represents abundant organic matter. Vertical bars are grain size, from left to right: clay, sand, gravel.

3.1 Radiocarbon Dates

Seven carbonate samples collected from the core were sent to the University of California Irvine for accelerated mass spectrometry dating. The CALIB V.6 software program was used for calibration and correction (Stuiver et al. 2005). A ΔR of 700 years was added to the standard marine reservoir correction of about 350 – 400 years, giving the 1100-year correction appropriate for Antarctic waters (Domack et al. 2001; Milliken et al. 2009). The dates are provided in Table 1.

Lab. no.	Core depth (cm)	Fraction modern (‰)	+/-	$\delta^{14}\text{C}$ (‰)	+/-	^{14}C age (BP)	+/-	Cal yr BP	+/- ^a
69391	0 ^b	0.87	0.0013	-126	1.3	1080	15	-57 ^d	2
69389	490 ^c	0.76	0.0013	-242	1.3	2225	15	1081	37
40843	556 ^c	0.78	0.0021	-219	2.1	1985	25	832 ^d	44
69390	671 ^b	0.75	0.0010	-254	1.0	2360	15	1228	32
40852	1273 ^c	0.70	0.0021	-300	2.1	2865	25	1759 ^d	43
40850	1692	0.63	0.0017	-368	1.7	3680	25	2750	11
40853	2194 ^c	0.58	0.5821	-418	6.2	4350	90	3559 ^d	54

^a 1 σ error of calibrated age

^b From articulated shells

^c From shell fragment material

^d Dates used in the radiocarbon age model

Table 1. Dates were calibrated using Calib v.6.0 software, and using the marine 04.14c calibration curve that incorporates a 350-400 year correction (Stuiver et al. 2005). A marine reservoir ΔR of 700 years was added, making the total marine reservoir correction about 1100 years.

3.2 Sedimentology

The sediment cores were described as part of NBP0703 and detailed facies descriptions, and sampling intervals were conducted at the Antarctic Research Facility,

Florida State University. The core contains four main facies that include green silty clay, dark olive gray silt, very poorly sorted sand granules and clay and fining upwards sandy layers. Sediment magnetic susceptibility and density were recorded at 1 cm intervals using a MSCL 7.6 (Geotek, Deventry, UK). Artefacts caused both by division of the core into individual sections and zones of incomplete core recovery have been removed from the data. Additional samples were collected for laser particle size analysis at 10 cm intervals. Measurements were conducted using a Mastersizer 2000 (Malvern Instruments, Worcester, UK). Magnetic susceptibility is used to estimate relative abundance of terrigenous versus biogenic material following Anderson (1999). X-ray radiographs were supplied by the Antarctic Research Facility at a 1:1 scale at 300 dpi, used as a non-invasive techniques to find pebbles (>4 mm) down core at 5 cm intervals.

3.3 Geochemistry

For geochemical analysis, we collected 107 samples. Samples (10 cc) were taken at 20 cm intervals down core, in 1 cm diameter sample tubes. Sample preparation followed methods outlined in Milliken et al. (2009). Samples were analyzed at the University of California Davis. Isotopic values and elemental values of carbon and nitrogen were measured using continuous flow mass spectrometry. Precision of the measurements is +/- 0.1⁰/₀₀ for isotopic values (δ) of carbon, +/- 0.2⁰/₀₀ for nitrogen, 0.5% for carbon (μg), and 0.1% for nitrogen (μg). Organic carbon and nitrogen results were normalized using the weight of sediment ($\mu\text{gC, N} / \text{sediment weight} [\mu\text{g}]$) to give weight percentages (wt.%). The isotopic values were supplied by the University of California Davis in parts per thousand (⁰/₀₀), relative to Pee Dee Belemnite (PDB) (carbon) and air (nitrogen). We

have adapted the calculation of mass accumulation rates from Willmott et al. (2009) that uses the elemental concentration of carbon and nitrogen, dry bulk density and sedimentation rate to calculate organic matter mass accumulation rates by removing dry bulk density. Including dry bulk density as calculated from multi-sensor core logger density does not change the mass accumulation rates significantly and is therefore omitted allowing use of the equation over a broader range of data sets. The equation we use is:

$$\text{Mass accumulation rate}_{(\text{TOC,N})} = \frac{\text{TOC,N (wt.\%)}}{100 \cdot \text{sedimentation rate (cm yr}^{-1}\text{)}} \quad (1)$$

4. Results

4.1 Geophysical Analysis and Core Integration

Core JPC-24 and JTC-24 were recovered from the 2000 m deep King George Sub-basin. The core is mostly composed of green-grey diatomaceous silty clays and clayey silt. Continuous parallel reflections in the sub-bottom profile correlate with the JPC-24 core lithology, suggesting the complete recovery of recent sediments. Results from a trigger core (JTC-24) taken at the same location corroborate the integrity of the core top.

4.2 Radiocarbon Age Model

The highest stratigraphic date was recovered from 0 cm and yielded an age of 0 calibrated years before present (cal yr BP; laboratory number 69391; Table 1). Since it is difficult to use radiocarbon dating techniques on material younger than 1950, we set our 0 cal yr BP date to represent the most recent sediment, and acknowledge that this tallies

with our linear age model. A simple linear interpolation age model has been constructed for the youngest radiocarbon dates (Fig. 4) and is used to convert depth in core (cm) to cal yr BP. Of the seven carbonate samples dated we chose the four youngest dates to construct an age model for this core, including the core-top zero date. Three older dates that do not fall in chronological order, along a linear regression of the youngest dates, are only older by a few hundred years and reinforce the existing age model, providing a possible age range for delivery of reworked sediments to the deep Bransfield Basin.

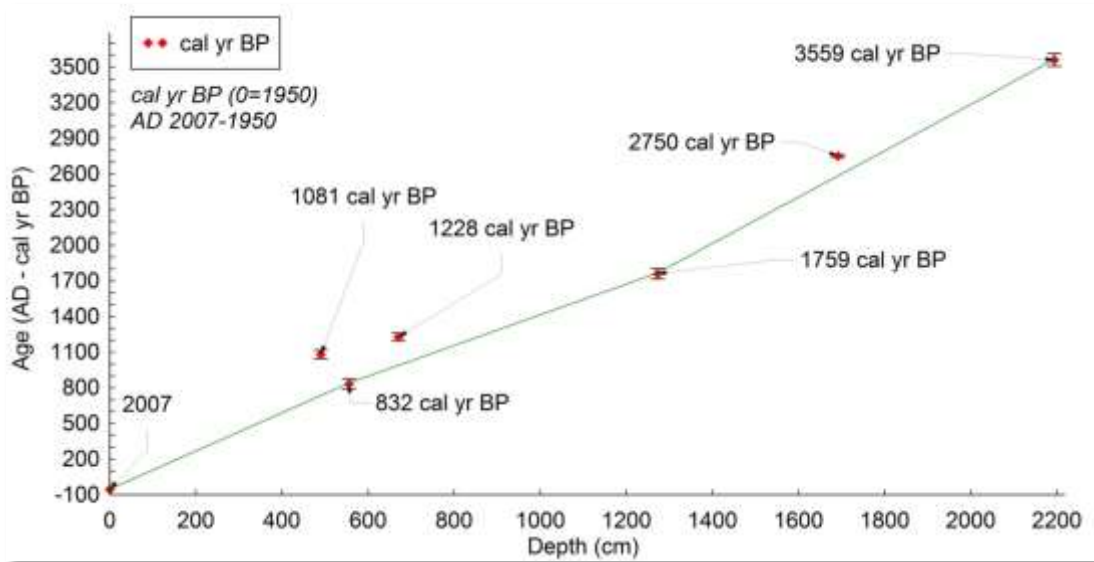
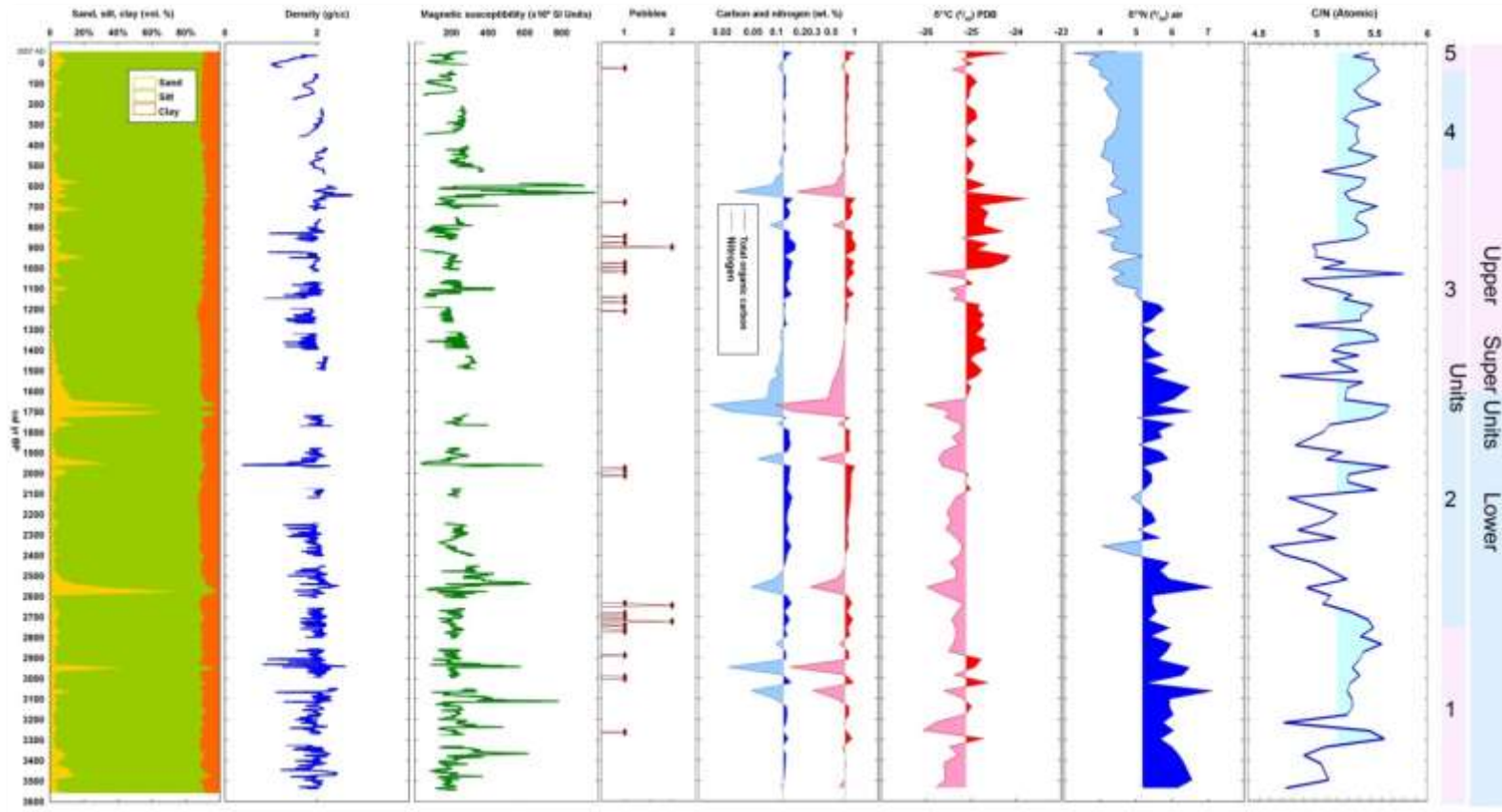


Figure 4. Age model for the radiocarbon dates, constructed by linear interpolation, showing 1 σ error bars. Because 1950 AD is equivalent to 0 cal yr BP, the age model uses negative values on the x axis to reach 2007 AD (-57 cal yr BP). The calculated sedimentation rate, based on a linear interpretation from the origin to 22 m at 3559 cal yr BP, is 0.6 cm/yr.

4.3 Super-units and Units

According to our age model we present two super-units and five units that have been recognized based on facies analysis, grain size data, magnetic susceptibility, pebble count, and weight percentages, ratio and isotopic values of carbon and nitrogen (Fig. 5). For the whole data set the average mean $\delta^{13}\text{C}$ and $\delta^{15}\text{N}$ values are -25‰ and 5‰ , respectively, with ranges of ca. 2‰ ($\delta^{13}\text{C}$) and ca. 4‰ ($\delta^{15}\text{N}$). The lower super-unit covers the age range 3560 – 1600 cal yr BP, and the upper super-unit from 1600 cal yr BP – present. Average mean values for total organic carbon and nitrogen (wt. %) are 0.75 and 0.12, respectively, and the average mean atomic C/N ratio is 5.3. The upper super-unit has higher average mean values of total organic carbon and nitrogen (wt. %), and $\delta^{13}\text{C}$ that are higher than the mean average and lower $\delta^{15}\text{N}$ values. Comparison of the weight percentages and facies shows that the lowest values occur in coarser sediments. In contrast, the lower super-unit has average-mean isotopic signature values that are higher than the data set averages for $\delta^{15}\text{N}$, and lower for $\delta^{13}\text{C}$. Unit boundaries are defined by relatively small changes in the proxy data, resulting in less well-defined boundaries between units: 1/2, 3/4 and 4/5.

Figure 5. Grain size (sand, silt, clay percentages), multi-sensor core logger data (density and magnetic susceptibility), pebble count, elemental and isotopic data (total organic carbon and nitrogen (wt. %), $\delta^{13}\text{C}$, $\delta^{15}\text{N}$ (‰)) and the C/N atomic ratio for units and super-units throughout JPC-24 plotted by age (cal yr BP).



4.4 Units

Unit 1 (3560 – 2600 cal yr BP) is composed of hemipelagic sediment with some distal turbidites, and includes the highest sustained $\delta^{15}\text{N}$ values within this core, with values consistently above the data set mean average. Unit 2 (2600 – 1600 cal yr BP) is characterized by organic-rich hemipelagic sediment including three turbidites, and lower $\delta^{15}\text{N}$ values through the middle of the unit. Unit 3 (1600 – 500 cal yr BP) is dominated by organic-rich hemipelagic sediment and includes a layer of abundant angular granules interpreted as ice-rafted debris. The maximum $\delta^{13}\text{C}$ value, -24‰ , occurs in unit 3 along with above average concentrations of carbon and nitrogen. Unit 4 (500 – 50 cal yr BP) is composed of low density, low magnetic susceptibility hemipelagic sediment, with no pebbles and less sand relative to the other units (vol. %). Throughout units 3 and 4, $\delta^{15}\text{N}$ decreases toward the core top, with a slight increase in $\delta^{15}\text{N}$ values in unit 4. Unit 5 is characterized by a wider range of $\delta^{15}\text{N}$ values and high $\delta^{13}\text{C}$ values (-24.2‰).

5. Discussion

The ratio of biogenic to terrigenous sediment determines the magnetic susceptibility character. High percentages of biogenic sediment result in relatively low magnetic susceptibility values, and high percentages of terrigenous sediment produce high magnetic susceptibility values. Consequently, magnetic susceptibility has been widely implemented as a proxy for the ratio of marine to land-derived sediment. From 1600 cal yr BP to present, low magnetic susceptibility is more frequent in the upper super-unit,

and most probably represents an increase in the accumulation of marine organic matter at this time.

In glacial marine environments coarse sediments, grain size greater than 4 mm, are typically interpreted as ice-rafted debris. The importance of sea ice in the Bransfield Strait for sedimentation is well defined by extreme levels of seasonal variability in the particle flux. As much as 97% – 99% of the mass flux occurs during the austral summer (Wefer et al. 1988; Khim et al. 2005). Ice-rafted debris is delivered to the deep basin either by sea ice or by icebergs, meaning that it also requires open ocean conditions. Units 1 and 3 contain the highest pebble counts indicating a larger contribution of ice-rafted debris and also low magnetic susceptibility values. These proxies reveal the increased relative inputs of marine organic accumulation and terrigenous material from ice-rafted debris, not turbidites. The dominance of marine organic matter and ice-rafted debris in the sedimentary record establishes that open ocean conditions prevailed during those times. When the Bransfield Strait is free of sea ice (pancake ice) icebergs and near-shore sea ice enter the Bransfield Strait unhindered, resulting in a greater supply of ice-rafted debris to the Central Bransfield Basin.

Most of the sediment in JPC-24 (90%) is homogeneous hemipelagic sediment with a mean average C/N ratio of 5.3. The results in this study show a very strong positive correlation (correlation coefficient of 0.98) between carbon and nitrogen with a very low standard deviation (0.04). We interpret these results to mean that the carbon and nitrogen isotopic signature represents marine organic matter. In Fig. 6*' the best-fit line of the

carbon and nitrogen data crosses the origin signifying that that these samples contain insignificant amounts of inorganic carbon or nitrogen.

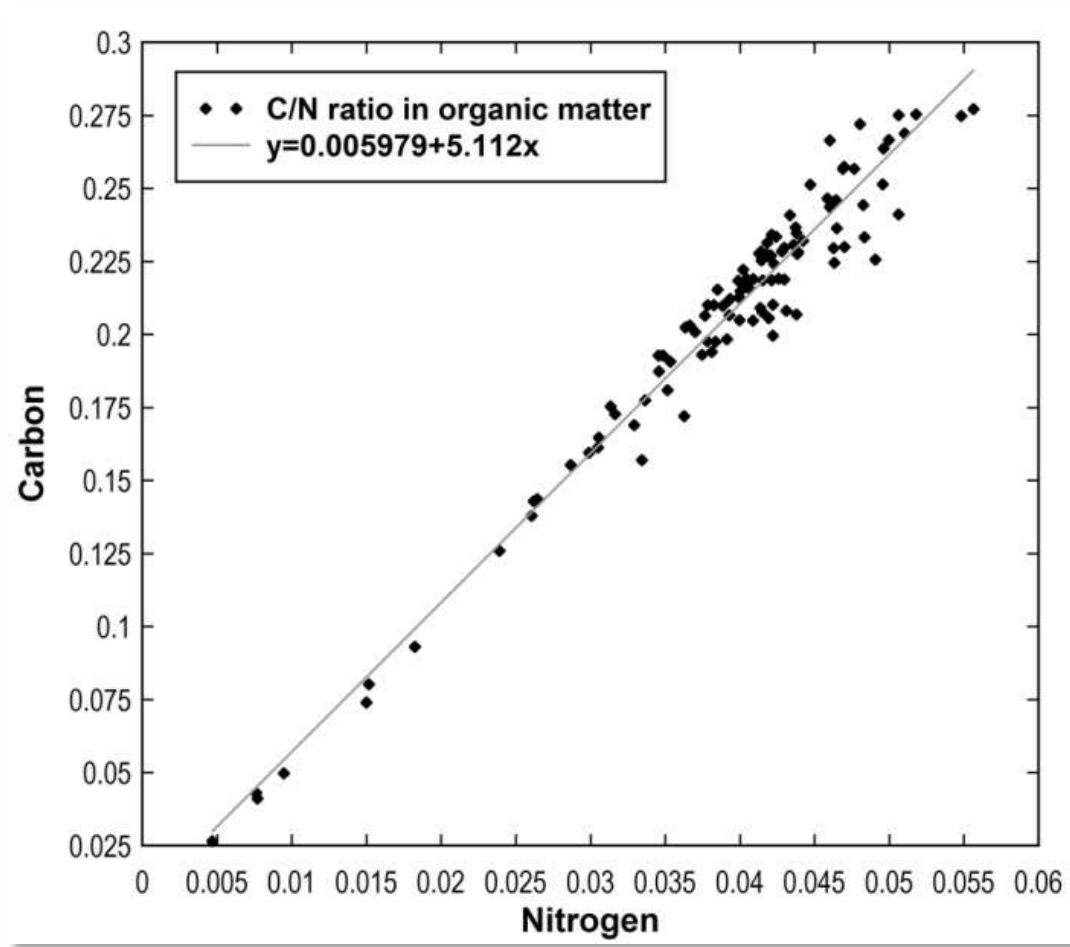


Figure 6. Atomic carbon and nitrogen ratio of organic matter. The correlation coefficient for the best-fit line is 0.99. The traditional Redfield Ratio has a slope between 3 and 8 and here the best-fit line has a slope of 5.1.

The slope of the C/N ratio is 5.1, close to the stoichiometry found in the traditional Redfield Ratio (ca. 6.6 [Redfield 1934]). To achieve the Redfield Ratio marine organisms

must achieve a balanced lifestyle requiring limiting nutrients and tolerable levels of environmental stress. When balance is not achieved the Redfield Ratio becomes a broader realm of C/N values between 3 – 8.75 (Jørgensen & Bendoricchio 2001). Phytoplankton attain the Redfield Ratio when growing at their maximum growth rate (Goldman et al. 1979) and if the supply of nutrients is sufficient that no single nutrient limits growth, then the only limitation of biomass is the quantity of nutrients available. From this data we infer that changes in the isotopic signature are likely to represent changes in surface biomass (productivity).

The carbon isotopic signature in our data has a mean average $\delta^{13}\text{C}$ value of -24‰ that can be explained by the sources and metabolic pathways used. Sources of carbon for marine phytoplankton are dissolved-marine bicarbonate with a $\delta^{13}\text{C}$ value of ca. 0‰ and dissolved CO_2 that has a $\delta^{13}\text{C}$ value of ca. -6‰ (Meyers 1994). Marine phytoplankton use the photosynthetic C3 pathway that creates an isotopic shift in of about -20‰ , as a function of dissolved CO_2 , temperature, light and nutrient supply (Meyers 1997).

The trend toward higher $\delta^{13}\text{C}$ values in the younger parts of the core (Fig. 7) could be driven by the “cold-water effect” proposed by Rau et al. (1989) whereby increased isotopic discrimination toward ^{12}C occurs when the abundance of dissolved CO_2 increases. Additionally, the concentration of dissolved CO_2 is higher in cold water so it is preferentially incorporated during photosynthetic activity over marine bicarbonate. Light is also an important factor in surface waters and the amount of irradiance can influence $\delta^{13}\text{C}$ values; in laboratory experiments exposure to increased levels of irradiance over a 24-hour period caused 1.5‰ higher $\delta^{13}\text{C}$ values in phytoplankton (Burkhardt et al.

1999). Changes in the environmental conditions are expected to be related to changes in diatom assemblages.

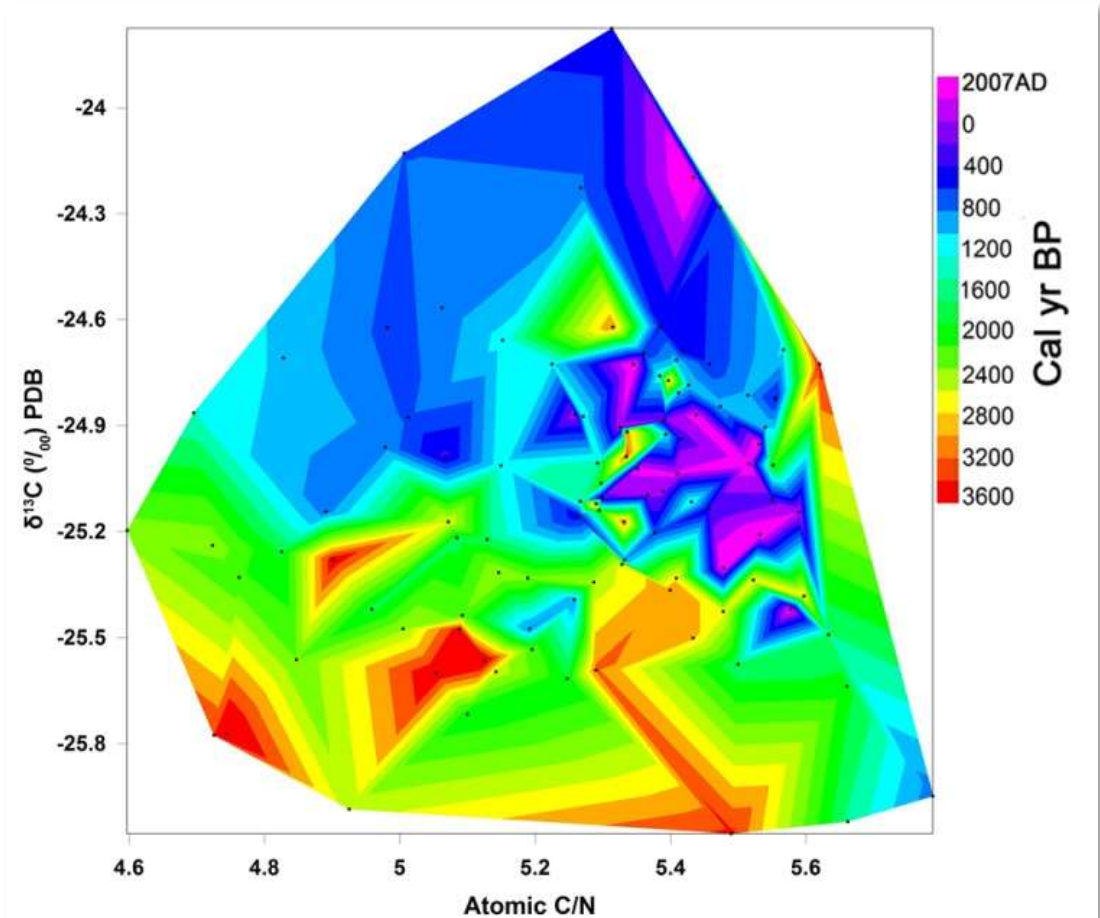


Figure 7. Three-dimensional plot of $\delta^{13}\text{C}$ and C/N ratio. The highest $\delta^{13}\text{C}$ values occur in the youngest parts of the core.

Using a sedimentary record from the Central Bransfield Basin Barcena et al. (1998) showed that there has been an increase in the amount of diatom sea-ice taxa over the last 2000 years. The range of carbon isotopic values changes quite dramatically during seasonal sea ice diatom taxa variations by up to 10‰ (Henley et al. 2012). Because our

$\delta^{13}\text{C}$ values only change by 1 – 1.5‰, it is possible that only small modifications to the assemblages are driving the changes we observe. It is unlikely that our results represent transfer from autotrophic to heterotrophic communities because this would result in a step-wise enrichment of both $\delta^{15}\text{N}$ (3.5‰) and $\delta^{13}\text{C}$ (1.5‰) values (Rau et al. 1983; Minagawa & Wada 1984). It therefore seems reasonable to attribute the increase in $\delta^{13}\text{C}$ values at 1600 cal yr BP to changes in the environmental conditions that affected the diatom assemblages.

Using both the carbon and nitrogen isotopic signatures, plotted with the mass accumulation rate of organic matter provides an insight into the ratio of productivity in surface waters to accumulation on the seafloor. Figure 8 shows that $\delta^{13}\text{C}$ and total organic carbon mass accumulation values have a positive relationship, whereas $\delta^{15}\text{N}$ values and nitrogen mass accumulation values have a negative relationship. This is further evidence that there is a strong relationship between the accumulation of organic matter in sediment and the isotopic signature. The organic matter provides a record of isotopic fractionation during primary production related to surface water processes.

The utilization of different nitrogen compounds in surface waters is controlled by the uptake of different compounds of nitrogen so the $\delta^{15}\text{N}$ signature changes as a function of the compound used. The mean average $\delta^{15}\text{N}$ of the marine organic matter in this core is 5‰, a value similar to that of nitrate entering the oceans via continental runoff (5-10‰). In the upper super-unit there is a trend towards lower $\delta^{15}\text{N}$ values. So long as the nutrient supply maintains an abundance of surface $^{14}\text{[N]-NO}_3^-$, increases in productivity result in lower $\delta^{15}\text{N}$ values than would be expected with increasing levels of productivity (Meyers

1997; Altabet & Francois 2001). Nutrient supply levels are so high in the Antarctic Peninsula region that they fuel not just local but also regional increases in productivity (Ardelan et al. 2010).

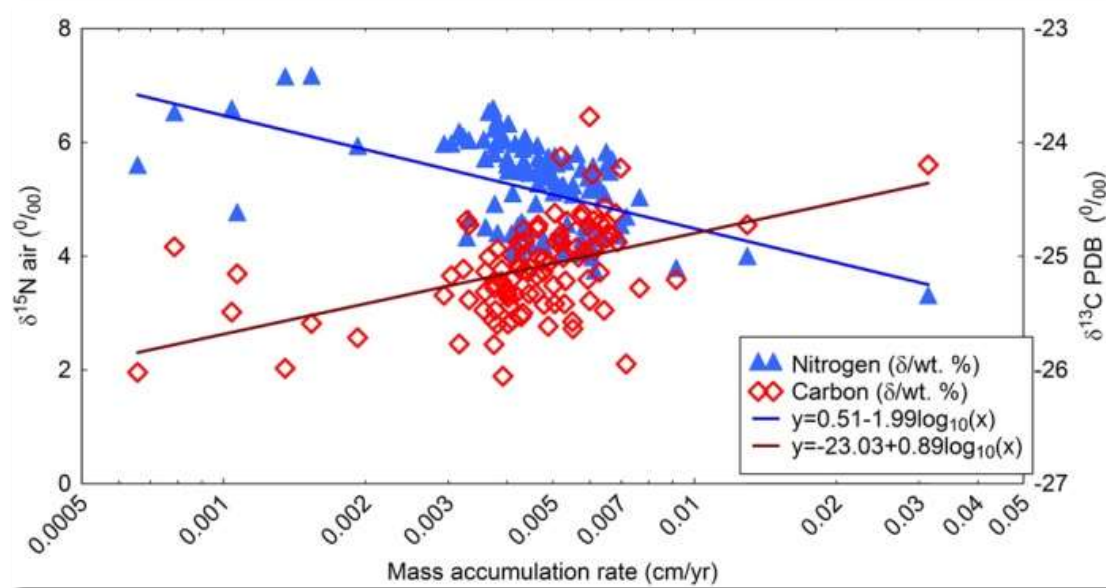


Figure 8. Total organic carbon and nitrogen mass accumulation rate, $\delta^{13}\text{C}$ and $\delta^{15}\text{N}$ values cross-plot with best fit lines, correlation coefficients for nitrogen 0.48 and carbon 0.41, standard deviation of 0.69 and 0.36, respectively.

In the Bransfield Strait during the austral summer regenerated production using “recycled” ammonium with lower $\delta^{15}\text{N}$ values accounts for more than 80% of the total primary production (Koike et al. 1986). Regenerated production can also be fueled by ammonium (NH_4^+) produced by phytoplankton as a mechanism to lose excess energy gained from increased levels of irradiance (Lomas et al. 2000). Recent studies of the mixed layer depth and nitrate assimilation in the Southern Ocean strongly suggest that

light limitation is the dominant control of nitrate assimilation (DiFiore et al. 2009). An increase in regenerated production could alter the $\delta^{15}\text{N}$ values in relative isolation from the $\delta^{13}\text{C}$ values resulting in a decoupled $\delta^{13}\text{C}$ and $\delta^{15}\text{N}$ signal.

Irradiance of surface waters causes increased late summer levels of regenerated production and can change the community structure. Differential uptake and remineralization following a seasonal pattern has also been observed (Lourey et al. 2003). Coincident maximums for both mass flux and regenerated production occur in the late summer. The concomitant increases in late summer (January – February) regenerated production and mass flux result in a greater preservation potential of the isotopic signature.

5.1 Correlation of Units to Late Holocene Climate Periods

Climate records from the maritime western Antarctic Peninsula feature regional heterogeneity and the results in this paper allow new comparisons and correlation of Late Holocene climate changes to be made (Fig. 9). Unit 1 (3560 – 2600 cal yr BP) is broadly synchronous with the later stages of the Mid-Holocene Warm Period (Fig. 9), a period of warmth, reduced sea ice and greater melt-water-derived sedimentation (Bentley et al. 2009). The Mid-Holocene Warm Period is seen in many records from this region, ending in Palmer Deep at 3360 (Domack et al. 2001), in the Bransfield Strait (Heroy et al. 2008) and Maxwell Bay (Milliken et al. 2009; Majewski et al. 2012) at 2000 – 2600 cal yr BP, and in the Firth of Tay at 3500 cal yr BP (Michalchuk et al. 2009). Unit 2 (2600 – 1600 cal yr BP) is broadly synchronous with the Neoglacial Interval, a period of pronounced

shift to colder climate on land and increased sea ice and cooler waters at sea (Bentley et al. 2009). Cores from the Palmer Deep (Domack et al. 2001) and Firth of Tay (Michalchuk et al. 2009) document the Neoglacial Interval as a period of cooling continuing through to the recent rapid warming (Fig. 9).

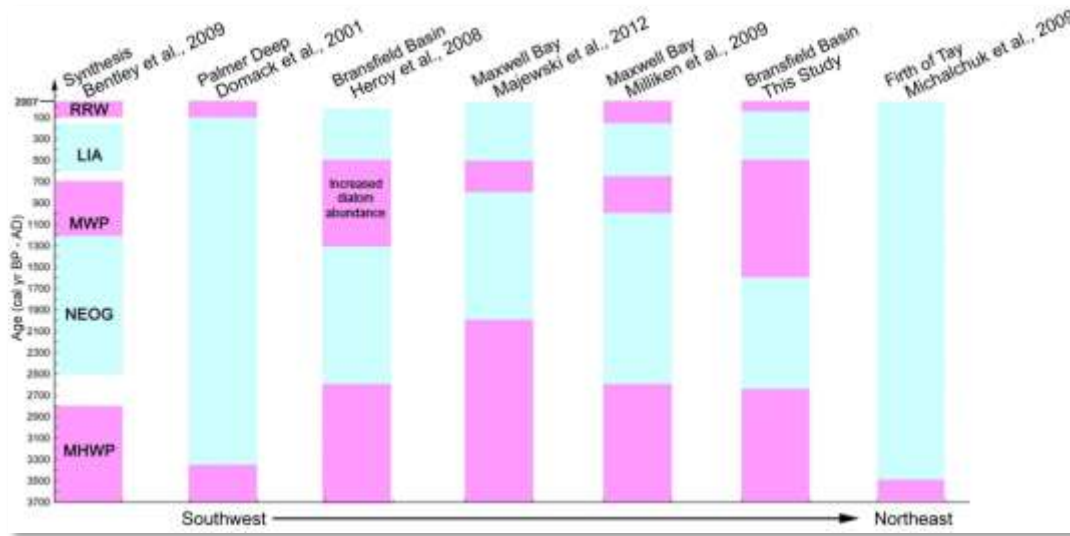


Figure 9. Summary showing the warm (pink) and cold (blue) periods defined in other studies and compared to this study. Bentley et al. (2009) presented a summary including onshore and offshore work but the timings of the changes are uncertain and are shown as gaps. The other six columns are marine records organized geographically from southwest to north-east. Terms are abbreviated as follows: Recent Rapid Warming (RRW); Little Ice Age (LIA); Medieval Warm Period (MWP); Neoglacial (NEOG); Mid-Holocene Warm Period (MHWP).

Unit 3 (1600 – 500 cal yr BP) is broadly synchronous with the Medieval Warm Period (Bentley et al. 2009; Lu et al. 2012), observed in proxy data from Maxwell Bay (Milliken et al. 2009; Majewski et al. 2012), and the Bransfield Basin (Heroy et al. 2008 and this study). El Niño Southern Oscillation records peak at 1200 cal yr BP, providing a potential explanation for the greater variability in proxy data from this study at that time (Bentley et al. 2009). Other studies from the region also document increased sea-surface temperatures following 1600 – 2000 cal yr BP (Nielsen et al. 2004). Prior to 650 cal yr BP the climate warmed, shown by the fact that the Collins Ice Cap on King George Island was at or behind its present extent (Hall 2007) and in the western Antarctic Peninsula ice extent was at or behind its present extent between 970 – 700 cal yr BP (Hall et al. 2010). Unit 4 (500 – 50 cal yr BP) is similar in timing to the Little Ice Age (Bentley et al. 2009; Lu et al. 2012), and also coincides with a decrease in productivity at the Palmer Deep (Sjunneskog & Taylor 2002). Land-based records show glacier advances at this time, for example the Collins Ice Cap advanced at 650 cal yr BP (Hall 2007). In Palmer Deep, the Little Ice Age is dated between 700 and 150 cal yr BP (Domack et al. 2001). Unit 5 (50 cal yr BP – present) is equivalent to the present-day recent rapid warming. It has been recognized in numerous proxy records by higher sedimentation rates, increased total organic carbon, more ice-rafted debris and higher clay percentages (Bentley et al. 2009; Lu et al. 2010). These diachronous Late Holocene climatic changes that coincide with the Neoglacial, Medieval Warm Period, Little Ice Age and Recent Rapid Warming highlight the importance of global climate to this region.

6. Summary and Conclusions

This study defines two super-units and five units that are broadly synchronous with known climatic intervals across the Antarctic Peninsula region. An interval representing a climatic change is defined by the super-unit boundary at approximately 1600 cal yr BP. Since then, the climate in the Bransfield Strait has changed and these changes are recorded in diatom productivity proxies in the sediments. Correlation to other proxy records from the region (Domack et al. 2001; Heroy et al. 2008; Michalchuk et al. 2009; Milliken et al. 2009; Majewski et al. 2012) indicates that these Late Holocene changes are broadly synchronous, yet high-resolution studies are starting to show that each area has its own detailed history, unlike the changes happening across the Antarctic Peninsula today.

The integrated proxy data show that regional climatic changes, previously identified in more proximal locations, can be identified in Holocene sediments accumulating in the deep Bransfield Basin. This suggests that drill cores obtained from the Bransfield Basin in the future could be used to reconstruct older Late Quaternary glacial–interglacial cycles. Records from the key time periods include material derived from the glacimarine environment during glacial advances and retreats.

Detailed analysis of the geochemical data allows us to make some general conclusions about the marine environmental conditions at the time of deposition. Since 1600 cal yr BP, the isotopic signatures of carbon and nitrogen document a change in the surface water conditions that are recorded by the diatom assemblages. The similarity of

the C/N ratio to the traditional Redfield Ratio indicates an autochthonous marine planktonic source for the organic matter unlimited by nutrients. Variations in the amount of organic matter in the sediment correlate well with changes in the isotopic signature, interpreted as a record of surface water biogeochemical fractionation. Seasonal maximums in organic matter reaching the basin floor and regenerated production during the summer sea ice free season provide a geochemical signature of the past environmental conditions. The changes observed were likely to have been driven by increases in surface water irradiance as the sea-ice season shortens.

7. Acknowledgements

We acknowledge the National Science Foundation for funding this project (OPP-0739596 to JSW and JBA). We thank the science party of NBP0703, Rice University Sedimentology Laboratory, Petroleum Systems and Geochemistry Program at the University of Houston, Steve Ackley for discussion of sea-ice trends, Qi Fu and three anonymous reviewers.

8. References

- Altabet M.A. & Francois R. 2001. Nitrogen isotope biogeochemistry of the Antarctic Polar Frontal Zone at 170°W. *Deep-Sea Research Part II* 48, 4247–4273.
- Anderson J.B. 1999. *Antarctic marine geology*. Cambridge: Cambridge University Press.
- Ardelan M.V., Holm-Hansen O., Hewes C.D., Reiss C.S., Silva N.S., Dulaiova H., Steinnes E. & Sakshaug E. 2010. Natural iron enrichment around the Antarctic Peninsula in the Southern Ocean. *Biogeosciences* 7, 11–25.
- Arndt, J.E., Werner Schenke, H., Jakobsson, M., Nitsche, F.O., Buys, G., Goleby, B., Rebesco, M., Bohoyo, F., Hong, J., Black, J., Greku, R., Udintsev, G., Barrios, F., Reynoso-Peralta, W., Taisei M., & Wigley, R. 2013. The International Bathymetric Chart of the Southern Ocean (IBCSO) Version 1.0—A new bathymetric compilation covering circum-Antarctic waters. *Geophysical Research Letters* 40, 3111–3117.
- Barcena M.A., Gersonde R., Ledesma S., Fabres J., Calafat A.M., Canals M., Sierro F.J. & Flores J.A. 1998. Record of Holocene glacial oscillations in Bransfield Basin as revealed by siliceous microfossil assemblages. *Antarctic Science* 10, 269–285.
- Bentley M.J., Hodgson D.A., Smith J.A., O Cofaigh C., Domack E.W., Larter, R.D., Roberts S.J., Brachfeld S., Leventer A., Hjort C., Hillenbrand C.D. & Evans J. 2009. Mechanisms of Holocene paleoenvironmental change in the Antarctic Peninsula region. *The Holocene* 19, 51–69.
- Boldt K.V., Nittrouer C.A., Hallet B., Koppes M.N., Forrest B.K., Wellner J.S. & Anderson J.B. 2013. Modern rates of glacial sediment accumulation along a 15° S–N transect in fjords from the Antarctic Peninsula to southern Chile. *Journal of Geophysical Research—Earth Surface* 118, 2072–2088.
- Burkhardt S., Riebesell U. & Zondervan I. 1999. Effects of growth rate, CO₂ concentration, and cell size on the stable carbon isotope fractionation in marine phytoplankton. *Geochimica et Cosmochimica Acta* 63, 3729–3741.
- Carbotte S.M., Ryan W.B.F., O’Hara S., Arko R., Goodwillie A., Melkonian A., Weissel R.A. & Ferrini V.L. 2007. Antarctic multibeam bathymetry and geophysical data synthesis: an on-line digital data resource for marine geoscience research in the Southern Ocean. U.S. Geological Survey Open-File Report 2007-1047. Short Research Paper 002. Reston, VA: U.S. Geological Survey.
- Cook A.J., Fox A.J., Vaughan D.G. & Ferrigno J.G. 2005. Retreating glacier fronts on the Antarctic Peninsula over the past half-century. *Science* 308, 541–544.
- DiFiore P.J., Sigman D.M., Karsh K.L., Trull T.W., Dunbar R.B. & Robinson R.S. 2010. Poleward decrease in the isotope effect of nitrate assimilation across the Southern

Ocean. *Geophysical Research Letters* 37, article no. L17601, doi: 10.1029/2010GL044090.

Domack E., Leventer A., Dunbar R., Taylor F., Brachfeld S. & Sjunneskog C. 2001. Chronology of the Palmer Deep site, Antarctic Peninsula; a Holocene paleoenvironmental reference for the circum-Antarctic. *The Holocene* 11, 1-9.

Ducklow H.W., Baker K., Fraser W.R., Martinson D.G., Quetin L.B., Ross R.M., Smith R.C., Stammerjohn S. & Vernet M. 2007. Marine pelagic ecosystems: the West Antarctic Peninsula. *Philosophical Transactions of the Royal Society of London B*, 362, 67–94.

García M., Ercilla G., Anderson J.B. & Alonso B. 2008. New insights on the post-rift seismic stratigraphic architecture and sedimentary evolution of the Antarctic Peninsula margin (Central Bransfield Basin). *Marine Geology* 251, 167-82.

Goldman J.C., McCarthy J.J. & Peavey D.G. 1979. Growth rate influence on the chemical composition of phytoplankton in oceanic waters. *Nature* 279, 210–215.

Griffith T.W. & Anderson J.B. 1989. Climatic control of sedimentation in bays and fjords of the northern Antarctic Peninsula. *Marine Geology* 85, 181–204.

Hall B.L. 2007. Late-Holocene advance of the Collins Ice Cap, King George Island, South Shetland Islands. *The Holocene* 17, 1253-1258.

Hall B.L., Koffman T. & Denton G.H. 2010. Reduced ice extent on the western Antarctic Peninsula at 700-900 cal yr BP. *Geology* 38, 635-638.

Henley S.F., Annett A.L., Ganeshram R.S., Carson D.S., Weston K., Crosta X., Tait A., Dougans J., Fallick A.E. & Clarke A. 2012. Factors influencing the stable carbon isotopic composition of suspended and sinking organic matter in the coastal Antarctic sea ice environment, *Biogeosciences*, 9, 1137-1157.

Heroy D. & Anderson J.B. 2005. Ice sheet extent on the Antarctic Peninsula during the last glacial maximum (LGM)—insights from glacial geomorphology. *Geological Society of America Bulletin* 117, 1497-1512.

Heroy D.C. & Anderson J.B. 2007. Radiocarbon constraints on Antarctic Peninsula ice sheet retreat following the Last Glacial Maximum (LGM). *Quaternary Science Reviews* 26, 3286-3297.

Heroy D.C., Sjunneskog C. & Anderson J.B. 2008. Holocene climate change in the Bransfield Basin, Antarctic Peninsula; evidence from sediment and diatom analysis. *Antarctic Science* 20, 69-87.

Jørgensen S.E. & Bendricchio G. 2001. *Fundamentals of ecosystem modeling*. Amsterdam: Elsevier.

Khim B.K., Kim D., Shin H.C. & Kim D.Y. 2005. Stable carbon and nitrogen isotopes of sinking particles in the eastern Bransfield Strait (Antarctica). *Ocean Science Journal* 40, 167-176.

King J.C. 1994. Recent climate variability in the vicinity of the Antarctic Peninsula. *International Journal of Climatology* 14, 357-369.

Koike I., Holm-Hansen O. & Biggs D.C. 1986. Inorganic nitrogen metabolism by Antarctic phytoplankton with special reference to ammonium cycling. *Marine Ecology Progress Series* 30, 105–116.

Lomas M.W., Rumbley C.J. & Glibert P.M. 2000. Ammonium release by nitrogen sufficient diatoms in response to rapid increases in irradiance. *Journal of Plankton Research* 22, 2351–2366.

Lourey M.J., Trull T.W. & Sigman D.M. 2003. Sensitivity of $\delta^{15}\text{N}$ of nitrate, surface suspended and deep sinking particulate nitrogen to seasonal nitrate depletion in the Southern Ocean. *Global Biogeochemical Cycles* 17, 1-7.

Lu Z., Rickaby R.E.M., Kennedy H., Kennedy P., Pancost R.D., Shaw S., Lennie A., Wellner J. & Anderson J.B. 2012. An ikaite record of late Holocene climate at the Antarctic Peninsula. *Earth and Planetary Science Letters* 325-326, 108-115.

Lu Z., Rickaby R.E.M., Wellner J., Georg B., Charnley N., Anderson J.B. & Hensen C. 2010. Pore fluid modeling approach to identify recent meltwater signals on the west Antarctic Peninsula. *Geochemistry, Geophysics, Geosystems* 11, 14-21.

Majewski W., Wellner J.S., Szczuciński W. & Anderson J.B. 2012. Holocene oceanographic and glacial changes recorded in Maxwell Bay, West Antarctica. *Marine Geology* 326-328, 67-79.

Meredith M.P. & King J.C. 2005. Rapid climate change in the ocean west of the Antarctic Peninsula during the second half of the 20th century. *Geophysical Research Letters* 32, article no. L19604, doi: 10.1029/2005GL024042.

Meredith M.P., Wallace M.I., Stammerjohn S.E., Renfrew I.A., Clarke A., Venables H.J., Shoosmith D.R., Souster T. & Leng, M.J. 2010. Changes in the freshwater composition of the upper ocean west of the Antarctic Peninsula during the first decade of the 21st century. *Progress in Oceanography*, 87, 127-143.

Meyers P.A. 1994. Preservation of elemental and isotopic source identification of sedimentary organic matter. *Chemical Geology* 114, 289-302.

Meyers P.A. 1997. Organic geochemical proxies of paleoceanographic, paleolimnologic, and paleoclimatic processes. *Organic Geochemistry* 27, 213-250.

Michalchuk B.R., Anderson J.B., Wellner J.S., Manley P.L., Majewski W. & Bohaty S. 2009. Holocene climate and glacial history of the northeastern Antarctic Peninsula: the marine sedimentary record from a long SHALDRIL core. *Quaternary Science Reviews* 28, 3049-3065.

Milliken K.T., Anderson J.B., Wellner, J.S., Bohaty S.M. & Manley P.L. 2009. High-resolution climate history of Maxwell Bay, South Shetland Islands, Antarctica. *Geological Society of America Bulletin* 121, 1711-1725.

Minagawa M. & Wada E. 1984. Stepwise enrichment of ^{15}N along food chains: further evidence and the relation between $\delta^{15}\text{N}$ and animal age. *Geochimica et Cosmochimica Acta* 48, 1135-1140.

Mulvaney R., Abram N.J., Hindmarsh R.C.A., Arrowsmith C., Fleet L., Triest J., Sime L.C., Alemany O. & Foord S. 2012. Recent Antarctic Peninsula warming relative to Holocene climate and ice-shelf history. *Nature* 489, 141-145.

Nielsen S.H.H., Koc N. & Crosta X. 2004. Holocene climate in the Atlantic sector of the Southern Ocean: controlled by insolation or oceanic circulation? *Geology* 4, 317–320.

Prezelin B.B., Hofmann E.E., Mengelt C. & Klinck J.M. 2000. The linkage between Upper Circumpolar Deep Water (UCDW) and phytoplankton assemblages on the west Antarctic Peninsula continental shelf. *Journal of Marine Research* 58, 165-202.

Rau G.H., Mearns A.J., Young D.R., Olson R.J., Schafer H.A. & Kaplan I.R. 1983. Animal $^{12}\text{C}/^{13}\text{C}$ correlates with trophic level in pelagic food webs. *Ecology* 64, 1314-1318.

Rau G.H., Takahashi T. & Des Marais D.J. 1989. Latitudinal variations in plankton $\delta^{13}\text{C}$: implications for CO_2 and productivity in past oceans. *Nature* 341, 516-518.

Redfield A.C. 1934. On the proportions of organic derivatives in seawater and their relation to the composition of plankton. In R.J. Daniel (ed.): James Johnson memorial volume. Pp. 177–192. Liverpool: Liverpool University Press.

Reynolds J.M. 1981. The distribution of mean annual temperatures in the Antarctic Peninsula. *British Antarctic Survey Bulletin* 54, 123-133.

Simms A.R., Milliken K.T., Anderson J.B. & Wellner J.S. 2011. The marine record of deglaciation of the South Shetland Islands, Antarctica since the Last Glacial Maximum. *Quaternary Science Reviews* 30, 1538 -1601.

Sjunneskog C. & Taylor F. 2002. Postglacial marine diatom record of the Palmer Deep, Antarctic Peninsula (ODP Leg 178, Site 1098) 1. Total diatom abundance. *Paleoceanography* 17, article no. 8003, doi: 10.1029/2000PA000563.

Steig E.J., Schneider D.P., Rutherford S.D., Mann M.E., Comiso J.C. & Shindell D.T. 2009. Warming of the Antarctic ice-sheet surface since the 1957 International Geophysical Year. *Nature* 457, 459-462.

Stuiver M., Reimer P.J. & Reimer, R. W. 2005. Calib v.6.0. Accessed on the internet at <http://calib.qub.ac.uk/calib/> on 1 November 2008.

Taylor F. & Sjunneskog C. 2002. Postglacial marine diatom record of the Palmer Deep, Antarctic Peninsula (ODP Leg 178, Site 1098) 2. Diatom assemblages. *Paleoceanography*, 17, article no. 1026, doi: 10.1029/2000PA000564.

Turner J., Colwell S.R., Marshall G.J., Lachlan-Cope T.A., Carleton A.M., Jones P.D., Lagun V., Reid P.A. & Iagovkina S. 2005. Antarctic climate change during the last 50 years. *International Journal of Climatology* 25, 279–294.

Vaughan D.G. & Doake C.S.M. 1996. Recent atmospheric warming and retreat of ice shelves on the Antarctic Peninsula. *Nature* 379, 328-379.

Wefer G., Fischer G., Fuetterer D. & Gersonde R. 1988. Seasonal particle flux in the Bransfield Strait, Antarctica. *Deep Sea Research Part I* 35, 891-898.

Willmott V., Rampen S.W., Domack E.W., Canals M., Damste J.S.S. & Schouten S. 2009. Holocene changes in Proboscia diatom productivity in shelf waters of the northwestern Antarctic Peninsula. *Antarctic Science* 22, 3-10.